COMPUTATIONAL INVESTIGATION OF HYDRODYNAMICS OF VISCOELASTIC FLUIDS FLOWING AROUND SQUARE CYLINDER AND COMPLEX FLUID RHEOLOGY VIA MAGNETIC RESONANCE IMAGING

A THESIS SUBMITTED TO
THE GRADUATE SCHOOL OF NATURAL AND APPLIED SCIENCES
OF
MIDDLE EAST TECHNICAL UNIVERSITY

BY

GÜLER BENGÜSU TEZEL

IN PARTIAL FULFILLMENT OF THE REQUIREMENTS
FOR
THE DEGREE OF DOCTOR OF PHILOSOPHY
IN
CHEMICAL ENGINEERING

JANUARY 2016

Approval of the thesis:

COMPUTATIONAL INVESTIGATION OF HYDRODYNAMICS OF VISCOELASTIC FLUIDS FLOWING AROUND SQUARE CYLINDER AND COMPLEX FLUID RHEOLOGY VIA MAGNETIC RESONANCE IMAGING

submitted by **GÜLER BENGÜSU TEZEL** in partial fulfillment of the requirements for the degree of **Doctor of Philosophy in Chemical Engineering Department, Middle East Technical University** by,

Prof. Dr. Gülbin Dural Ünver
Dean, Graduate School of **Natural and Applied Sciences** ________________

Prof. Dr. Halil Kalıpçılar
Head of Department, **Chemical Engineering** ________________

Prof. Dr. Yusuf Uludağ
Supervisor,**Chemical Engineering Dept., METU** ________________

Assoc. Prof. Dr. Kerim Yapıcı
Co-Supervisor, **Nanotechnology Eng. Dept., Cumhuriyet Uni.** ______________

Examining Committee Members:

Prof. Dr. Bülent Karasözen
Mathematics Dept & Inst. of Applied Mathematics., METU ________________

Prof. Dr. Yusuf Uludağ
Chemical Engineering Dept., METU ________________

Prof. Dr. Göknur Bayram
Chemical Engineering Dept., METU ________________

Prof. Dr. Nihal Aydoğan
Chemical Engineering Dept., Hacettepe University ________________

Asst. Prof.Dr. Berna Topuz
Chemical Engineering Dept., Ankara University ________________

Date: 29.01.16

I hereby declare that all information in this document has been obtained and presented in accordance with academic rules and ethical conduct. I also declare that, as required by these rules and conduct, I have fully cited and referenced all material and results that are not original to this work.

Name, Last name: Güler Bengüsu Tezel

Signature :

ABSTRACT

COMPUTATIONAL INVESTIGATION OF HYDRODYNAMICS OF VISCOELASTIC FLUIDS FLOWING AROUND SQUARE CYLINDER AND COMPLEX FLUID RHEOLOGY VIA MAGNETIC RESONANCE IMAGING

Tezel, Güler Bengüsu
Ph.D., Department of Chemical Engineering
Supervisor: Prof. Dr. Yusuf Uludağ
Co-Supervisor: Assoc. Prof. Dr. Kerim Yapıcı

January 2016, 138 pages

The flow past bluff bodies, especially cylinders, have been an attraction in all kinds of fluid mechanical investigations for a long time. The analysis of external flow past a square cylinder is a key to various engineering applications such as shell and tube heat exchangers, coating processes, cooling towers, extruders and membrane processes. It involves complex phenomena like flow separation and reattachment, drag formation.

In the present study, the main objective is to investigate flow of a viscoelastic fluid around a confined square obstacle computationally. Phan-Thien Tanner (PTT) and Oldroyd-B are used as constitutive viscoelastic fluid models. Finite volume method is employed to solve coupled equations of continuity, motion and constitutive model along with appropriate boundary conditions. The stress terms in the momentum and constitutive equations are approximated by a higher-order and bounded scheme of

Convergent and Universally Bounded Interpolation Scheme for the Treatment of Advection (CUBISTA) to get accurate numerical solutions.

Effects of inertia in terms of Reynolds number *Re*, elasticity in terms of Weissenberg number, *We*, and constitutive equation parameters on the recirculation length, drag coefficients, *Cd* and on the flow field in terms of stress and velocity fields are examined and presented in detail. Differences between the behavior of Newtonian and viscoelastic fluids flowing such over square cylinder as the normal stress effects are highlighted.

In order to verify the computational methodology employed, Particle Image Velocimetry technique was used to get velocity field around the immersed cylinder in the case of Newtonian fluid. Experimental measurements and computational results compared well qualitatively.

Online and offline rheological measurements on complex fluid such as Carboxylmethyl cellulose, and Carbopol solutions fluid flow is presented in detail. Magnetic Resonance Imaging (MRI) are used for online measurements.

Keywords: Square cylinder; PTT fluid; Oldroyd-B fluid; Finite volume method; CUBISTA; MRI

ÖZ

KARE KESİTLİ SİLİNDİR ETRAFINDAKİ VİSKOELASTİK AKIŞ DİNAMİĞİNİN SAYISAL OLARAK İNCELENMESİ VE KARMAŞIK AKIŞKAN REOLOJİSİNİN MANYETİK REZONANS İLE GÖRÜNTÜLENMESİ

Tezel, Güler Bengüsu
Doktora, Kimya Mühendisliği Bölümü Tez
Yöneticisi: Prof. Dr. Yusuf Uludağ Yardımcı
Tez Yöneticisi: Doç. Dr. Kerim Yapıcı

Ocak 2016, 138 sayfa

Akışa dik olan, özellikle, kare kesitli silindir yüzeyler üzerinden olan akışlar, akışkan mekaniği çalışmalarında uzun süredir ilgi çekmektedir. Kare kesitli silindir üzerinden olan akış, çeşitli ısı değiştiricilerde, kaplama ve zar süreçlerinde, ekstruder gibi mühendislik uygulamalarında önemli rol almaktadır. Bu tür akışlar, akış ayrılması, girdap ve sürüklenme oluşumları gibi karmaşık olaylar içermektedir.

Bu çalışmanın temel amacı viskoelastik akışkanların sınırlandırılmış kare kesitli silindir üzerinden olan akışlarının sayısal olarak incelenmesidir. Phan-Thien Tanner (PTT) ve Oldroyd-B viskoelastik yardımcı gerilim eşitlikleri kullanılmıştır. Sonlu hacimler methodu uygun olan sınır koşulları ile birlikte, birbirlerine kuvvetli bağlı süreklilik, hız ve yardımcı gerilim eşitliklerini çözümlemek için kullanılmıştır. Hız ve yardımcı gerilim eşitliklerindeki, konveksiyon terimleri için yüksek dereceli ve sınırlandırılmış CUBISTA şeması, hassas sayısal çözüm eldesi için kullanılmıştır.

Bu çalışmada, Reynolds sayılarının, elastisitenin ölçüsü olarak Weissenberg sayılarının ve de yardımcı gerilim eşitliklerindeki parametrelerin, akış alanındaki hız ve gerilim bileşenlerine, devir-daim uzaklığına, sürüklenme katsayısılarına olan etkileri detaylıca incelenmiş ve sunulmuştur. Newtonumsu ve viskoelastik akışkanların karesel silindir üzerinden olan, normal gerilim bileşenlerinden kaynaklı davranış farklılıkları vurgulanmıştır.

Sayısal yöntemi doğrulamak için, Newtonumsu akışkan içerisine daldırılmış silindir etrafındaki hız alanı, Parçacık Görüntüleme Hız tekniği kullanılarak incelenmiştir. Deneysel ölçümlerin ve sayısal sonuçların nitekliksel olarak gayet uyumlu olduğu görülmüştür.

Karboksimetil selüloz ve Carbopol gibi karmaşık yapıdaki çözeltilerin dinamik ve durağan reolojik ölçümleri detaylı bir şekilde sunulmuştur. Dinamik ölçümlerde, Manyetik Rezonans Görüntüleme tekniği kullanılmıştır.

Anahtar Kelimeler: Kare kesitli silindir; PTT akışkan; Oldroyd-B akışkan; Sonlu Hacim Methodu; CUBISTA; MRI

To my father, Faruk Tezel…

ACKNOWLEDGEMENTS

First and foremost, my deepest gratitude is to my supervisor Prof. Dr. Yusuf Uludağ for his valuable suggestion, understanding and encouragement throughout this study and guidance throughout my study. I express sincere appreciation to Assoc. Dr. Kerim Yapıcı for his endless support and insight through the study. I have been privileged to have an advisor and a co-advisor who gave me the freedom to explore on my own.

I would like to express sincere thanks to Prof. Dr. Michael J. McCarthy and Prof. Dr. Kathyrn L. McCarthy for their great support, hospitality, kindness, and providing a great laboratory environment during my research at University of California, Davis.

I would like to thank also Prof. Dr. Göknur Bayram for her helps and supports in my study and in my teaching asistant life.

I would like to thank METU ÖYP Research Fund Project, (BAP-08-11-DPT.2011K1211010) for experimental and financial support during research.

I owe a debt of gratitude to my colleague friend Okan Özkök for his support and invaluable assistance. I would also like to thank my special friends Gülsüm Çaylan, Dr. Sibel Uzuner, Cemre Avşar, Burçin İkizer, Özgen Yalçın for their friendship and valuable stimuli that made me focus on my work.

I wish to express my deepest thanks to my parents, Sevinç- Faruk Tezel and my sister, Bilgesu Tezel and also my grandmother Elif Güler for their great support and patience throughout my all education. I would like to thank them for always believing in me.

Last but not least, I would like to express my deepest thanks and love to my spouse, Mustafa Tanrısever for his encouragement and moral support to me and for being with me all the time. Life would be boring without you.

TABLE OF CONTENTS

LIST OF TABLES

TABLES

LIST OF FIGURES

FIGURES

NOMENCLATURE

b	Height of the square
H	Height of the channel
B	Blockage ratio of the channel
L	Length of the channel
H	Characteristic length
Cd	Drag coefficient
U	Characteristic velocity
Lr	Recirculation Length
u	Horizontal velocity
v	Vertical velocity
V	Volume
p	Pressure
w_r	Polymer contribution viscosity
x	Rectangular coordinates of x-direction
y	Rectangular coordinates of y-direction

Greek Letters:

β	Ratio of retardation and relaxation time
ρ	Density
η_0	Total viscosity
η_s	Solvent viscosity
ε	Elongational parameter
Γ	Diffusion coefficient
ω	Vorticity

ω	Vorticity
ψ	Stream function
Φ	Dependent variable
λ	Relaxation time
τ	Stress tensor

Subscripts:

i	i^{th} component
j	j^{th} component
min	Minumum
max	Maximum
E, e	East face of control volume
N, n	North face of control volume
S, s	South face of control volume
W, w	West face of control volume

Superscripts:

0	Previous iteration value
T	Transpose

Abbreviations:

CD	Central Differences scheme
FV	Finite Volume
PTT	Phan-Thien-Tanner
Re	Reynolds number
S	Source term

SIMPLE	Semi-Implicit Method for Pressure Linked Equation
UCM	Upper Convected Maxwell
TDMA	Tridiagonal Matrix Algorithm
We	Weissenberg number

CHAPTER 1

INTRODUCTION

1.1. Scope of Thesis

Over the years, a voluminous body of knowledge has increased on the flow of fluids past cylinders of various cross sections. The bulk of the literature pertains to circular cylinders, followed by square, elliptic and rectangular cylinders or obstacles [1-3]. Indeed, even for the simplest shape of a circular cylinder which is free from geometrical singularities [4], the flow exhibits a rich variety of phenomena depending upon the nature of the mainstream flow (type of fluid Newtonian or non-Newtonian), blockage ratio of the cylinder (length to diameter ratio) and the characteristic Reynolds number of the flow.

The flow over square cylinders such as high-rise buildings according to aerodynamical characteristics, cooling towers, chimneys, tube banks in heat exchangers, in coating processes, in pipe and pump flows are encountered extensively in engineering applications. These objects, which under normal circumstances usually create an effective wake region behind the square cylinder. Understanding the flow field around these cylinders is important in many applications related with efficient use of energy [5] and structural design [6].

The behavior of a fluid flow past a square cylinder often has many complex phenomena such as flow separation, vortex shedding, recirculation length of wake flow (the flow path behind the square cylinder), distribution of the shear and normal profile around the solid surfaces of the square cylinder and, drag and lift force coefficients [4-6].

Majority of these studies in the literature deal with flow of a Newtonian fluid around a circular obstacle and to a smaller extend, around a square obstacle. For example Breuer et al. [7] examined laminar Newtonian flow around a square cylinder in a 2D channel using two different computational techniques, finite volume and lattice-Boltzmann automata. Their blockage ratio *B*, defined as the ratio between the obstacle dimension and channel height, was 1/8. They compared the results of the techniques in terms of velocity field, drag coefficient, *Cd*, recirculation length and Strouhal number. They observed an excellent agreement between the results of the techniques.

A numerical study to investigate Newtonian flow past a square cylinder for Reynolds numbers $Re \leq 40$ was conducted by Sen et al. [8] using a stabilized finite-element formulation with a non-uniform structured mesh. In order to mimic an unconfined flow, a small blockage ratio, B =1/100, was employed. For comparison purposes they also used cylinders of elliptical and circular cross-sections. They investigated impact of *Re* on the flow separation angle and *Cd*. They found that, flow separation over the square cylinder occurs at a smaller *Re* compared to the other cylinders giving rise to the highest *Cd* among the investigated obstacles.

The flow structures and wake flow characteristics, vortex shedding behavior of behind square cylinder at high Reynolds numbers were experimentally studied using particle image velocimetry (PIV) [36] with different blockage ratios by Biswas et al. [9]. They employed the two-dimensions flow past a stationary square cylinder at zero incidence for Reynolds number, $Re \leqslant 150$ using a stabilized finite-element formulations. They also compared with a circular cylinder that the flow separated at a much lower *Re* from a square cylinder leading to the formation of a bigger wake. Consequently, at a given *Re,* the drag on a square cylinder was higher more than that on drag of a circular cylinder.

In spite of their important industrial implications, number of studies involving non-Newtonian fluids around enclosed obstacles is much smaller than those on Newtonian fluids in the literature. For example in their computational study Dhiman et al. [10] employed finite volume technique to investigate 2D flow of power-law fluids around a confined square cylinder. The fluids had index values between $0.5 \leq n \leq 2.0$. Their results revealed that the effects of *Re* and *B* on the size of the recirculation zone and on *Cd* were stronger than that of the power-law index.

In their other study Dhiman et al. [11] excluded the presence of channel wall while keeping the other parameters, such as *Re* and *n*, identical to their earlier study. They observed stronger impact of *n* on *Cd* at low values of *Re* compared to the elevated values of *Re*. Moreover, as the value of *n* gets closer to one or the shear thinning behavior gets weaker, *Cd* becomes smaller at a given *Re*.

Momentum and forced convection heat transfer characteristics for steady flow of shear-thinning and shear-thickening fluids past a square cylinder were investigated using finite difference based numerical solution for Reynolds number ($5 \leq Re \leq 40$) with blokage ratio 1/15 by Paliwal et al. [12]. They presented velocity and temperature fields around a square cylinder immersed in a streaming power liquid and also reported that shorter wake regions in shear thinning liquids and slightly larger recirculation lengths in shear-thickening media were observed in their flow patterns.

P. Koteswara Rao et al. [13] extended the results on momentum and heat transfer characteristics to highly shearthinning fluids, especially $n \leq 0.5$ at low Reynolds number. Fluid elements followed the contour of the square cylinder and flow remained attached to the surface. These works reveal that shear-thinning behavior increases both *Cd* and the rate of convective heat transfer from the square cylinder surface. Shear thinning behaviour not only delays the formation of a visible wake but the resulting wake is also somewhat shorter than that of Newtonian fluid case. The shear thickening, on the other hand, has exactly the opposite influence on wake formation.

In another computational study on the hydrodynamics of power-law fluids around a square cylinder, Ehsan et al. [14] analyzed the effects of n and Re on drag and lift coefficients, Strouhal number, stream functions and time-averaged velocities both at laminar and turbulent conditions. They reported the impact of n and Re on the flow hydrodynamics in detail. For example, they observed weaker dependence of Cd on n as the inertial effects in the flow gets stronger. Their other interesting finding was that at turbulent conditions, effect of Re on the flow appeared to be modest compared to that of power-law index n.

In their recent study Nilmarkar et al. [15] investigated 2D creeping flow of Bingham plastic fluids past a square cylinder of square section by using a finite element based solver, COMSOL Multiphysics. They reported the effect of Bingham number, Bi, on both various qualitative and quantitative features of the flow including size of the yielding and unyielding regions, stress and pressure fields. At elevated Bi yielding or fluid like regions in the flow shrank owing to the higher yielding stress to overcome. Their other major finding was the weaker dependence of investigated flow quantities on Bi at its elevated values.

In the case of non-Newtonian fluid flow around confined obstacles, the literature is dominated by the studies with generalized Newtonian model to capture shear thinning or thickening effects. On the other hand, investigating the effects of viscoelasticity [16-20] on the hydrodynamics of the flow around the obstacles has potentially crucial implications on many industrial applications. Therefore the absence of viscoelastic flows around various obstacles in the literature merits a study on the hydrodynamics of such industrially important flows to reveal both microscopic and macroscopic flow quantities.

1.2. Objective of Thesis

The objective of this study is to investigate flow of a viscoelastic fluid, a linear PTT fluid, and Oldroyd-B around a confined square obstacle computationally. Finite volume method is employed to solve coupled equations of continuity, motion and constitutive model along with appropriate boundary conditions. At high elasticity of viscoelastic flow, expressed via Weissenberg numbers, $We \geq 1$, exhibits severe stress boundary layers on sharp vicinity of square obstacle. Their presence also creates convergence problems for numerical algorithm. So, the stress terms in the constitutive equations are approximated by a higher-order and bounded scheme of Convergent and Universally Bounded Interpolation Scheme for the Treatment of Advection (CUBISTA) to get accurate numerical solutions.

Effects of inertia in terms of *Re*, elasticity in terms of Weissenberg number, *We*, and constitutive equation parameters on the recirculation length, drag coefficients, *Cd* and on the flow field in terms of stress and velocity fields are examined and presented in detail.

Another outcome of this study is related to the application of MRI rheometry on the measurement of complex fluid such as CMC (Carboxylmethyl cellulose), and Carbopol solutions flow. Online and offline rheological measurements on solutions is presented in detail. Magnetic Resonance Imaging (MRI) is used for online measurements.

1.3. Outline of Thesis

The study is divided into self-contained chapters, as follows.

Chapter 2 provides general background on numerical methodology and governing equations and constitutive equations of the system used in this work.

Chapter 3 reports investigation of Newtonian flow around the square cylinder with the effect of inertia on the developed finite volume code. This study prepares the ground for viscoelastic flow around the square cylinder. Experimental visualizations done by PIV also are presented in this section.

In Chapter 4 the effects of inertia and elasticity on viscoelastic flow (PTT and Oldroyd-B) around the square cylinder are investigated numerically. Stress fields and drag coefficients are presented and compared for both model in detail.

In Chapter 5, application of MRI rheometry on the measurement of complex fluid. This chapter is studies on rheological behaviour of non-Newtonian fluids. The fluids used are Power law and Herschel-Bulkley type.

Chapter 6 includes the main conclusions of this study and some recommendations for further work.

CHAPTER 2

GOVERNING EQUATIONS AND NUMERICAL METHODOLOGY

In this section numerical method used in the viscoelastic flow simulations are explained in detail. Flow geometry and boundary conditions and governing equations are also presented. Finite Volume (FV) method is used the integral form of the conservation equations, which are discretized over the control volumes. The stress terms in the constitutive equations are approximated by a higher-order and bounded scheme of Convergent and Universally Bounded Interpolation Scheme for the Treatment of Advection (CUBISTA).

2.1. Flow Geometry

In this study isothermal flow of a viscoelastic fluid over a 2D confined square cylinder is considered. The flow system is schematically depicted in Figure 2.1. The ratio between heights of the square and the channel, referred to as the blockage ratio, is 1/4 (b/H=1/4). In the computations the upstream region length is set as 1/6 of the total channel length, L to ensure fully developed flow region. The ratio between channel length and height was set as L/H=30.

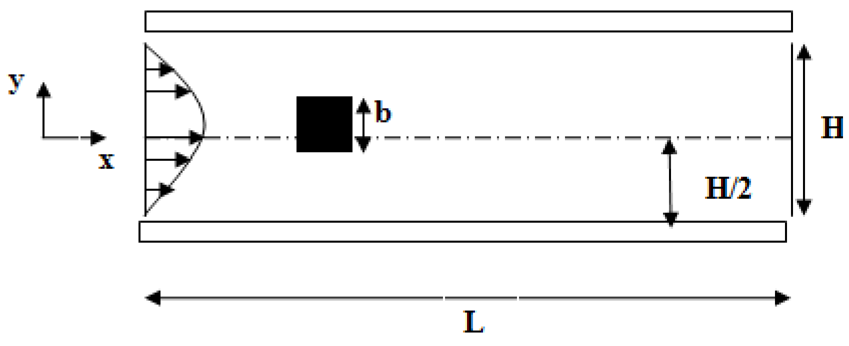

Figure 2.1 Schematic of 2D flow around a square cylinder

The formulation of the flow begins by considering basic equations of fluid flow, i.e. continuity and momentum equations given below.

$$\nabla . u = 0 \tag{2.1}$$

$$\rho \frac{\partial u}{\partial t} + \rho u . \nabla u = -\nabla p + \nabla . \tau + \beta \eta_0 \nabla^2 u \tag{2.2}$$

where u is the velocity, p is the pressure, η_0 is the total viscosity and τ represents the polymer or non-Newtonian contribution to the deviatoric stress tensor. The constant β is the ratio between the solvent viscosity and the total viscosity ($\beta = \eta_s / \eta_0$). A viscoelastic constitutive model provides the additional relation needed to solve the conservation equations.

In this study, Oldroyd-B model (constant viscosity with elasticity) and the PTT model (shear thinning with elasticity) are used to capture viscoelasticity. Linear PTT model [21] and Oldroyd-B model [20, 22], given by Equations 2.3-5 are employed. Linear PTT model captures both shear thinning and normal stress effects in the flow. The PTT fluid model generally refers to a nonlinear viscoelastic equation derived by Phan-Thien and Tanner [23] using the network theory. Unlike other non-Newtonian fluids, a distinctive advantage of PTT model is the inclusion of an extensional parameter, (ε). In this study, the extensional parameter is considered $\varepsilon \geq 0$, as a constant. The extensional parameter imposes an upper bound on the extensional viscosity which is inversely proportional to ε [24, 25]. It is worth mentioning that ε=0.25 in the PTT model correspond to the flow behavior of extremities for concentrated polymer melts polymer solutions [25].

The linear PTT model:

$$\lambda\left[\frac{\partial u}{\partial t}+\nabla.u\tau\right]+f(Tr\tau)\tau=\eta_p(\nabla u+\nabla u^T)+\lambda(\tau.\nabla u+\nabla u^T.\tau) \tag{2.3}$$

$$f(tr(\tau))=1+\frac{\varepsilon\lambda}{\eta_p}tr(\tau) \tag{2.4}$$

The Oldroyd-B model:

$$\lambda\left[\frac{\partial u}{\partial t}+\nabla.u\tau\right]+\tau=\eta_p(\nabla u+\nabla u^T)+\lambda(\tau.\nabla u+\nabla u^T.\tau) \tag{2.5}$$

where η_p is the zero shear rate viscosity for viscoelastic flow contribution and τ is the extra stress tensor, λ is the relaxation time of flow. Total viscosity, η, $\eta=\eta_p+\eta_s$ is the sum of the viscoelastic flow contribution viscosity and solvent or Newtonian flow contribution viscosity parts.

2.2. Dimensionless Form of Governing Equations

The set of equations which are derived above are converted into their dimensionless form by using the following dimensionless variables.

$$x^*=\frac{x}{H},\, y^*=\frac{y}{H},\, u^*=\frac{u}{U},\, p^*=\frac{pH}{\eta U},\, \tau^*=\frac{\tau H}{\eta U}$$

where *H* and *U* are the characteristic length and velocity in the flow, respectively. In the subsequent sections of the text, quantities without asterisk will be used to express dimensionless quantities for the sake of simplicity. For a two dimensional system of rectangular coordinates (x,y), the dimensionless steady state problem can be written as:

Continuity

$$\frac{\partial u}{\partial x}+\frac{\partial v}{\partial y}=0 \tag{2.6}$$

x–momentum

$$\frac{\partial}{\partial x}\left(\operatorname{Re} uu-\left(1-w_r\right)\frac{\partial u}{\partial x}\right)+\frac{\partial}{\partial y}\left(\operatorname{Re} vu-\left(1-w_r\right)\frac{\partial u}{\partial y}\right)=-\frac{\partial p}{\partial x}+\frac{\partial \tau_{xx}}{\partial x}+\frac{\partial \tau_{xy}}{\partial y} \tag{2.7}$$

y-momentum

$$\frac{\partial}{\partial x}\left(\operatorname{Re} uv-\left(1-w_r\right)\frac{\partial v}{\partial x}\right)+\frac{\partial}{\partial y}\left(\operatorname{Re} vv-\left(1-w_r\right)\frac{\partial v}{\partial y}\right)=-\frac{\partial p}{\partial y}+\frac{\partial \tau_{yy}}{\partial y}+\frac{\partial \tau_{xy}}{\partial x} \tag{2.8}$$

Dimensionless form of the stress components τ_{xx}, τ_{yy} and τ_{xy} are given through Equations 2.9-14.

Phan-Thien-Tanner (PTT) constitutive equation:

Stress components of τ_{xx}

$$\begin{aligned}\left(1+\varepsilon\frac{We}{w_r}\left(\tau_{xx}+\tau_{yy}\right)\right)\tau_{xx}+\frac{\partial}{\partial x}\left(Weu\tau_{xx}\right)+\frac{\partial}{\partial y}\left(Wev\tau_{xx}\right)=We\left(\frac{\partial u}{\partial y}-\frac{\partial v}{\partial x}\right)\tau_{xy}\\ +2We\frac{\partial u}{\partial x}\tau_{xx}+We\left(\frac{\partial u}{\partial y}+\frac{\partial v}{\partial x}\right)\tau_{xy}+2w_r\frac{\partial u}{\partial x}\end{aligned} \tag{2.9}$$

Stress components of τ_{yy}

$$\left(1+\varepsilon\frac{We}{w_r}\left(\tau_{xx}+\tau_{yy}\right)\right)\tau_{yy}+\frac{\partial}{\partial x}\left(Weu\tau_{yy}\right)+\frac{\partial}{\partial y}\left(Wev\tau_{yy}\right)=We\left(\frac{\partial v}{\partial x}-\frac{\partial u}{\partial y}\right)\tau_{xy}$$
$$+2We\frac{\partial v}{\partial y}\tau_{yy}+We\left(\frac{\partial u}{\partial y}+\frac{\partial v}{\partial x}\right)\tau_{xy}+2w_r\frac{\partial v}{\partial x} \qquad (2.10)$$

Stress components of τ_{xy}

$$\left(1+\varepsilon\frac{We}{w_r}\left(\tau_{xx}+\tau_{yy}\right)\right)\tau_{xy}+\frac{\partial}{\partial x}\left(Weu\tau_{xy}\right)+\frac{\partial}{\partial y}\left(Wev\tau_{xy}\right)$$
$$=-\frac{1}{2}We\left(\tau_{xx}-\tau_{yy}\right)\left(\frac{\partial u}{\partial y}-\frac{\partial v}{\partial x}\right)+w_r\left(\frac{\partial u}{\partial y}+\frac{\partial v}{\partial x}\right) \qquad (2.11)$$
$$+\frac{1}{2}We\left(\tau_{xx}+\tau_{yy}\right)\left(\frac{\partial u}{\partial y}+\frac{\partial v}{\partial x}\right)$$

Oldroyd-B constitutive equation:

Stress components of τ_{xx}

$$\tau_{xx}+\frac{\partial}{\partial x}\left(Weu\tau_{xx}\right)+\frac{\partial}{\partial y}\left(Wev\tau_{xx}\right)=We\left(\frac{\partial u}{\partial y}-\frac{\partial v}{\partial x}\right)\tau_{xy}+2We\frac{\partial u}{\partial x}\tau_{xx}$$
$$+We\left(\frac{\partial u}{\partial y}+\frac{\partial v}{\partial x}\right)\tau_{xy}+2w_r\frac{\partial u}{\partial x} \qquad (2.12)$$

Stress components of τ_{yy}

$$\tau_{yy}+\frac{\partial}{\partial x}\left(Weu\tau_{yy}\right)+\frac{\partial}{\partial y}\left(Wev\tau_{yy}\right)=We\left(\frac{\partial v}{\partial x}-\frac{\partial u}{\partial y}\right)\tau_{xy}+2We\frac{\partial v}{\partial y}\tau_{yy}$$
$$+We\left(\frac{\partial u}{\partial y}+\frac{\partial v}{\partial x}\right)\tau_{xy}+2w_r\frac{\partial v}{\partial x} \qquad (2.13)$$

Stress components of τ_{xy}

$$\tau_{xy}+\frac{\partial}{\partial x}\left(Weu\tau_{xy}\right)+\frac{\partial}{\partial y}\left(Wev\tau_{xy}\right)=-\frac{1}{2}We\left(\tau_{xx}-\tau_{yy}\right)\left(\frac{\partial u}{\partial y}-\frac{\partial v}{\partial x}\right)$$
$$+w_r\left(\frac{\partial u}{\partial y}+\frac{\partial v}{\partial x}\right) \qquad (2.14)$$
$$+\frac{1}{2}We\left(\tau_{xx}+\tau_{yy}\right)\left(\frac{\partial u}{\partial y}+\frac{\partial v}{\partial x}\right)$$

Where the Reynolds number and the Weissenberg number which is defined as the ratio of characteristic fluid relaxation time to characteristic time scale in the flow are given by

$$\mathrm{Re}=\frac{\rho UH}{\eta} \qquad (2.15)$$

$$We=\frac{\lambda U}{H} \qquad (2.16)$$

In this study, the material parameters β, extensibility parameter ε *a*nd polymer contribution viscosity ratio w_r are set as 0.2, 0.25 and 0.8, respectively. Extensibility parameter ε is zero for Oldroyd-B model.

2.3. Boundary conditions for flow domain

Use of appropriate boundary conditions is crucial to capture the physics of the flow. Due to the two-dimensional nature of flow, there is no flow in the *z*-direction and no flow variables depending upon the *z*-direction. The following inlet conditions are imposed for x and y-components of the velocity being u and v, respectively.

The imposed boundary conditions are:

$$u = 1 - \left|(1-0.5y)^2\right| \tag{2.17}$$

$$v = 0$$

$$0 \le y \le 4$$

No slip boundary condition at the channel and obstacle walls is imposed through:

$$\frac{\partial u}{\partial x} = 0, \frac{\partial v}{\partial x} = 0, \frac{\partial \tau_{xx}}{\partial x} = 0, \frac{\partial \tau_{yy}}{\partial x} = 0, \frac{\partial \tau_{xy}}{\partial x}, \frac{\partial P}{\partial x} = 0 \tag{2.18}$$

Outlet and inlet boundary stresses conditions : (2.19)

$$\tau_{xx} = 2We(1-\beta)\left(\frac{\partial u}{\partial y}\right)^2$$

$$\tau_{yy} = 0$$

$$\tau_{xy} = (1-\beta)\frac{\partial u}{\partial y}$$

At the channel wall stresses conditions: (2.20)

$$a = 1 + \varepsilon We(\tau_{xx} + \tau_{yy}) / \omega_r,$$

$$\tau_{xy} = (1-\beta)\frac{\partial u}{\partial y} / a$$

$$\tau_{xx} = 2We(1-\beta)\left(\frac{\partial u}{\partial y}\right)^2 / a$$

$$\tau_{yy} = 0$$

When “a” goes to 1, we get boundary conditions for Oldroyd-B model fluid, since the extensibility parameter ε is zero for Oldroyd-B model.

2.4. Finite Volume Method

In Finite Volume (FV) method the integral form of the conservation equations, which are discretized over the control volume, are used. The discretization of the governing set of PDEs given above is performed using Finite Volume method. Finite volume approximation of fluid flow systems is advantageous in terms of computer space and time requirements as well as in terms of numerical stability compared to the finite element method [26, 47].

Continuity, momentum and constitutive equations can be written in the general form as follows:

$$\frac{\partial}{\partial x}\left(\Lambda u\phi - \Gamma\frac{\partial \phi}{\partial x}\right) + \frac{\partial}{\partial y}\left(\Lambda u\phi - \Gamma\frac{\partial \phi}{\partial y}\right) = S_\phi \tag{2.21}$$

Convective flux term Diffusive flux term

where Λ is either density ρ or relaxation time λ, depending on the conservation or constitutive equation; ϕ is one of the dependent variables; Γ is the diffusion coefficient and S_ϕ is the source term. Corresponding dimensionless quantities of these variables are listed in Table 2.1.

Integrating Equation (2.21) over a control volume shown in Figure 2.2, the following equation can be obtained

$$\int_V \frac{\partial}{\partial x}\left(\Lambda u\phi - \Gamma\frac{\partial \phi}{\partial x}\right)dV + \int_V \left(\Lambda u\phi - \Gamma\frac{\partial \phi}{\partial y}\right)dV = \int_V S_\phi dV \tag{2.22}$$

Using the divergence theorem

$$\int_A \frac{\partial}{\partial x}\left(\Lambda u\phi - \Gamma\frac{\partial \phi}{\partial x}\right).\underline{n}\,dA + \int_A \left(\Lambda u\phi - \Gamma\frac{\partial \phi}{\partial y}\right).\underline{n}\,dA = \int_V S_\phi dV \tag{2.23}$$

where A is the surface enclosing volume V, and $\underline{n}$ is the unit vector normal to the surface. Integration of equation (2.23) gives

$$\begin{aligned}&\left\{\left[(\Lambda u\phi A)_e - (\Lambda u\phi A)_w\right] - \left[\Gamma_e A_e\left(\frac{\partial \phi}{\partial x}\right)_e - \Gamma_w A_w\left(\frac{\partial \phi}{\partial x}\right)_w\right]\right\}\\ &+\left\{\left[(\Lambda u\phi A)_n - (\Lambda u\phi A)_s\right] - \left[\Gamma_n A_n\left(\frac{\partial \phi}{\partial x}\right)_n - \Gamma_s A_s\left(\frac{\partial \phi}{\partial x}\right)_s\right]\right\} = S_\phi \Delta V\end{aligned} \tag{2.24}$$

where each quantity in the brackets is calculated on the corresponding face of the control volume.

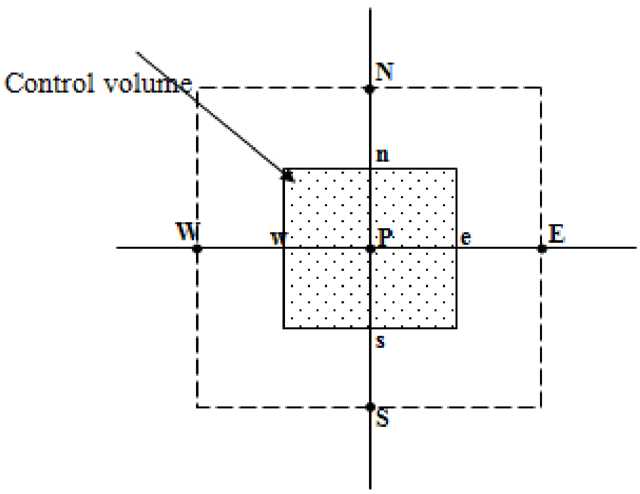

Figure 2.2 Schematic diagram of a control volume

Table 2.1 Finite volume method constants and functions for governing equations

Equation	Λ	Γ	S_ϕ
Continuity	1	0	0
u-momentum	*Re*	$1-\omega_r$	$-\frac{\partial p}{\partial x}+\frac{\partial \tau_{xx}}{\partial x}+\frac{\partial \tau_{xy}}{\partial y}$
v-momentum	Re	$1-\omega_r$	$-\frac{\partial p}{\partial y}+\frac{\partial \tau_{yy}}{\partial y}+\frac{\partial \tau_{xy}}{\partial x}$
			Linear PTT Model
Normal stress τ_{xx}	*We*	0	$We\left(\frac{\partial u}{\partial y}-\frac{\partial v}{\partial x}\right)\tau_{xy}+2We\frac{\partial u}{\partial x}\tau_{xx}+We\left(\frac{\partial u}{\partial y}+\frac{\partial v}{\partial x}\right)\tau_{xy}$ $+2w_r\frac{\partial u}{\partial x}-\left(1+\varepsilon\frac{We}{w_r}\left(\tau_{xx}+\tau_{yy}\right)\right)\tau_{xx}$
Normal stress τ_{yy}	*We*	0	$We\left(\frac{\partial v}{\partial x}-\frac{\partial u}{\partial y}\right)\tau_{xy}+2We\frac{\partial v}{\partial y}\tau_{yy}+We\left(\frac{\partial u}{\partial y}+\frac{\partial v}{\partial x}\right)\tau_{xy}+2w_r\frac{\partial v}{\partial x}$ $-\left(1+\varepsilon\frac{We}{w_r}\left(\tau_{xx}+\tau_{yy}\right)\right)\tau_{yy}$
Shear stress τ_{xy}	*We*	0	$-\frac{1}{2}We\left(\tau_{xx}-\tau_{yy}\right)\left(\frac{\partial u}{\partial y}-\frac{\partial v}{\partial x}\right)+w_r\left(\frac{\partial u}{\partial y}+\frac{\partial v}{\partial x}\right)$ $+\frac{1}{2}We\left(\tau_{xx}+\tau_{yy}\right)\left(\frac{\partial u}{\partial y}+\frac{\partial v}{\partial x}\right)-\left(1+\varepsilon\frac{We}{w_r}\left(\tau_{xx}+\tau_{yy}\right)\right)\tau_{xy}$
			Oldroyd-B Model
Normal stress τ_{xx}	*We*	0	$We\left(\frac{\partial u}{\partial y}-\frac{\partial v}{\partial x}\right)\tau_{xy}+2We\frac{\partial u}{\partial x}\tau_{xx}+We\left(\frac{\partial u}{\partial y}+\frac{\partial v}{\partial x}\right)\tau_{xy}+2w_r\frac{\partial u}{\partial x}-\tau_{xx}$
Normal stress τ_{yy}	We	0	$We\left(\frac{\partial v}{\partial x}-\frac{\partial u}{\partial y}\right)\tau_{xy}+2We\frac{\partial v}{\partial y}\tau_{yy}+We\left(\frac{\partial u}{\partial y}+\frac{\partial v}{\partial x}\right)\tau_{xy}+2w_r\frac{\partial v}{\partial x}-\tau_{yy}$
Shear stress τ_{xy}	*We*	0	$-\frac{1}{2}We\left(\tau_{xx}-\tau_{yy}\right)\left(\frac{\partial u}{\partial y}-\frac{\partial v}{\partial x}\right)+w_r\left(\frac{\partial u}{\partial y}+\frac{\partial v}{\partial x}\right)+\frac{1}{2}We\left(\tau_{xx}+\tau_{yy}\right)\left(\frac{\partial u}{\partial y}+\frac{\partial v}{\partial x}\right)-\tau_{xy}$

2.5. Discretization of Governing Equations

There are two kinds of grid arrangements used in being staggered grids and nonstaggered or collocated grids to supply discretization of equations [27]. In staggered grid arrangements stress components τ_{xx} and τ_{yy} are located at the center of the control volume depicted in Figure 2.3, while generally τ_{xy} is located at the corners and velocities are placed on the faces of the control volume. Whereas in collocated grids, all flow variables are located at the center of the control volumes. The coefficients in the discretization equations are identical for all velocities for collocated grids, pressure derivatives show zig-zag pressure distribution. It causes divergence of numerical solution and decreases numerical stability.

Staggered grid was used to discretize the governing the set of governing equations as shown in Figure 2.4. In staggered grid arrangement, the velocity components of u, v (u_i,v_i) are distributed around the pressure points, p. This layout has the advantage that, when multiplied by the cell face area, the velocity components give the exact volume fluxes and this leads to a simplified mass balance computation and results in fully-coupled velocity and pressure fields. To avoid checkerboard or zig-zag pressure distribution, staggered grid arrangements are also preferred in study.

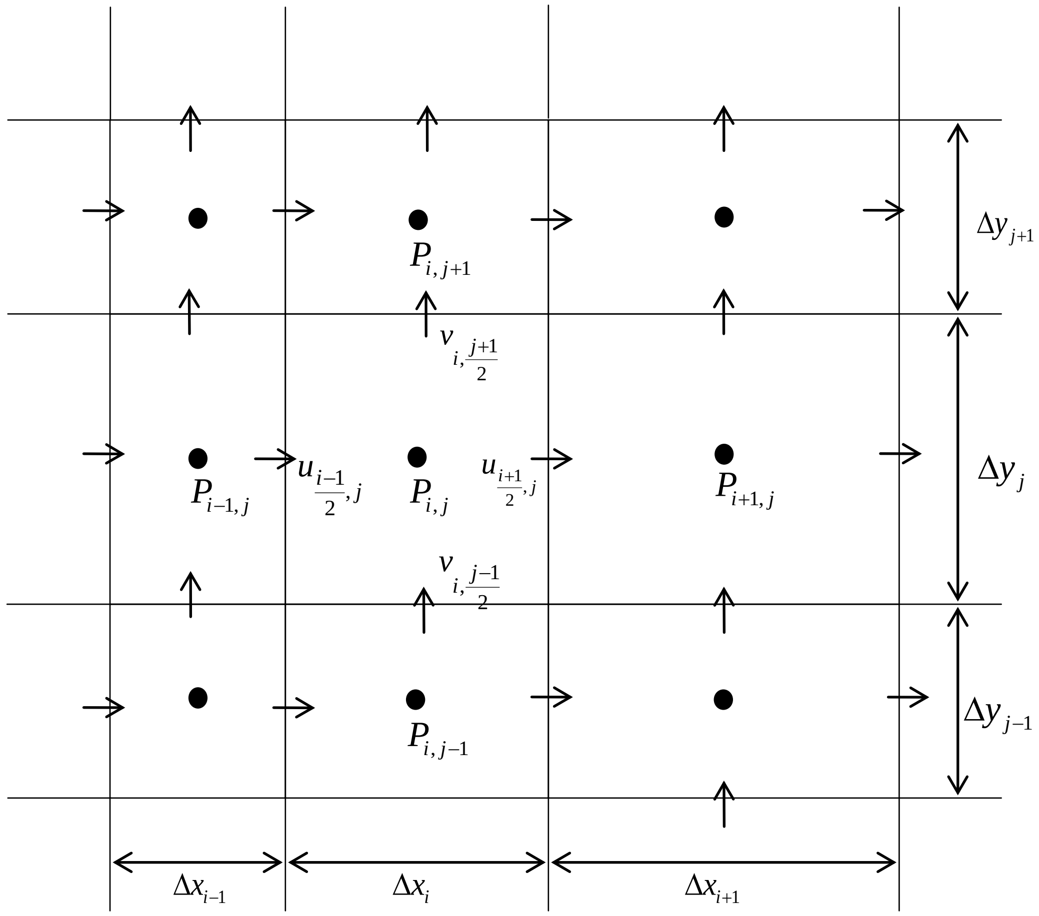

Figure 2.3 Flow variables on staggered grid arrangements

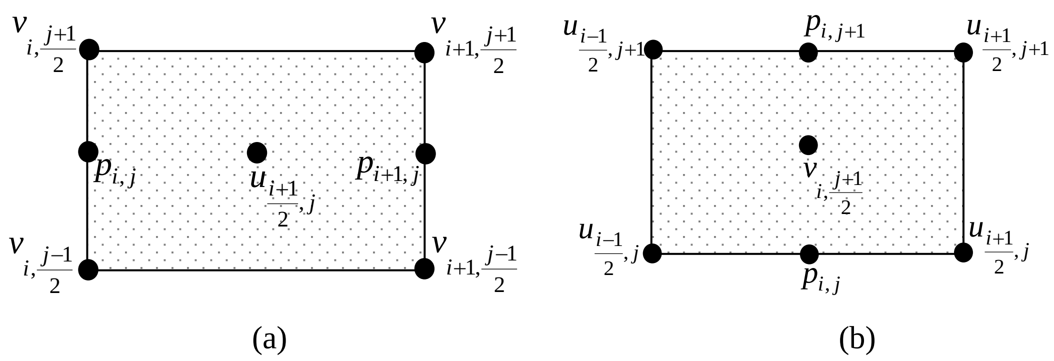

Figure 2.4 (a) u-momentum control volume cell (b) v-momentum control volume cell on staggered grid arrangement

2.5.1. Second Order Central Difference Scheme

Central difference scheme is used for the approximation of the gradients in Equation 2.24 which is associated with the diffusion term. Then the equation can be expressed as follows:

East Face :

$$\Gamma_e A_e \left(\frac{\partial \phi}{\partial x}\right)_e = \left(\frac{1}{\mathrm{Re}}\right)\frac{(y_n - y_s)}{(x_E - x_P)}(\phi_E - \phi_P) = D_e(\phi_E - \phi_P) \tag{2.25}$$

West Face:

$$\Gamma_w A_w \left(\frac{\partial \phi}{\partial x}\right)_w = \left(\frac{1}{\mathrm{Re}}\right)\frac{(y_n - y_s)}{(x_P - x_W)}(\phi_P - \phi_W) = D_w(\phi_P - \phi_W) \tag{2.26}$$

North Face:

$$\Gamma_n A_n \left(\frac{\partial \phi}{\partial x}\right)_n = \left(\frac{1}{\mathrm{Re}}\right)\frac{(x_e - x_w)}{(y_N - y_P)}(\phi_N - \phi_P) = D_n(\phi_N - \phi_P) \tag{2.27}$$

South Face:

$$\Gamma_s A_s \left(\frac{\partial \phi}{\partial x}\right)_s = \left(\frac{1}{\mathrm{Re}}\right)\frac{(x_e - x_w)}{(y_P - y_S)}(\phi_P - \phi_S) = D_s(\phi_P - \phi_S) \tag{2.28}$$

A new symbol, *F*, for the convective terms in equation is inserted into Equation 2.24 for the sake of convenience as follows:

$$F_e = \mathrm{Re}\, u_e A_e \qquad F_w = \mathrm{Re}\, u_w A_w \tag{2.29}$$

$$F_n = \mathrm{Re}\, u_n A_n \qquad F_s = \mathrm{Re}\, u_s A_s \tag{2.30}$$

"*F*" can be considered as a coefficient of the cell face convective fluxes. Equations 2.25 to 2.30 are inserted in to the Equation 2.24 to yield the following the convection-diffusion equations:

$$\begin{aligned}&\{[F_e\phi_e - F_w\phi_w] - [D_e(\phi_E - \phi_P) - D_w(\phi_P - \phi_W)]\}\\&+\{[F_n\phi_n - F_s\phi_s] - [D_n(\phi_N - \phi_P) - D_s(\phi_P - \phi_S)]\} = S_\phi \Delta V\end{aligned} \tag{2.31}$$

The next step is to solve the set of algebraic equations which are non-linear due to the source term in the constitutive equations. To make the equations linear, first, source term S_ϕ is assumed to be a linear function of variable ϕ such that,

$$S_\phi = S_C + S_P\phi_P \tag{2.32}$$

where S_C is constant part of the S_ϕ that is independent of ϕ while S_P is the coefficient of ϕ_P which is set as negative to enhance the numerical stability [24].

2.5.2. Convergent and Universally Bounded Interpolation (CUBISTA) Scheme

Convective terms in the constitutive equations are approximated by at least second-order accurate, bounded and non-uniform version of CUBISTA scheme using dimensionless form of given in Equation 2.34. This scheme is preferred due to its documented advantages on the higher order schemes when viscoelastic fluids are considered [29,33]. Mathematical expression of CUBISTA scheme proposed by Alves et al. [28] is given in Equation 2.35 for a nonuniform mesh structure. The implementation of the CUBISTA scheme is carried out via deferred correction method that was proposed by Khosla and Rubin [30]. To ensure stability of the higher-order schemes, a well known and widely used technique, the "deferred correction," [25] is used for the evaluation of the variables at the faces of the control volumes. Mathematically this technique may be stated as;

$$\phi_f = \phi_{LO} + (\phi_{HO} - \phi_{LO})^0 \tag{2.33}$$

The first term in Equation 2.33 is the result from the low order (LO) scheme, and is used to evaluate the coefficient of the discretized equation. The other term is obtained at the previous iteration, and is used in the source term. Upwind Differencing Scheme (UDS) [31] is used to handle the first term in Equation 2.33. High order (HO) results are also obtained using Equation 2.34. The corresponding matrix coefficients are therefore always diagonally dominant. The purpose of the convection scheme use is then to specify the values of ϕ_f (ϕ_w, ϕ_e) at the face, based on existing values at the neighbouring cell centres, ϕ_c (ϕ_P) as in Figure 2.5.

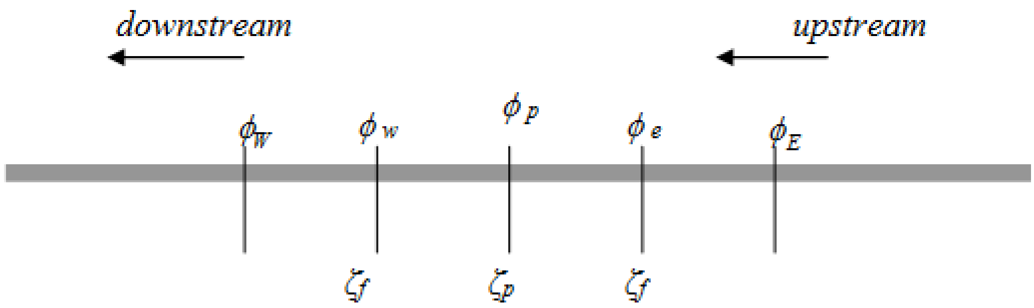

Figure 2.5 General representation for grid points in the x direction one dimensional Cubista

$$\phi_f = \begin{cases} \frac{7}{4}\phi_C & 0 < \phi_C < \frac{3}{8} \\ \frac{3}{4}\phi_C + \frac{3}{8} & \frac{3}{8} \le \phi_C < \frac{3}{4} \\ \frac{1}{4}\phi_C + \frac{3}{4} & \frac{3}{4} < \phi_C < 1 \\ \phi_C & \text{elsewhere } (\phi_C > 1 \text{ or } \phi_C < 0) \end{cases} \tag{2.34}$$

The simplest scheme satisfying the transportive property is upwind, whereby $\phi_f = \phi_P$ where P is the cell centre situated on the upwind side in relation to face f (measured by $F_f > 0$). Upwind differencing is a first-order scheme. The UDS [31] is unconditionally bounded and highly stable. But it may produce severe numerical diffusion due to its first order accuracy. Besides, for the differential constitutive equations found in viscoelastic flows, which do not have a diffusion-like term, upwind scheme is too inaccurate because it introduces excessive numerical diffusion errors in the solution. So, we need higher order and stable scheme to discretize convection terms in the governing equations. Equation 2.35 is more generalized form of CUBISTA in the normalized coordinates to handle the non-uniform meshes.

$$\hat{\phi}_f = \begin{cases} \left(1 + \dfrac{\hat{\xi}_f - \hat{\xi}_P}{3\left(1-\hat{\xi}_P\right)}\right)\dfrac{\hat{\xi}_f}{\hat{\xi}_P}\hat{\phi}_P & 0 < \hat{\phi}_P < \dfrac{3}{4}\hat{\xi}_P \\ \dfrac{\hat{\xi}_f\left(1-\hat{\xi}_f\right)}{\hat{\xi}_P\left(1-\hat{\xi}_P\right)}\hat{\phi}_P + \dfrac{\hat{\xi}_f\left(\hat{\xi}_f - \hat{\xi}_P\right)}{\left(1-\hat{\xi}_P\right)} & \dfrac{3}{4}\hat{\xi}_P \le \hat{\phi}_P \le \dfrac{1+2\left(\hat{\xi}_f - \hat{\xi}_P\right)}{2\hat{\xi}_f - \hat{\xi}_P}\hat{\xi}_P \\ 1 - \dfrac{\left(1-\hat{\xi}_f\right)}{2\left(1-\hat{\xi}_P\right)}\left(1-\hat{\phi}_P\right) & \dfrac{1+2\left(\hat{\xi}_f - \hat{\xi}_P\right)}{2\hat{\xi}_f - \hat{\xi}_P}\hat{\xi}_P < \hat{\phi}_P \\ \hat{\phi}_P & \text{elsewhere} \end{cases} \tag{2.35}$$

In this formulation the advacted variable $\hat{\phi}$ is normalized as;

$$\hat{\phi} = \frac{\phi - \phi_E}{\phi_E - \phi_W} \tag{2.36}$$

Normalized coordinates are given as followings:

$$\hat{\xi}_P = \frac{\xi_P - \xi_E}{\xi_E - \xi_W} \quad \hat{\xi}_f = \frac{\xi_f - \xi_E}{\xi_E - \xi_W} \tag{2.37}$$

Use of these in the Cubista equation yields the following expression for τ_{xx} where τ_{xxeP} is the face value of control cell as depicted in Figure 2.6.

$$\tau_{xxeP}=\begin{cases}\left(1+\dfrac{\hat{\xi}_f-\hat{\xi}_P}{3\left(1-\hat{\xi}_P\right)}\right)\dfrac{\hat{\xi}_f}{\hat{\xi}_P}\hat{\tau}_{xxP} & 0<\hat{\tau}_{xxP}<\dfrac{3}{4}\hat{\xi}_P\\ \dfrac{\hat{\xi}_f\left(1-\hat{\xi}_f\right)}{\hat{\xi}_P\left(1-\hat{\xi}_P\right)}\hat{\tau}_{xxP}+\dfrac{\hat{\xi}_f\left(\hat{\xi}_f-\hat{\xi}_P\right)}{\left(1-\hat{\xi}_P\right)} & \dfrac{3}{4}\hat{\xi}_P\le\hat{\tau}_{xxP}\le\dfrac{1+2\left(\hat{\xi}_f-\hat{\xi}_P\right)}{2\hat{\xi}_f-\hat{\xi}_P}\hat{\xi}_P\\ 1-\dfrac{\left(1-\hat{\xi}_f\right)}{2\left(1-\hat{\xi}_P\right)}\left(1-\hat{\tau}_{xxP}\right) & \dfrac{1+2\left(\hat{\xi}_f-\hat{\xi}_P\right)}{2\hat{\xi}_f-\hat{\xi}_P}\hat{\xi}_P<\hat{\tau}_{xxP}\\ \hat{\tau}_{xxP} & \text{elsewhere}\end{cases}\tag{2.38}$$

Where;

$$\hat{\tau}_{xxP}=\frac{\tau_{xxP}-\tau_{xxW}}{\tau_{xxE}-\tau_{xxW}}$$

It should be noted that, details of the discretisation of τ_{xx} are provided. For the other components of the stress, the same methodology is employed. Definition of normalized coordinates in Cubista functions, when ζ goes to x according to our nomenclature in Equation 2.38 as follows:

$$\hat{\xi}_P=\frac{x_P-x_E}{x_E-x_W}\qquad\hat{\xi}_f=\frac{x_e-x_E}{x_E-x_W}$$

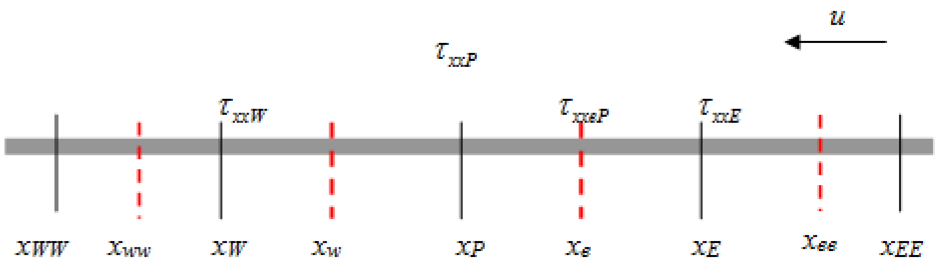

Figure 2.6 General representation for grid points in the x direction as one dimensional Cubista. Dashed lines represent face values of the control volume cells.

After getting τ_{xx} components in all faces (τ_{xxe}, τ_{xxw} , τ_{xxn}, τ_{xxs}) using the bounded CUBISTA scheme, they are expressed in their matrix form as in Equation 2.42. Discretization of the PTT constitutive equation by using CUBISTA scheme is given through Equations 2.39-45. Two dimensional discretised model equations over the control volume can be expressed symbolically as follows for τ_{xx} :

$$\{[F_e\tau_{xxe} - F_w\tau_{xxw}]\} + \{[F_n\tau_{xxn} - F_s\tau_{xxs}]\} = S_\phi \Delta V \qquad (2.39)$$

where F_e, F_w, F_n and F_s, are convective terms that are defined as in Equation 2.40.

$$F_e = Weu_{i,j}(y_n - y_s) \qquad F_n = Wev_{i,j}(x_e - x_w)$$
$$F_w = Weu_{i-1,j}(y_n - y_s) \qquad F_s = Wev_{i,j-1}(x_e - x_w) \qquad (2.40)$$

Discretized form of the Equation 2.39 is expressed as,

$$A_P\tau_{xxi,j} = A_E\tau_{xxi+1,j} + A_W\tau_{xxi-1,j} + A_N\tau_{xxi,j+1} + A_S\tau_{xxi,j-1} + b\tau_{xxi,j} \qquad (2.41)$$

where the coefficients are given by the through following relations for the case of CUBISTA scheme.

$$A_E = \max(-F_e, 0)$$

$$A_W = 0;$$

$$A_N = \max(-F_n, 0)$$

$$A_S = 0; \tag{2.42}$$

$$A_P = A_E + A_W + A_N + A_S + (F_e - F_w) + (F_n - F_s) + \max(F_w, 0)$$

$$+\max(F_s, 0) + (x_e - x_w)(y_n - y_s) + \varepsilon We(x_e - x_w)(y_n - y_s)(\tau_{xxi,j}{}^0 + \tau_{yyi,j}{}^0) / \omega r$$

Source terms in Equation 2.42 are given as follows in Equation 2.43-45.

Source term of τ_{xx} equations:

$$b\tau xx_{i,j} = 2We\frac{\partial u_{i,j}}{\partial x}\tau^0{}_{xxi,j}(x_e - x_w)(y_n - y_s) + 2\omega r\frac{\partial u_{i,j}}{\partial x}(x_e - x_w)(y_n - y_s) \tag{2.43}$$
$$+2We\frac{\partial u_{i,j}}{\partial y}\tau^0{}_{xyi,j}(x_e - x_w)(y_n - y_s) + \max(F_w, 0)\tau_{xxi-1,j}{}^0 + \max(F_s, 0)\tau_{xxi,j-1}{}^0$$

Source term of τ_{yy} equations:

$$b\tau_{yyi,j} = 2We\frac{\partial v_{i,j}}{\partial y}\tau^0{}_{yyi,j}(x_e - x_w)(y_n - y_s) + 2\omega r\frac{\partial v_{i,j}}{\partial y}(x_e - x_w)(y_n - y_s)$$
$$+2We\frac{\partial v_{i,j}}{\partial x}\tau^0{}_{xyi,j}(x_e - x_w)(y_n - y_s) + \max(F_w, 0)\tau_{yyi-1,j}{}^0 + \max(F_s, 0)\tau_{yyi,j-1}{}^0 \tag{2.44}$$

Source term of τ_{xy} equations:

$$b\tau_{xyi,j} = \frac{\partial v_{i,j}}{\partial x}(We\tau_{xxi,j}{}^{0} + \omega r)(x_e - x_w)(y_n - y_s) \tag{2.45}$$
$$+\frac{\partial u_{i,j}}{\partial y}(We\tau_{yyi,j}{}^{0} + \omega r)(x_e - x_w)(y_n - y_s) + \max(F_w, 0)\tau_{xyi-1,j}{}^{0} + \max(F_s, 0)\tau_{xyi,j-1}{}^{0}$$

where superscript 0 denotes the values obtained at previous iteration. Gradients of velocities are computed by central differences [26] and also they are solved using CUBISTA scheme at the related interior domain.

The SIMPLE [32] method is employed to solve the coupled system of the continuity, momentum and constitutive equations. The set of linearized algebraic equations are solved by using the Thomas algorithm or the tridiagonal matrix algorithm (TDMA). The solution process is reiterated until the maximum relative change of flow variables (u, v, p, τ_{xx}, τ_{yy}, τ_{xy}) are less then a prescribed tolerance or residual as:

$$res = MAX\left\{\frac{\left|\phi^{n+1} - \phi^{n}\right|}{\left|\phi^{n+1}\right|}\right\} \le 1x10^{-8} \tag{2.46}$$

where $\phi = \left(u, v, p, \tau_{xx}, \tau_{yy}, \tau_{xy}\right)^{T}$.

CHAPTER 3

STEADY NEWTONIAN FLOW AROUND SQUARE OBSTACLE

The confined flow of a Newtonian fluid around a square cylinder mounted in a rectangular channel (blockage ratio B=1/4) was investigated both numerically and experimentally. The flow variables including streamlines, vorticity and drag coefficients were calculated at $0 \leq Re \leq 50$ using finite volume method. Particle image velocimetry (PIV) was also used to obtain the two-dimensional velocity field. The flow measurements were conducted for $1 \leq Re \leq 100$. Streamline and vorticity results obtained by PIV are compared with those of the numerical simulations.

3.1. Introduction

The flow past bluff bodies have been an attraction in all kinds of fluid mechanical investigations for a long time. The analysis of external flow past a square cylinder is a key to various engineering applications such as shell and tube heat exchangers, coating processes, cooling towers, extruders and membrane processes [28]. It involves complex phenomena like flow separation and reattachment, drag formation. Most experimental [29] and numerical studies concerning the external flow past a stationary square cylinder have been carried out at moderate to high Reynolds numbers. In this regime, the flow is unsteady. There are also many steady flow studies on square cylinders.

Characteristics of the steady confined flow past a square cylinder have been reported by Breuer et al. [7]. They presented results for Re=0.5–300 in two-dimensions. The results were computed via finite-volume and lattice-Boltzmann simulations. A blockage of 1/8 was used. Separation was not observed for Re<1. Gupta et al. [34]

employed the finite difference method and studied the steady flow and heat transfer characteristics in conjunction with the power-law fluids for *Re*=5–40 and *B*=1/8. Sharma and Eswaran [35] presented results for *B*=1/20 and *Re*=1−160 by using a finite-volume formulation. These studies are related to the physics of the Newtonian flow past a square cylinder and the accuracy of numerical predictions of simulations.

The results of the theoretical studies (especially numerical simulations) on fluid flow mechanics should be evaluated with respect to the experimental studies performed at similar conditions. In this study, Particle Image Velocimetry (PIV) is used to carry out flow field measurements experimentally. PIV has been used for both Newtonian and non-Newtonian fluid flow measurements [36]. This technique enables the qualitative and quantative flow visualization by means of accurate measurement at multiple points over the entire flow.

In this study, Newtonian flow around square cylinder with *B*=1/4 analyzed by developing non-uniform staggered 372x162 grids on finite volume code as in Figure 3.1. Objective of this chapter is twofold. One is to obtain accurate numerical solutions of the system providing a background for complex flow simulations. The other one is to compare and verify to the corresponding results in literature.

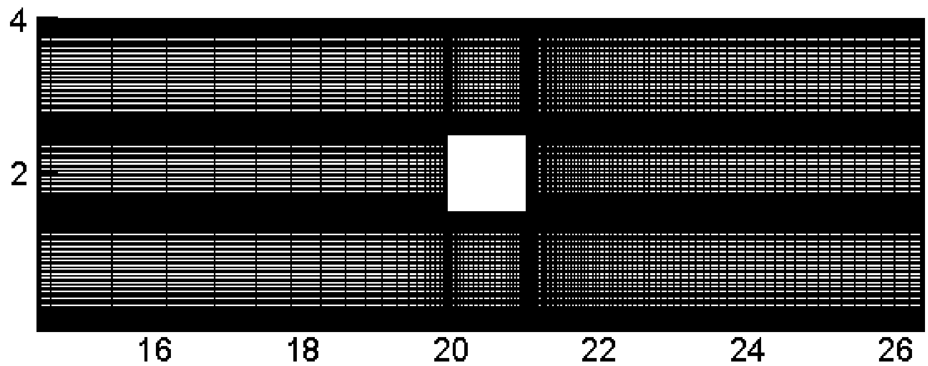

Figure 3.1 Non-uniform mesh around the obstacle with minimum cell size of $\Delta x= 0.02$ and $\Delta y= 0.01$ for B=1/4.

3.2. Numerical Results and Discussion

Streamline profiles calculated in around the cylinder are shown in Figures 3.2a-d. The series of profiles illustrates how the wake gradually decreases in intensity and spreads laterally with increasing distance from the cylinder. Near the cylinder the profiles are quite similar but there are growing differences further downstream, indicating the greater development of the wake as the Reynolds number increases from 0 to 50. The length of the vortex pair obtained also increased with growing wake region as in Figures 3.2c-d.

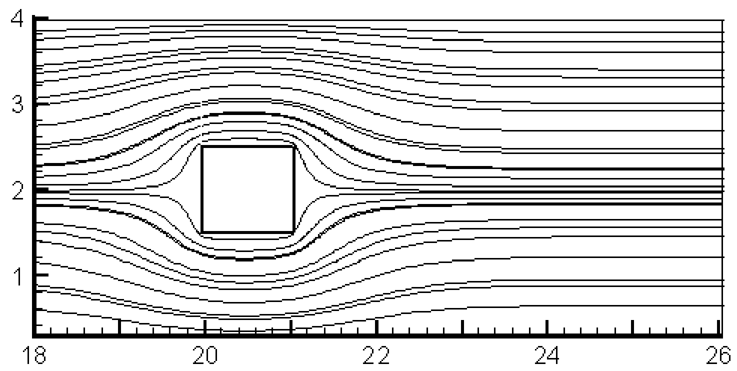

(a)

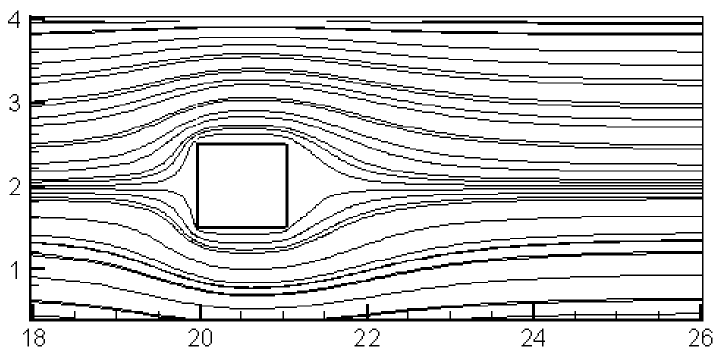

(b)

Figure 3.2 Streamlines around the square cylinder for different Reynolds numbers (a)*Re*=0 (b)*Re*=10 (c)*Re*=30 (d)*Re*=50.

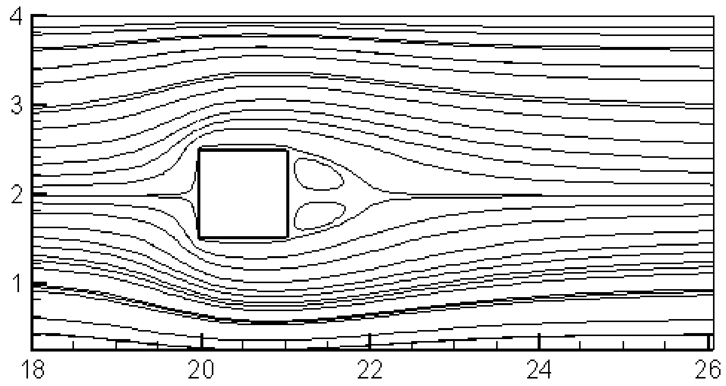

(c)

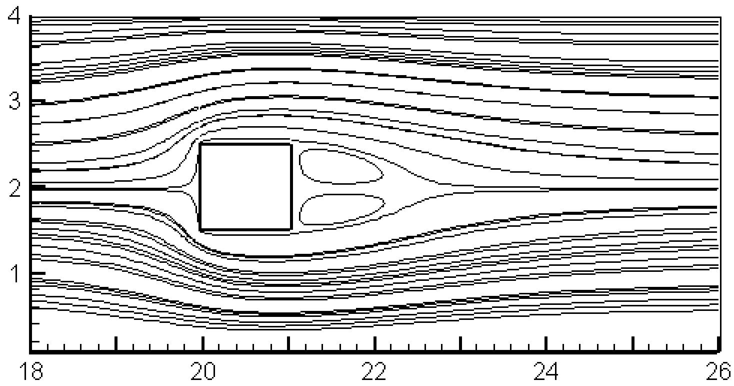

(d)

Figure 3.2 Streamlines around the square cylinder for different Reynolds numbers (a)*Re*=0 (b)*Re*=10 (c)*Re*=30 (d)*Re*=50 (continued).

Figures 3.3-5 show velocity profiles of streamwise or x-component velocity (u) and vertical velocity (v) along the centerline of the channel (y=2) at *Re*=0, 10, 30, 50. After x=21 position, wake region, asymmetric velocity distribution is obtained with increased *Re* numbers in Figure 3.3 due to dominancy of inertial effects. Vertical velocity (y-component velocity) has sharp profile due to suddenly changed boundary conditions at the vicinity of obstacle (at singularity points). Figure 3.5 illustrates distribution of the velocity component, u at several positions of the flow field for *Re* numbers along the center line.

At x=19 that is the position of near cylinder region, the velocity profiles differs from Poiseuille flow. In the wake region, at x=22, maximum velocity point shifts with respect to increasing *Re*. This behavior can be attributed to the vortex formation behind of obstacle.

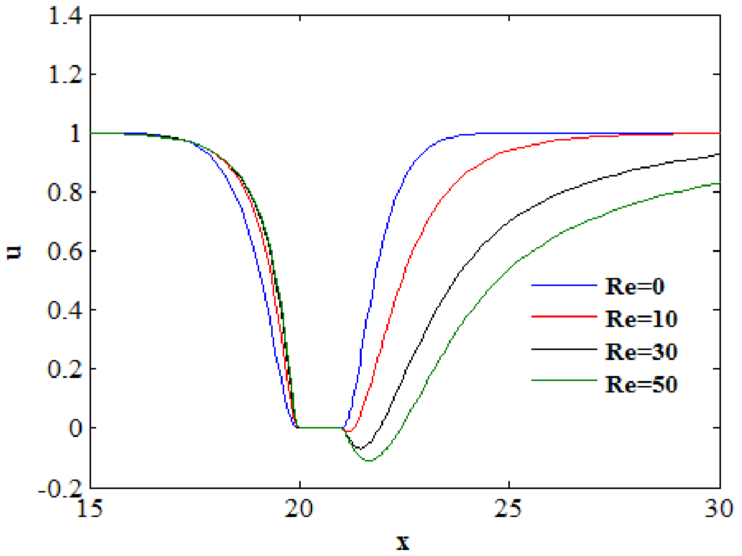

Figure 3.3 Streamwise (u) velocity along the centerline y=2 at *Re*=0, 10, 30, 50.

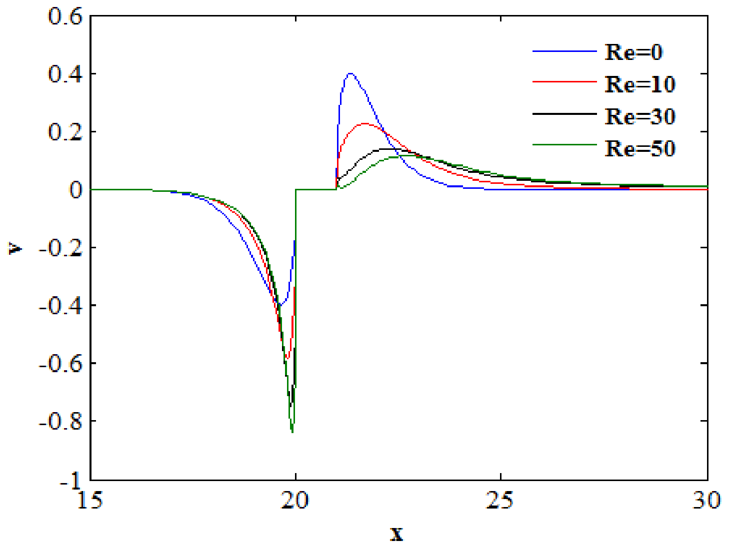

Figure 3.4 Vertical velocity (v) along the centerline y=2 at *Re*=0, 10, 30, 50.

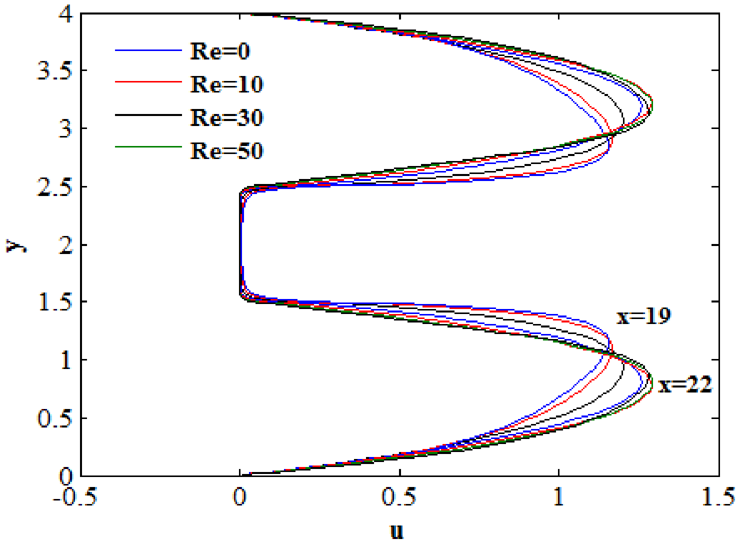

Figure 3.5 Velocity component, u, profiles for different positions at x=19 (near cylinder), x=22 (wake region) for *Re*=0, 10, 30, 50 along the centerline (y=2).

Figure 3.6 shows the effect of *Re* number on the confined flow patterns around the square obstacle in terms of streamline and vorticity profiles for *Re*=0, 10, 20, 30, 50. The streamline profiles are shown in the upper half of figures, while the vorticity contours are shown in the lower half. No separation occurs from the surface of the cylinder for *Re*=0 due to creeping nature of the flow. However, flow separation was observed at higher *Re* numbers. As *Re* number increases from *Re*=10 to 50, the flow separation gets more pronounced at the vicinity of the obstacle edges. A closed recirculation region consisting of two symmetric vortices develop in the wake region as shown in Figures 3.6c-e.

Dimensionless recirculation length that is also known as the wake region is defined by Breuer et al. [7] as the distance between the obstacle surface and reattachment point of streamlines (i.e., ψ=0 on the axis of symmetry at y=2) to form the encapsulated region behind the obstacle. As Reynolds increased, this length gets larger.

Vorticity profiles can also be used to investigate the behavior of the fluid flow around the obstacle. Stream function, ψ, and vorticity, ω, are obtained through the solution of the following Equations 3.1 and 3.2.

$$\nabla^2\psi = -\omega \tag{3.1}$$

$$\omega = -\frac{\partial u}{\partial y} + \frac{\partial v}{\partial x} \tag{3.2}$$

Vorticity are also helpful in locating separation points. These contours seem to transit from being symmetrical at *Re*=0 to being asymmetrical at higher *Re* numbers as in Figures 3.6. The vorticity also is seen to persist for a very long way downstream of tile cylinder at higher *Re* numbers. The magnitude of the corner vorticity increases with *Re* number at the upstream of the flow for *Re*=20, 30, 50.

Values of the stream function and vorticity and their primary axial wake locations at x=22, 23, 24 and vertical locations at y=2.5, 3 are tabulated in Table 3.1. These points are also considered as near wake (x=22, y=2.5) and far wake region (x=24, y=3) of the obstacle. In the near wake region, vorticity values are larger compared to far wake region due to highly intense velocity gradients in that region. Gupta et al. [34] and Dhiman et al. [11] have also reported similar vorticity distribution for Newtonian flow around the square cylinder in the range conditions $1 \leq Re \leq 45$. For small *Re* flows, vicinitiy vorticities get higher, since v-velocity component gradient is also higher at small *Re* (see Figure 3.4).

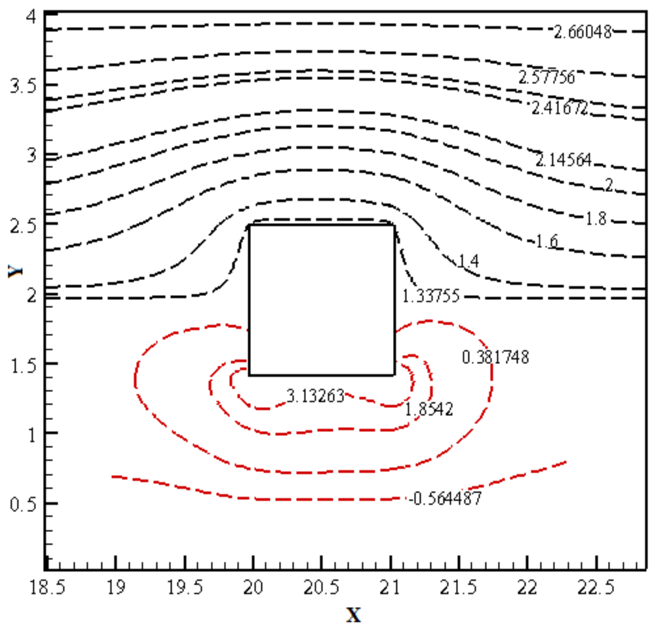

(a)

Figure 3.6 Streamline and vorticity profiles (upper and lower parts gives the results for streamline and vorticity, respectively) for a for different Reynolds numbers (a) *Re*=0 (b) *Re*=10 (c) *Re*=20 (d) *Re*=30 (e) *Re*=50.

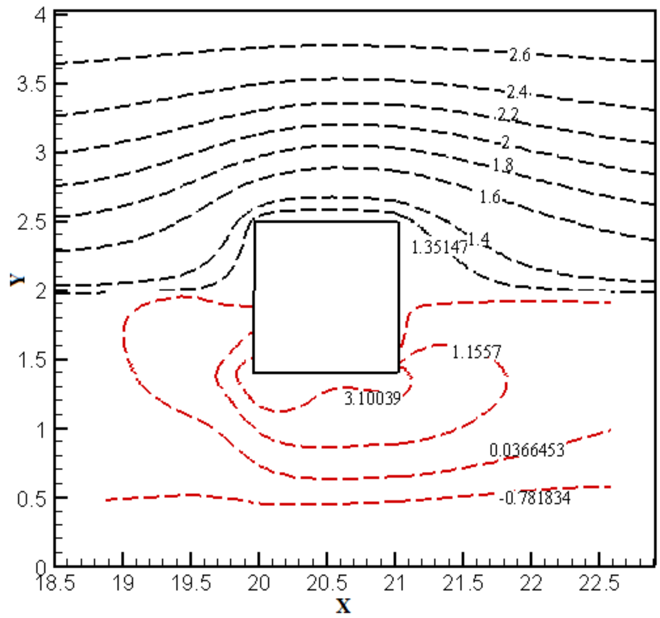

(b)

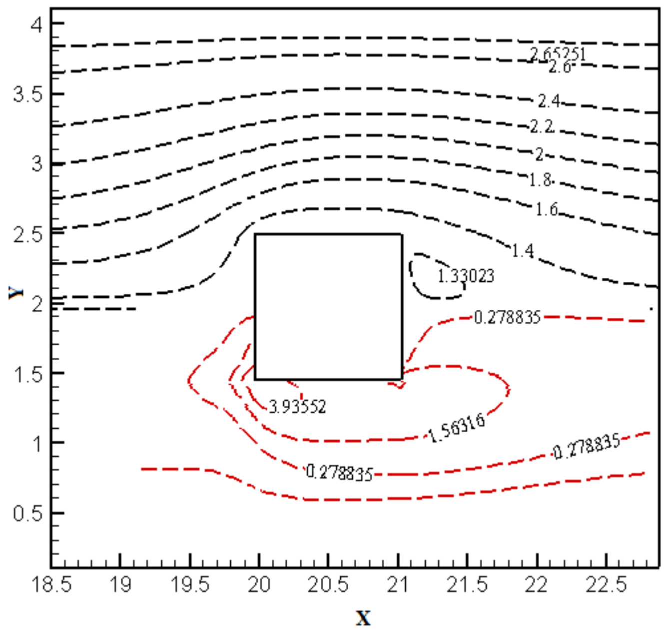

(c)

Figure 3.6 Streamline and vorticity profiles (upper and lower parts gives the results for streamline and vorticity, respectively) for a for different Reynolds numbers (a) *Re*=0 (b) *Re*=10 (c) *Re*=20 (d) *Re*=30 (e) *Re*=50 (continued).

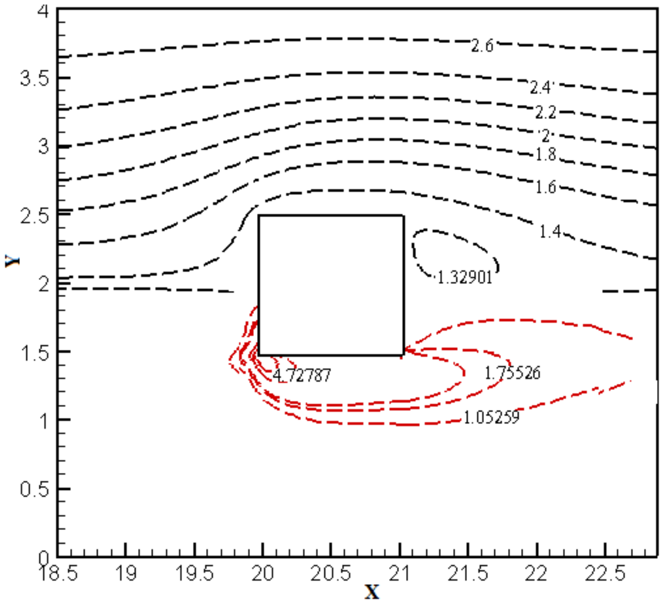

(d)

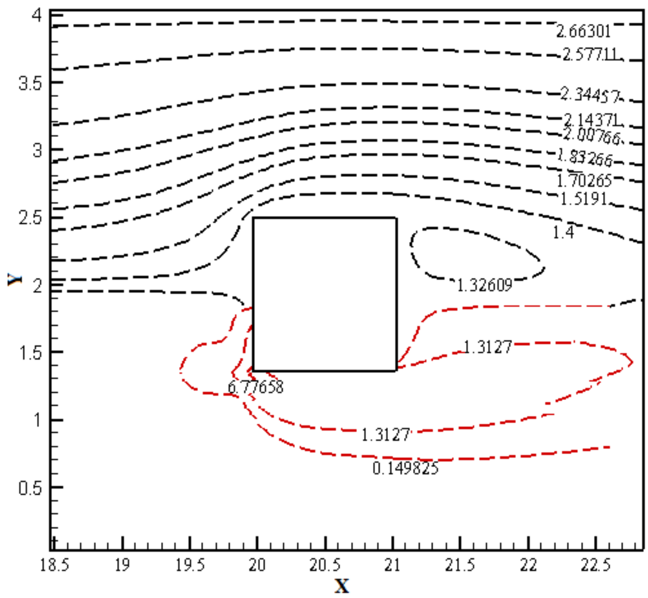

(e)

Figure 3.6 Streamline and vorticity profiles (upper and lower parts gives the results for streamline and vorticity, respectively) for a for different Reynolds numbers (a) *Re*=0 (b) *Re*=10 (c) *Re*=20 (d) *Re*=30 (e) *Re*=50 (continued).

Table 3.1 Intensities of the primary eddies and vorticity and their locations in the wake region

Re	***ω***	***ψ***	**x**	**y**
0	-1.8930	1.6636	22	3
0	-1.7269	1.6874	23	3
0	-1.4988	1.7168	24	3
0	-4.3842	1.3526	22	2.5
0	-3.0359	1.3762	23	2.5
0	-2.2318	1.4061	24	2.5
10	-1.9136	1.6246	22	3
10	-1.8391	1.6379	23	3
10	-1.7330	1.6548	24	3
10	-2.9159	1.3424	22	2.5
10	-2.3837	1.3531	23	2.5
10	-2.0887	1.3668	24	2.5
20	-1.9703	1.6089	22	3
20	-1.9091	1.6177	23	3
20	-1.8289	1.6291	24	3
20	-2.6605	1.3589	22	2.5
20	-2.2703	1.3442	23	2.5
20	-2.0476	1.3316	24	2.5
30	-2.0254	1.6021	22	3
30	-1.9662	1.6084	23	3
30	-1.8932	1.6167	24	3
30	-2.3695	1.3365	22	2.5
30	-2.1791	1.3397	23	2.5
30	-2.0538	1.3438	24	2.5
50	-2.0765	1.5949	22	3
50	-1.9779	1.5985	23	3
50	-1.9034	1.6035	24	3
50	-2.1139	1.3343	22	2.5
50	-2.0603	1.3351	23	2.5
50	-1.9946	1.3359	24	2.5

For the same region, say x=22 and y=2.5, streamline magnitudes are similar for different *Re* number. However, vorticity intensity shows a decreasing trend as compared to upstream locations. It can be resulted from that v velocity component changing with respect to x creates smaller gradients in the wake region for high *Re* numbers as shown in Figure 3.4. On the other hand, u-velocity component changing with y axis has more symmetrical distribution due to the imposed parabolic velocity profile at the inlet of the channel. It is also nearly independent of *Re* numbers (see Figure 3.5).

3.3. Drag coefficient around the obstacle

One of the most important characteristic quantities of the flow around a cylinder is the drag coefficient *Cd*. In the region of small Reynolds numbers the drag coefficient varies strongly with *Re*. The contributions of the viscous and pressure forces to the total drag are of the same order of magnitude as in Table 3.2. A comparison of the computed results of different studies is shown in Table 3.3 at $0 \leq Re \leq 50$. A Cartesian non-uniformly structured mesh with 372x162 grid system is used to represent the flow system having a blockage ratio of *B*=1/8 and *B*=1/4.

Drag coefficient is obtained by integrating the shear stress (viscous) and pressure contributions over the square cylinder surfaces denoted as *f* front, *r* rear, *t* top, and *b* bottom similar to the methodology reported by Dhiman et al. [11]. The relation for *Cd* can be written as:

$$Cd = \frac{2}{\mathrm{Re}} \int_0^1 [((\tau_{xy,t}(x) + \tau_{xy,b}(x))dx] + 2\int_0^1 [(P_r(y) - P_f(y))dy] \tag{3.3}$$

Table 3.2 Viscous and pressure effects of *Cd* in steady flow regime for various *Re* numbers

Re	**Viscous Effect Contribution to *Cd***	**Pressure Effect Contribution to *Cd***	***Cd***
1	17.711	18.567	72.557
5	5.531	6.535	15.282
10	3.263	3.737	8.127
20	1.821	2.261	4.702
30	1.234	1.736	3.555
50	0.791	1.288	2.608

Viscous and pressure contributions of the total drag are listed in Table 3.2. The decreasing trend of *Cd* with increasing *Re* is captured. The impact of *Re* on *Cd* becomes more pronounced at low *Re* region. At very low *Re* region ($Re<1$) that strong impact can be deduced through the Stokes drag coefficient as $Cd=24/Re$. The drag results are also listed in Table 3.3 along with the available values in literature. No data is found in the literature for B=1/4 for the Newtonian case. Therefore, comparison was only done for B=1/8. When B=1/8, the results of this study and those earlier studies compare well with each other. Therefore the methodology followed in this study seems to be accurate to simulate the flow for the Newtonian case.

Another interesting result is associated with the effect of the blockage ratio on the *Cd*. Due to the Newtonian nature of the flow, the drag originates from the form drag acting on the front and rear surfaces and shear drag on the top and bottom surfaces. When flow gets more restricted due to presence of a larger obstacle, i.e. larger *B*, higher velocities between the channel and the obstacle give rise to higher shear stress and form drag effects, i.e. larger *Cd* values as shown in Table 3.3.

Table 3.3 Comparison of *Cd* in steady flow regime with literature for various *Re* numbers

Re	***B*=1/4 (present)**	***B*=1/8 (present)**	***B*=1/8 [11]**	***B*=1/8 [34]**	***B*=1/8 [7]**
0	$7.114\text{x}10^5$	$3.115\text{x}10^5$	-	-	-
1	72.557	23.687	-	-	24.612
5	15.282	5.761	5.849	5.549	5.814
10	8.127	3.699	3.663	3.511	3.872
20	4.702	2.462	2.442	2.448	2.578
30	3.556	2.214	-	-	2.278
40	3.236	1.826	1.852	1.864	1.925
50	2.608	1.793	1.751	1.762	1.854

3.4. Visualization of Flow Field

PIV is a non-intrusive laser optical measurement technique for analyzing laminar and turbulence flow, microfluidic flow processes. Standard PIV measures two velocity components in a plane using a single camera. The principle behind PIV is to derive velocity vectors from sub-sections of the target area of the particle-seeded flow by measuring the movements of particles between two light pulses:

$$v = \frac{\Delta x}{\Delta t}$$

In a standard, two-dimensional system, illumination of the flow field is provided by a narrow sheet of light. The flow is seeded particles, and the images of these particles are recorded by a camera placed at 90^0 to the light sheet as in Figure 3.7.

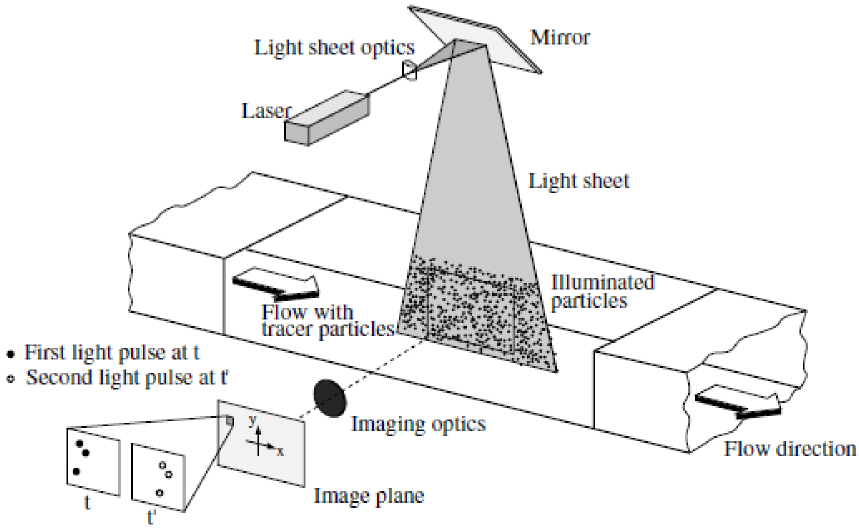

Figure 3.7 Schematic set-up of particle image velocimetry [36]

Low Reynolds number PIV studies in the literatüre are scarce due to difficulties encountered to obtain a high quality velocity measurements. On the contrary, reports on numerical investigation at low Reynolds number flows are more readily available as mentioned in section 3.1.

In this section, we qualitatively describe the sequence of changes that occurs to the flow pattern around a cylinder with blockage ratio of 1/4 with Reynolds number within the range of 1 and 100 using PIV.

A large number of studies have been performed to investigate the Newtonian flow over single square cylinder to analyze turbulence flow characteristics. Okajima [37] carried out an experimental study of flow past a square cylinder as well as rectangular cylinder for 70<*Re*<20,000 to determine the vortex shedding frequencies for unsteady flow. Okajima found that the highest Strouhal number (*St*) was observed when $10^4<Re<2\mathrm{x}10^4$. Oudheusden et al. [38] studied the vortex shedding and drag force characteristics in the near wake of a square cylinder placed at various angles (Θ) to the mean flow for Reynolds numbers of 4,000, 10,000, and 20,000 using PIV. They found that the flow separation occurred at both front corners and the shallow recirculation regions were observed above and below the obstacle while the angle is 0. The separation points move downstream while $\Theta>0$. Furthermore, two other large recirculation regions appeared in the wake behind the body in a similar fashion as that for the circular cylinder. According to Berrone et al [39] as *Re* is increased, the upstream–downstream symmetry of the streamlines disappeared and two eddies appeared behind the cylinder. These eddies get bigger with increasing *Re*, but do not move off downstream: the flow in the wake is still steady. At high *Re*, the flow becomes unsteady due to wake instability mechanisms and the phenomenon of vortex shedding, known also as von Kármán Street [40].

The literature review indicates the importance of turbulence characteristics for bluff bodies at high Reynolds numbers. These are mainly related to the unsteady flow around the obstacle. Current PIV measurements were conducted to investigate the impact of square obstacle inside a channel. Particle image velocimetry (PIV) was used to measure the two-dimensional velocity field to reveal streamlines and vorticity patterns in a qualitatively manner. The changes of flow structure of the system due to effect of *Re* number were compared with computational results obtained at similar conditions.

PIV visualizations were performed at Nanotechnology Engineering Department at Cumhuriyet University, Sivas. The experiments were carried out in a 300 cm long channel plexiglas of ½ in with the inner cross-section of 12x12 cm. The channel and the closed flow loop to circulate clean tap water via a magnetic pump are depicted in Figure 3.8. Square obstacle made of plexiglas was installed in the test section as shown in Figure 3.9. The dimensions of obstacle were 3 cm height, 0.5 cm in thickness, and 12 cm in width to provide a blockage ratio of 1/4. *B* is the ratio of obstacle diameter over channel diameter.

Experiments were done at the Reynolds numbers of 1, 20, 30, 40, 50, 100 where the Reynolds number was defined based on the diameter of the channel and the mean water velocity. To observe two-dimensional flow field of the system, illumination of the flow field was provided by a narrow sheet of light. The flow was seeded by Polyamide particles of size 50 μm and the images of these particles were recorded by a camera placed at 90^0 to the light sheet depicted in Figure 3.10.

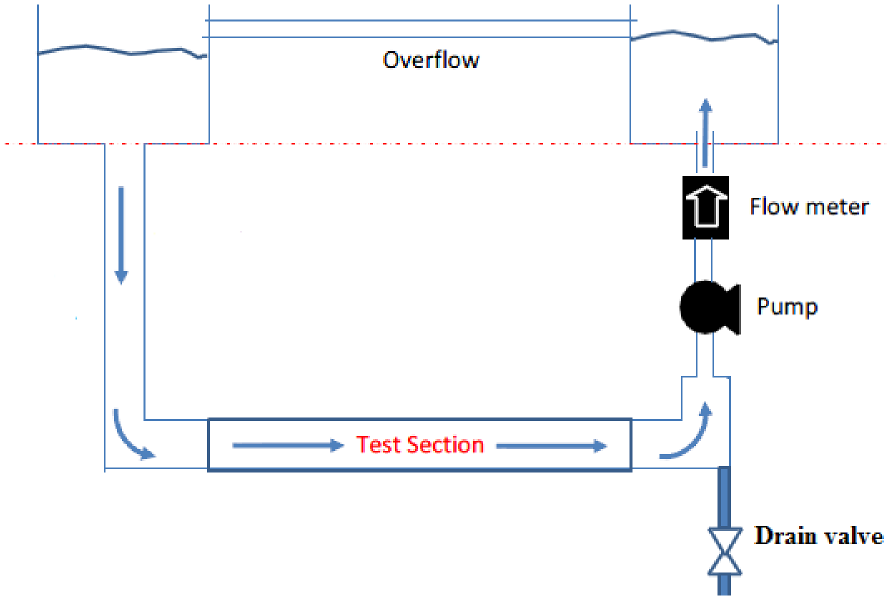

Figure 3.8 Experimental flow loop set-up

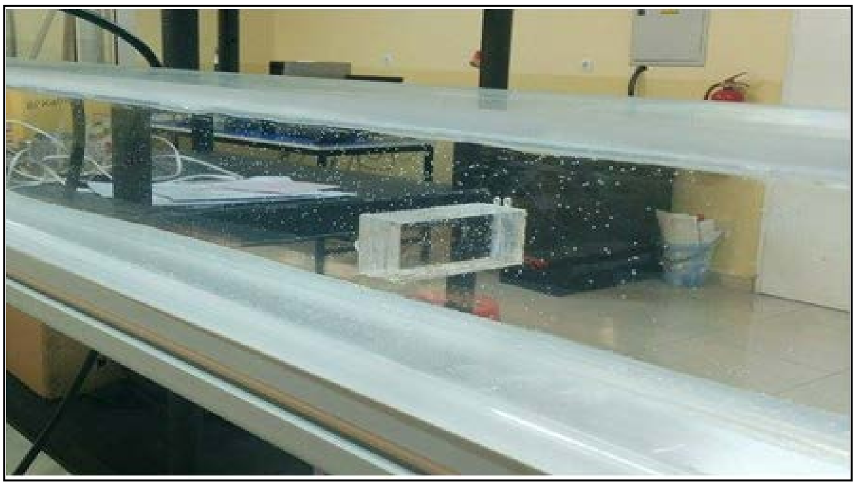

Figure 3.9 Illustration of square obstacle inside experimental set-up

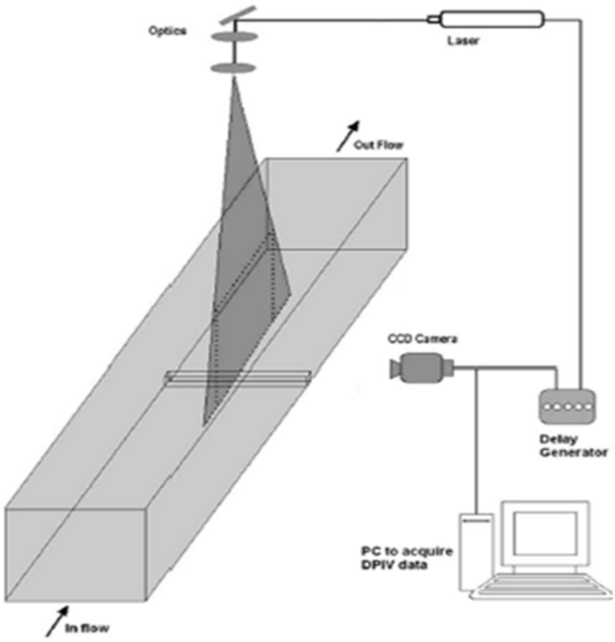

Figure 3.10 Schematic of test section

Solid state Nd: YAG lasers using frequency-doubling crystals to produce light at 532 nm was used as the light source. 256 pair of images were taken by PIV camera as seen in Figure 3.10 and these images yields velocity vectors by cross-correlating the interrogation region in the first 5 image with the corresponding search region in the second image pair [36]. Averages of these images were taken by PIV processor to get flow field.

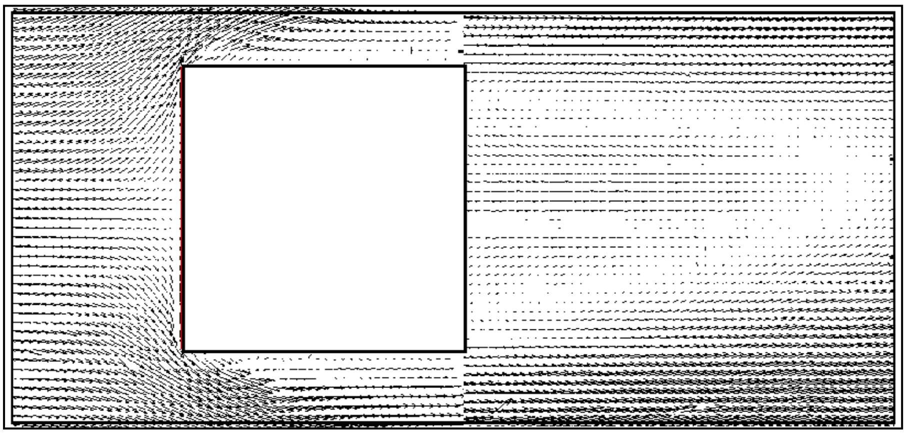

Figure 3.11 Experimental velocity vector field at Re=30

Two dimensional mean velocity vector fields at *Re*=30 is presented in Figure 3.11. The plot represents the typical behavior flow past over an obstacle. The flow shows that the flow is affected by the obstacle mainly in the surrounding region with the flow separation off the top and bottom edges of the obstacle. Figure 3.11 also exhibits strong recirculation region at downstream of the obstacle. Stagnation areas are observed near the obstacle wall.

Vortices induced by the obstacle enhance mixing in the recirculation zone. Subsequent plots in Figures 3.12b and 3.12f give the vortex patterns. These locations cover the spatial extent of the flow within the given field of view from the region immediately downstream of the obstacle including the recirculation zone up to the region where the flow reattaches itself. Comparing the flow patterns for both results, symmetrical vortex region can be identified similar to the numerical results in Figure 3.2. At *Re*=20, small vortexes start to occur near attachment of the wake region as shown in Figure 3.12b. The wake area or recirculation region also increases as the effect of inertial forces increases when *Re* is increased from *Re*=30 to *Re*=100. With an increase in *Re* number, symmetrical vortexes become more dissernable due to the increased accuracy of PIV at higher velocities.

Large part of the flow domain is affected by the obstacle and larger vortex appeared behind the obstacle as shown in Figure 3.12e-f compared to Figure 3.12c-d when the Reynolds number increased.

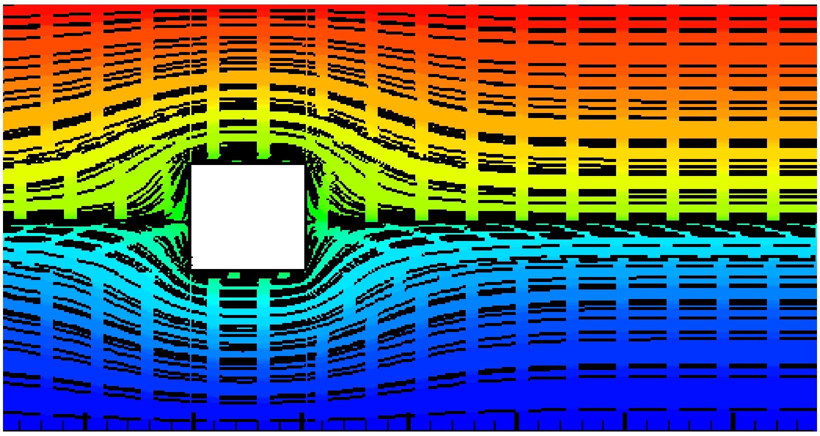

(a)

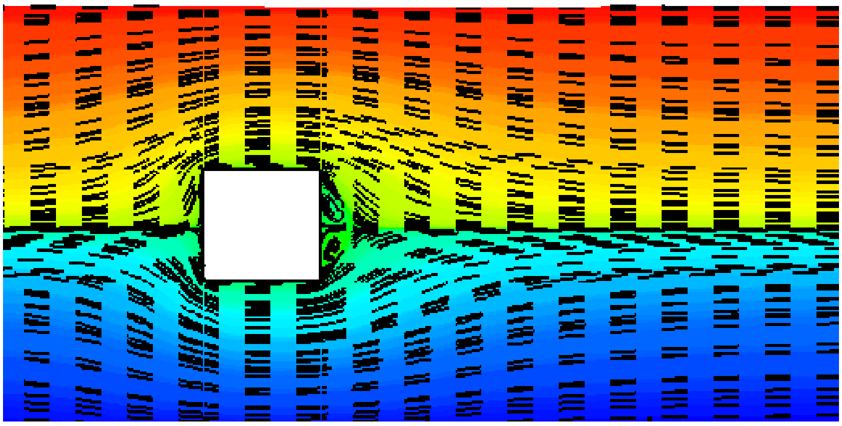

(b)

Figure 3.12 Experimental streamline profiles around the square cylinder for different Reynolds numbers by PIV (a) *Re*=1 (b) *Re*=20 (c) *Re*=30 (d) *Re*=40 (e) *Re*=50 (f) *Re*=100.

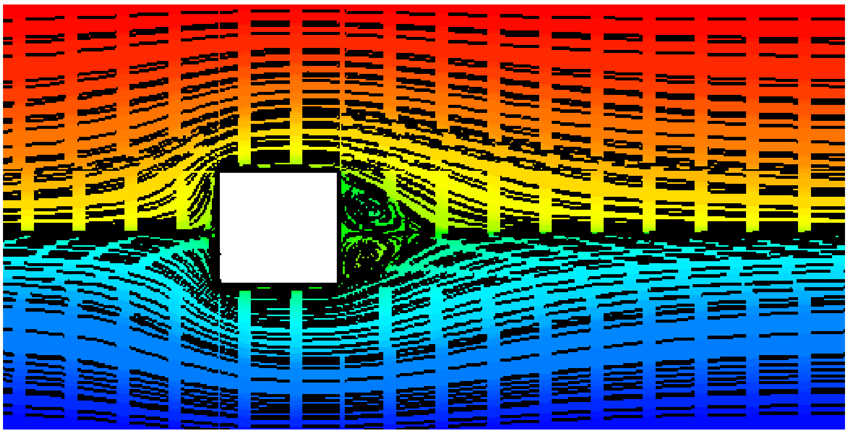

(c)

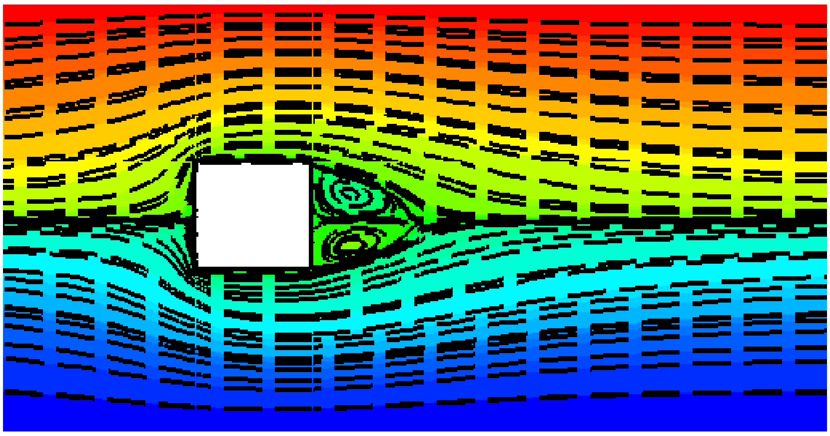

(d)

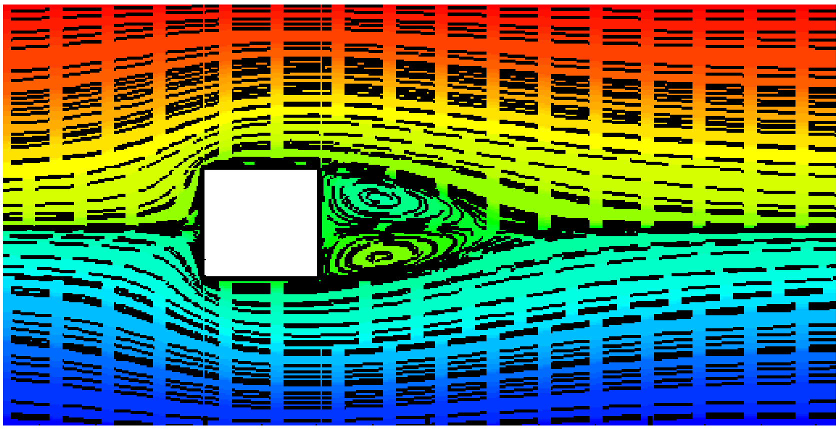

(e)

Figure 3.12 Experimental streamline profiles around the square cylinder for different Reynolds numbers by PIV (a) *Re*=1 (b) *Re*=20 (c) *Re*=30 (d) *Re*=40 (e) *Re*=50 (f) *Re*=100 (continued).

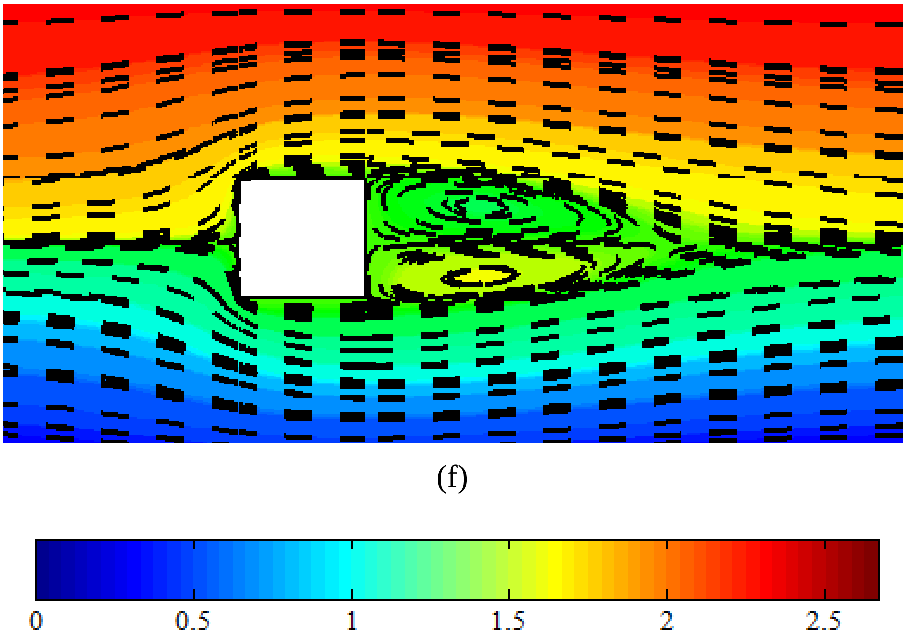

Figure 3.12 Experimental streamline profiles around the square cylinder for different Reynolds numbers by PIV (a) *Re*=1 (b) *Re*=20 (c) *Re*=30 (d) *Re*=40 (e) *Re*=50 (f) *Re*=100 (continued). Contour levels are shown from 0 to 2.5 with the increment of 0.5.

Vorticity field is calculated based on the velocity field shown in Figure 3.12. The mechanism of the vorticity production is dependent on the no-slip boundary condition at the obstacle surface and the surface curvature. Hence, at the edges of the obstacle where boundary conditions of the system changes suddenly, highest intensity of the vorticity is obtained in the normal direction to the flow. But in the region between obstacle and the channel wall there is high shearing of the fluid and the vorcitiy magnitude is lower in this region as shown in Figure 3.13.

In order to study influence of *Re* on the vorticity dynamics of Newtonian flow around the obstacle, contour maps of the vorticity field of flow for different Reynolds numbers are presented in the following plots in Figures 3.13a-f. There are qualitative similarities between numerical and experimental results. For all Reynolds numbers, symmetrical vorticity distribution is attained in Figures 3.13a-d. Vorticity is almost uniform and its intensity remains the same at the corner of the obstacle depicted in Figure 3.13a and 13d.

Increase of flow inertia leads to increase in the intensity of the vorticity contours as shown in Figure 3.13c and 3.13d. Contour layers at the edges of the obstacle are more distinguishable, a behavior similar to the numerical predictions. As Reynolds number increases, vorticity pattern disperses symmetrically in the flow direction as shown in Figure 3.6. Vortex area is also found to be higher as Reynolds number gets larger.

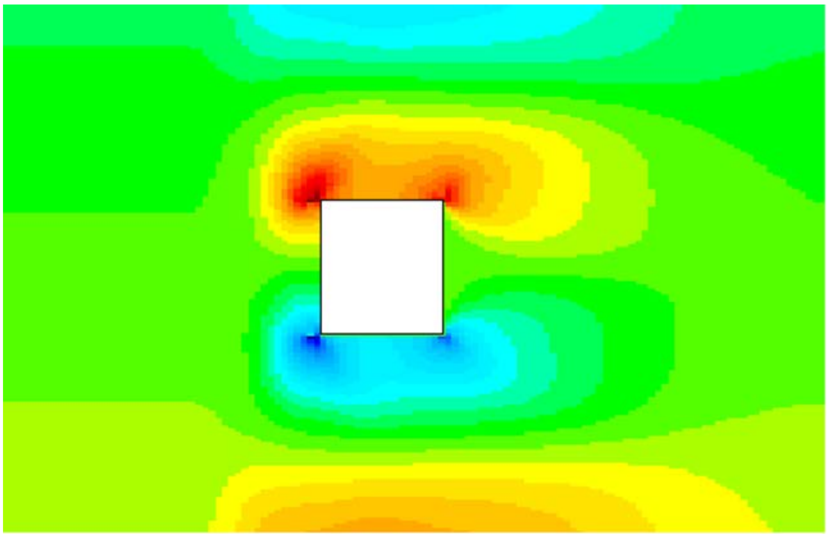

(a)

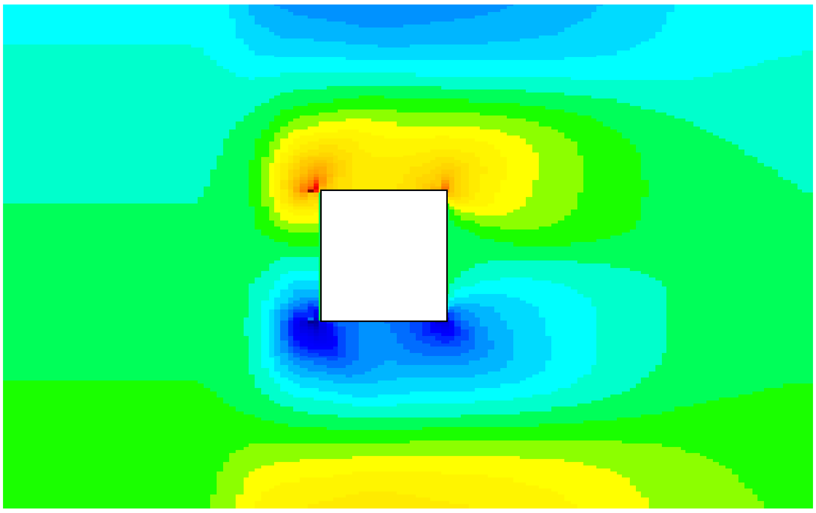

(b)

Figure 3.13 Experimental vorticity profiles around the square cylinder for different Reynolds numbers by PIV (a) *Re*=1 (b) *Re*=10 (c) *Re*=50 (d) *Re*=100.

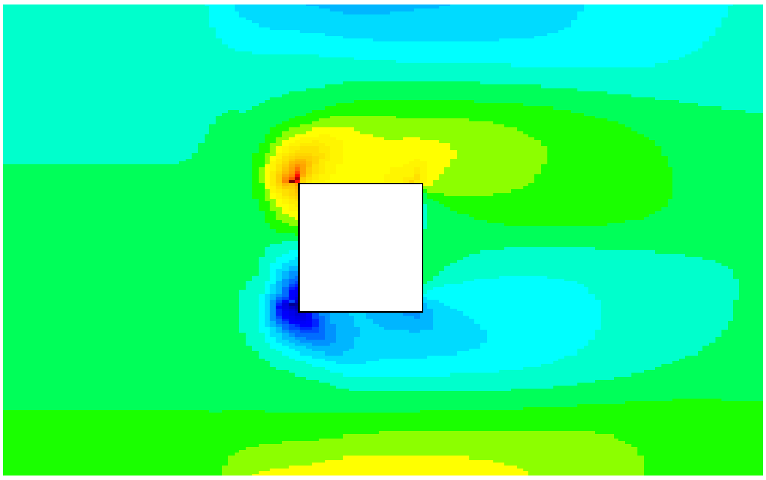

(c)

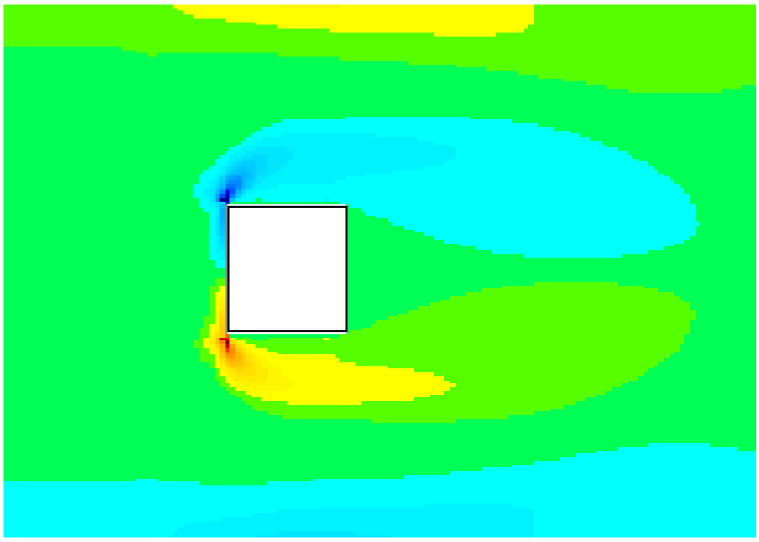

(d)

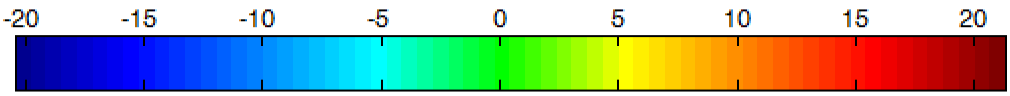

Figure 3.13 Experimental vorticity profiles around the square cylinder for different Reynolds numbers by PIV (a) *Re*=1 (b) *Re*=10 (c) *Re*=50 (d) *Re*=100 (continued). Contour levels are shown from -20 to 20 with increment of 5.

CHAPTER 4

STEADY VISCOELASTIC FLOW AROUND SQUARE OBSTACLE

This study focuses on the implementation of a structured non-uniform finite volume method for the 2-D laminar flow of viscoelastic fluid past a square section of cylinder in a confined channel with a blockage ratio 1/4 for $Re=10^{-4}$, 5, 10 and 20. Oldroyd-B model (constant viscosity with elasticity) and the PTT model (shear-thinning with elasticity) are the constitutive models considered. Finite volume method is used with the staggered grid arrangement. The stress terms in the constitutive equations are approximated by a higher-order and bounded scheme of Convergent and Universally Bounded Interpolation Scheme for the Treatment of Advection (CUBISTA). In this section, effects of the elasticity and inertia on the stress field around the square cylinder and drag coefficient are obtained and discussed in detail.

4.1. Introduction

In the case of non-Newtonian fluid flow around confined obstacles, the literature is dominated by the studies with generalized Newtonian model to capture shear thinning or thickening effects. On the other hand, investigating the effects of viscoelasticity on the hydrodynamics of the flow around the obstacles has potentially crucial implications on many industrial applications. Therefore it is important to study the hydrodynamics of such industrially important flows to reveal both microscopic and macroscopic flow quantities. Hence, the objective of this study is to investigate flow of a viscoelastic fluid, a linear PTT fluid and Oldroyd-B fluid, around a confined square obstacle computationally. Finite volume method is employed to solve coupled equations of continuity, motion and constitutive model along with appropriate boundary conditions. Effects of inertia in terms of *Re*, elasticity in terms of Weissenberg number, *We*, and constitutive equation parameters on the recirculation length, drag and on the flow field in terms of stress and velocity fields are examined and presented in detail.

4.2. Numerical Results and Discussion

A Reynolds number range $10^{-4} \leq Re \leq 20$ was investigated numerically, where *Re* is based on the cylinder diameter b and the maximum flow velocity u_{max} of the parabolic inflow profile (see Figure 2.2) The following section starts with a description of the different flow patterns observed with respect to *Re* and *We* . The subsequent sections present a detailed comparison of the computed results based on velocity, pressure and stress profiles at several positions in the flow field for both of the viscoelastic model. Furthermore, the computations are analyzed and compared in terms of drag coefficient.

4.2.1. Streamlines around the obstacle

We begin presenting the computational results of the flow system by the inertial and elasticity effects on the recirculation patterns behind the obstacle depicted in Figure 4.1. The values of the constitutive model parameters used to obtain these results are ε=0.25 and β=0.2. Dimensionless recirculation length that is also known as the wake region is defined by Breuer et al. [7] as the distance between the obstacle surface and reattachment point of streamlines to form the encapsulated region behind the obstacle. It should be noted that at a given *Re* upper limit of *We* is determined by the stability of the computations. The higher the value of *Re*, the lower *We* that can be attained for stable computations. For example when *Re* is set as 20, the maximum value of the attainable *We* is 3 in this study. Figures 4.1 illustrate that increasing fluid elasticity or inertia leads to larger recirculation lengths and eventually formation of symmetric vortexes as depicted in Figure 4.1.c similar to the results reported by Breuer et.al. [7]. Larger recirculation lengths and observed vortexes can be attributed to Hoop stresses getting stronger at increased fluid inertia and elasticity. Hu and Joseph [41] used UCM model, which has the same behavior as Oldroyd-B, and reported similar trend in the flow around circular cylinder. They also observed larger vortices with increasing elasticity.

The flow quantities such as stress and velocity fields are determined through the complex interactions between inertia, elasticity and shear thinning that gets stronger at elevated *Re* and *We*. In Figure 4.2, viscoelastic fluid effects on the recirculation length (*Lr*) are compared at different *Re*. Oldroyd-B fluid with constant viscosity flow has larger wake region size or recirculation length depicted in Table 4.1. P.Y.Huang and J.Feng [42] obtained the same wake lengths for Oldroyd-B flow around circular cylinder at *Re*=10 when *We* is increased zero to one. Also, *Lr* is increased with *Re* numbers as in Newtonian flow.

Viscoelastic wake behind square obstacle is longer than the Newtonian wake (*We*=0). Because, the wake phenomena has strong dependence on the structure of the flow and on the presence of vortices in the region of highest stress that resides downstream of the rear stagnation point of obstacle surface. Therefore, lacking shear thinning property, Oldroyd-B fluid leads to higher stresses and larger wake field around the obstacle compared to PTT and Newtonian flows. Oldroyd-B flow vortex centers also shift upward and downward direction with respect to PTT fluid due to expanding wake region in Figure 4.2b and 4.2c. This can be clearly seen in Table 4.2. The vortex pair size increases in wake region as *Re* number increases as in Figure 4.2c, when vortex intensities increase for both model listed in Table 4.2.

However, at *Re*=10, the magnitude of vorticity becomes lower. This behavior is different from Newtonian case (see Table 3.1). For low *Re* number, inertial force gets lower and impact of the elasticity on the flow is comparatively smaller than at high *Re* number. So, at *Re*=20, the elasticity of polymer molecule is higher for Oldroyd-B than PTT flow in Figure 4.2c. So, vortex intensity values in wake region ($1.3079<\psi<1.3179$) gets higher at x locations away from the obstacle at a constant y=2.2006 for Oldroyd-B flow at *Re*=20 as depicted in Table 4.2. Also, this vortex enhancement may be attributed to large and constant elongational viscosity of

Oldroyd-B flow. Because, large elongational viscosity delays the acceleration of the fluid which results in the increase of vortex size (see Figure 4.2c).

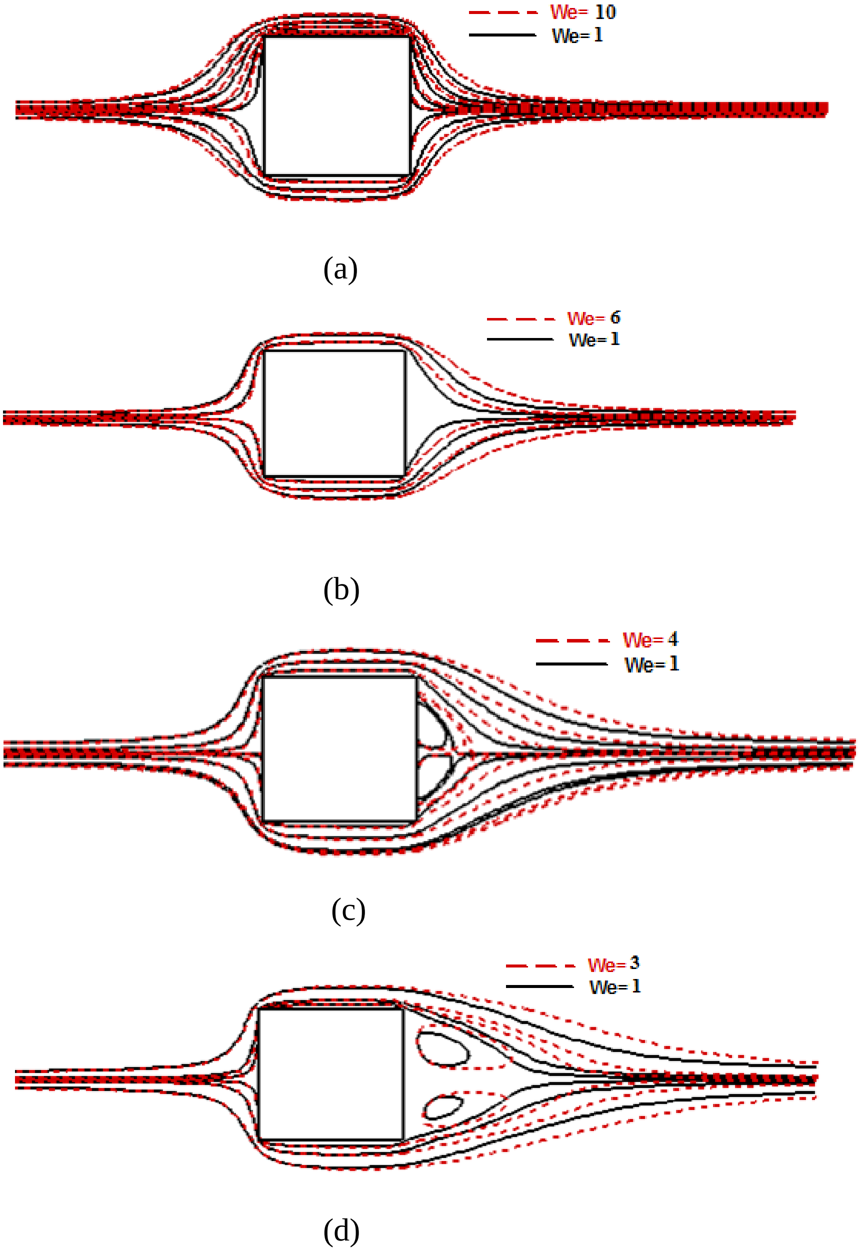

Figure 4.1 Effect of *We* on the recirculation length for PTT fluid at a) *Re*=0 b) *Re*=5 c) *Re*=10 d) *Re*=20

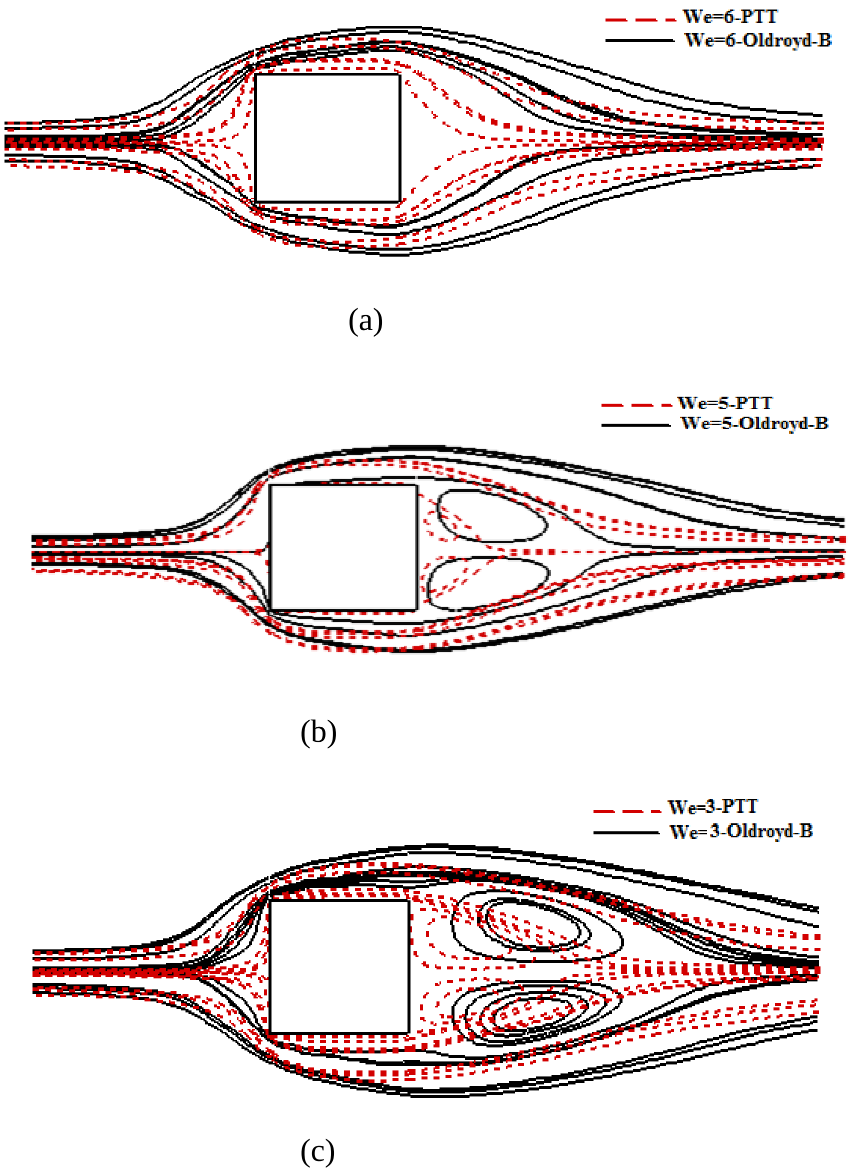

Figure 4.2 Viscoelastic fluid effect on the recirculation length for a) Re=5 b) Re=10 c) Re=20

Table 4.1 Variation of recirculation length (*Lr*) with Reynolds number (*Re*) for different *We* numbers

Re	***We***	***Lr* of PTT at (ψ=0)**	***Lr* of Oldroyd-B at (ψ=0)**
5	0	20.2132	20.2132
	1	21.6133	22.8912
	2	21.9957	23.0755
	5	23.4713	25.1997
	6	23.8912	25.3664
10	0	21.0341	21.0341
	1	24.7001	25.1285
	2	25.1213	26.4356
	3	25.3634	27.3259
	4	26.1784	27.8712
	5	26.2467	28.0125
20	0	22.3452	22.3452
	1	25.7823	26.5648
	2	26.1239	27.1547
	3	26.8745	28.7645

Table 4.2 Intensities of the primary eddies and vorticity and their locations in the wake region

PTT					
We	***Re***	***ω***	***ψ***	**x**	**y**
5	10	-0.1275	1.3314	21.2222	2.1487
5	10	-0.1462	1.3315	21.2502	2.1487
5	10	-0.1855	1.3317	21.3040	2.1487
5	10	-0.2073	1.3320	21.3405	2.1487
5	10	-0.2284	1.3324	21.3501	2.1487
5	10	-0.2504	1.3329	21.4063	2.1487
3	20	-0.2354	1.3263	21.5527	2.1487
3	20	-0.2620	1.3267	21.6340	2.1487
3	20	-0.2891	1.3276	21.7213	2.1487
3	20	-0.3024	1.3282	21.7673	2.1487
3	20	-0.3154	1.3291	21.8149	2.1487
3	20	-0.3495	1.3322	21.9683	2.1487
Oldroyd					
We	***Re***	***ω***	***ψ***	**x**	**Y**
5	10	-0.1281	1.3051	21.5527	2.2006
5	10	-0.1591	1.3068	21.6340	2.2006
5	10	-0.1963	1.3076	21.7212	2.2006
5	10	-0.2172	1.3085	21.7673	2.2006
5	10	-0.2402	1.3104	21.8149	2.2006
5	10	-0.3305	1.3123	21.9683	2.2006
3	20	-0.3884	1.3073	22.2625	2.2006
3	20	-0.3918	1.3086	22.3278	2.2006
3	20	-0.4036	1.3112	22.3954	2.2006
3	20	-0.4095	1.3117	22.4654	2.2006
3	20	-0.4145	1.3157	22.6128	2.2006
3	20	-0.4176	1.3179	22.6905	2.2006

4.2.2. Mesh Tests

Cartesian non-uniform structured mesh is used to represent the flow system having a blockage ratio of B=1/4. Section of the mesh around the axial location of the obstacle is depicted in Figure 4.3 and 4.4. Owing to the specific geometry in the present study, only cartesian grids are applied. Minimum size of the mesh is employed at the vicinity of the obstacle with $\Delta x= 0.02$ and $\Delta y= 0.01$.

Grid points can be clustered in regions of large gradients in the vicinity of the obstacle and coarser grids can be used in regions of minor interest. Only y-dimension grid size is changed due to nature of parabolic velocity profile of the flow. Total numbers of the cells are 372x81 and 372x162 in Figures 4.3 and 4.4 respectively. The FVM allows the application of non-equidistant grids.

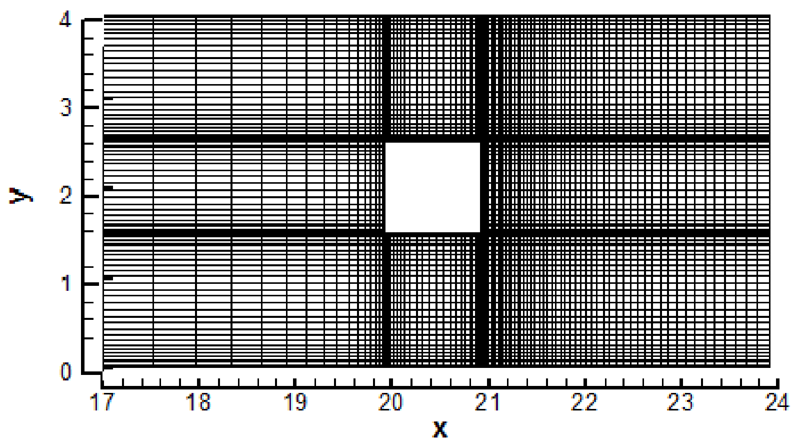

Figure 4.3 Non-uniform meshes around the obstacle with 372x81 cells

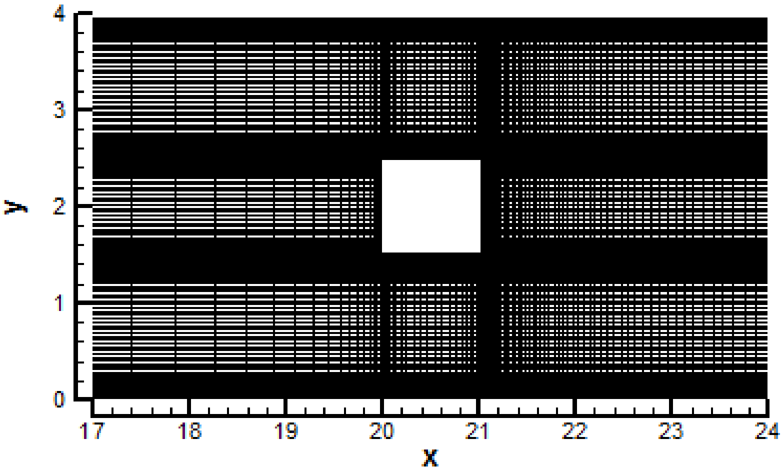

Figure 4.4 Non-uniform meshes around the obstacle with 372x162 cells

The impact of the mesh refinement on the magnitudes of the vorticity, normal stress and shear stress component at the primary vortex center is examined for each of the used constitutive model through the mesh structures tabulated in Table 4.3 at *Re*=10. With shrinking length scales in the velocity gradients, larger stress values can be expected in the computations obtained by the integration of the velocities for both model at 372x162 meshes. The impact of mesh size on computational results was considered negligibly small for the dense mesh of 372x162. The presented results were obtained by using 372x162 meshes.

Table 4.3 Effect of mesh refinement on vortex intensities, normal stress components of $\tau_{xx,}$ shear stress components of τ_{xy} at the center of primary vortex at *Re*=10 for PTT and Oldroyd-B fluid

	PTT	
We	***ω (372x81)***	***ω (372x162)***
1	-0.2315	-0.2325
5	-0.1275	-0.1282
We	***τ_{xx} (372x81)***	***τ_{xx}(372x162)***
1	0.1713	0.1753
5	0.0356	0.0361
We	***τ_{xy} (372x81)***	***τ_{xy}(372x162)***
1	-0.04683	-0.04772
5	-0.00912	-0.00924
	Oldroyd-B	
We	***ω (372x81)***	***ω (372x162)***
1	-0.1467	-0.1469
5	-0.4801	-0.4821
We	***τ_{xx} (372x81)***	***τ_{xx}(372x162)***
1	0.0594	0.0598
5	0.3823	0.3836
We	***τ_{xy} (372x81)***	***τ_{xy}(372x162)***
1	-0.0151	-0.0159
5	-0.1238	-0.1245

4.2.3. Velocity and Pressure profiles around the obstacle

Figures 4.5 and 4.6 present velocity distribution of component, u and v, at several positions of the flow field for *Re*=0 and *Re*=20 with different *We* numbers along the center line. Velocity profile near cylinder and in the wake region differs more than Newtonian flow case (see Figure 3.4). At x=19 that is the position prior to the cylinder region, the velocity profiles differ from Poiseuille flow. Streamwise velocity, u, has a local minimum points for each *We* numbers. As the *We* number increases, the local minimum velocity decreases as in Figure 4.5 a, c and d at x=19 for both model. On the other hand, at x=22, local maximum velocity increases at elevated *We*.

In the wake region, x=22, u- velocity profiles become highly modified due to the presence of the obstacle. For both model, flow is nearly independent of *We* number at *Re*=20. These results associated with the velocity field can be attributed to shear thinning property of the fluid that becomes more pronounced at elevated *We* values as shown in Figure 4.5a and b for PTT fluid. On the other hand, u velocity for Oldroyd-B has more deformation due to more elastic behavior and the maximum velocity region shifts (see Figure 4.5c and d). In other words, the elasticity changes dramatically the flow at high *We* numbers. The streamwise velocity at high *We* is slower to recover the undisturbed bulk velocity than low *We* flows especially in the wake region as seen in Figures 4.5a-d.

Figure 4.5e and 4.5f show influence of *We* on profiles of the streamwise velocity component, u, along the centerline (y=2) for PTT fluid. We also compare these results with the corresponding numerically computed velocity profiles for a Newtonian fluid under at *Re*=5 and *Re*=20 (see Figure 4.5e-h). Upstream of the cylinder the flow is essentially independent of *We* along the cylinder, in agreement with Figure 4.5e, f, h.

For PTT flow, required length to achieve the fully developed velocity, ($\partial u/\partial x=0$), is nearly the same for all *We* numbers plotted in Figure 4.5e and 4.5f while fully developed velocity in magnitude is lower than Newtonian flow. Axial velocity is shifted downstream and thus decreases relative to Newtonian flow with increasing *We*.

For Oldroyd-B flow in Figure 4.5g, a slight velocity overshoot is observed far from the cylinder, at high *We* at which elastic effects are dominant. Elasticity of the fluid leads to increase in the required length for velocity recovery. When inertia increases, shear and viscous effects also play important role in the flow and recovery of the velocity occurs at even larger lengths as shown in Figure 4.5h.

Figure 4.6 shows cross-stream velocity, v, along the center line at y=2. This component of the velocity is smaller than u. Therefore it becomes challenging to predict it accurately compared to Newtonian flow case (see Figure 3.3).

For the flow of PTT, more symmetric velocity profiles around obstacle are observed as shown in Figure 4.6a and 4.6b. With low elasticity, higher vertical velocity, v, is obtained. As *We* number increases, the maximum value of vertical velocity component decreases in magnitude. However, at *Re*=0 and *Re*=20, Oldroyd-B flow has overshoot and undershoot peaks especially for *We*=3 in Figure 4.6c and 4.6d. Absolute magnitude of vertical velocity component range is also higher than PTT. The overshoot and undershoot at the centerlines can be attributed to the purely elastic and constant viscosity behaviors of Oldroyd-B flows. They get more pronounced as *We* increases. In the wake region, vertical velocity approaches to zero at *Re*=0 as in Figure 4.6c. Also, some oscillations appear at high *Re* in Figure 4.6d.

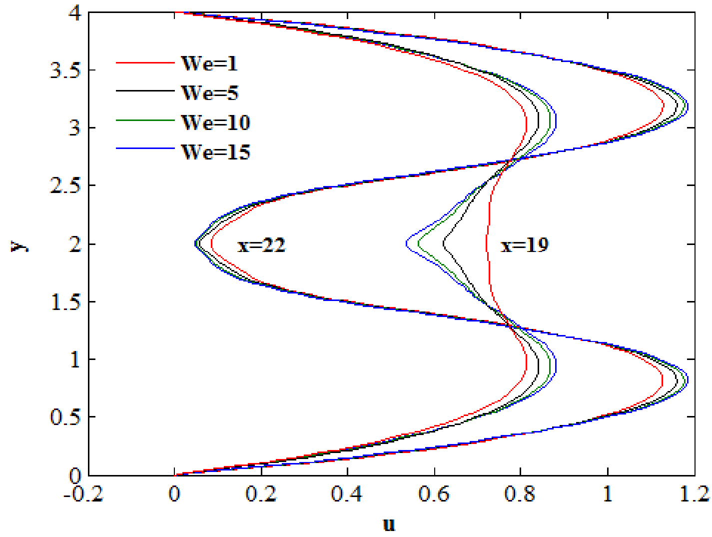

(a)Re=0

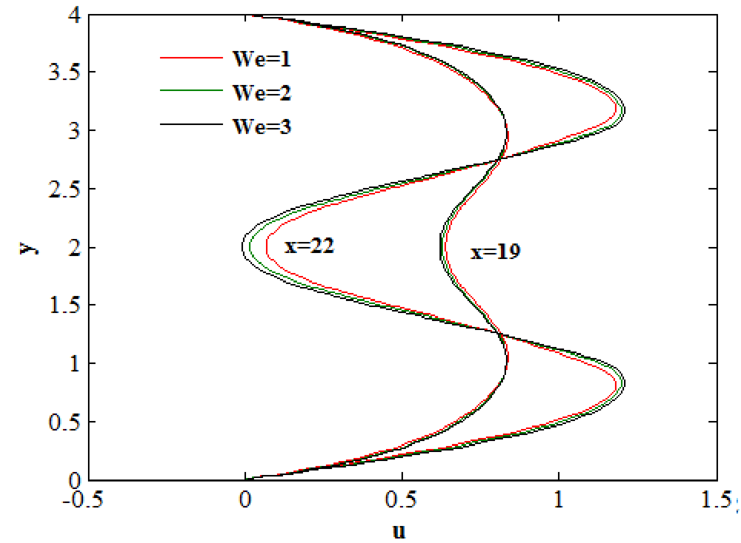

(b) Re=20

Figure 4.5 Velocity component, u, profiles for different positions at x=19 (before cylinder), x=22 (wake region) (a) and (b) for PTT fluid (c) and (d) for Oldroyd-B fluid, at y=2 (centerline) (e) and (f) for PTT fluid (g) and (h) for Oldroyd-B fluid.

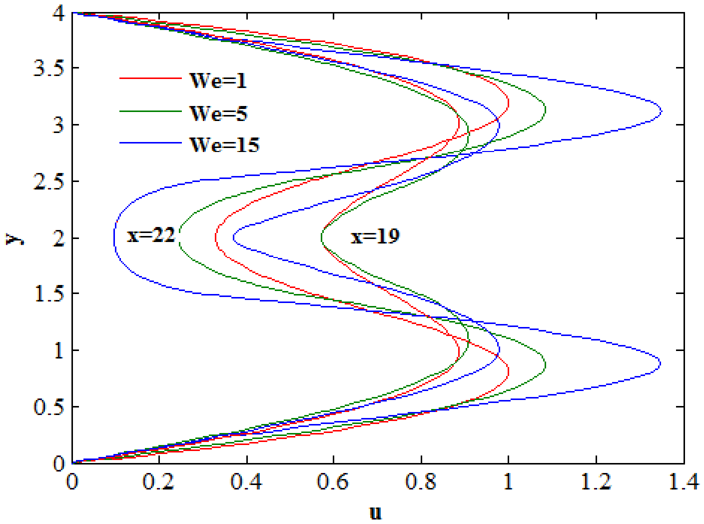

(c)Re=0

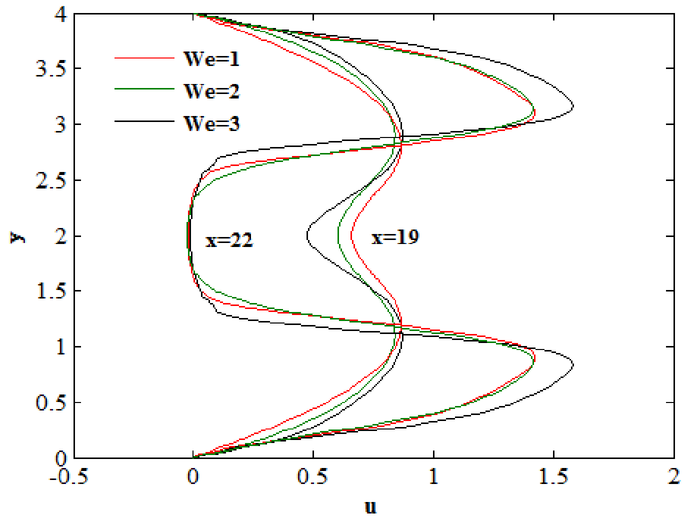

(d) Re=20

Figure 4.5 Velocity component, u, profiles for different positions at x=19 (before cylinder), x=22 (wake region) (a) and (b) for PTT fluid (c) and (d) for Oldroyd-B fluid, at y=2 (centerline) (e) and (f) for PTT fluid (g) and (h) for Oldroyd-B fluid.

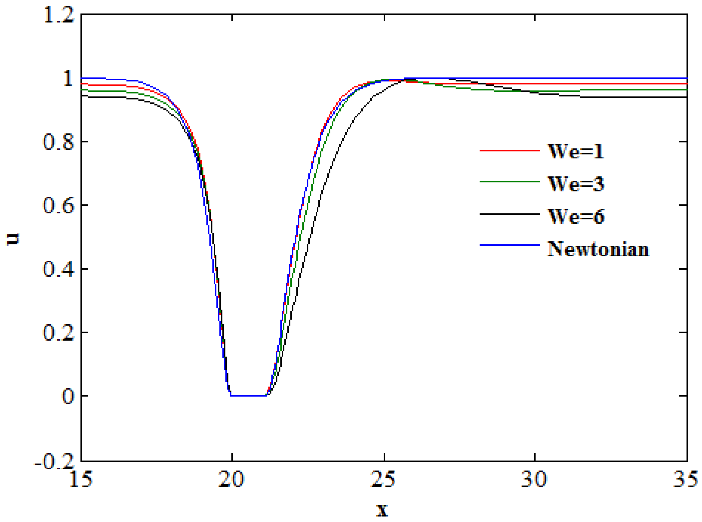

(e) Re=5

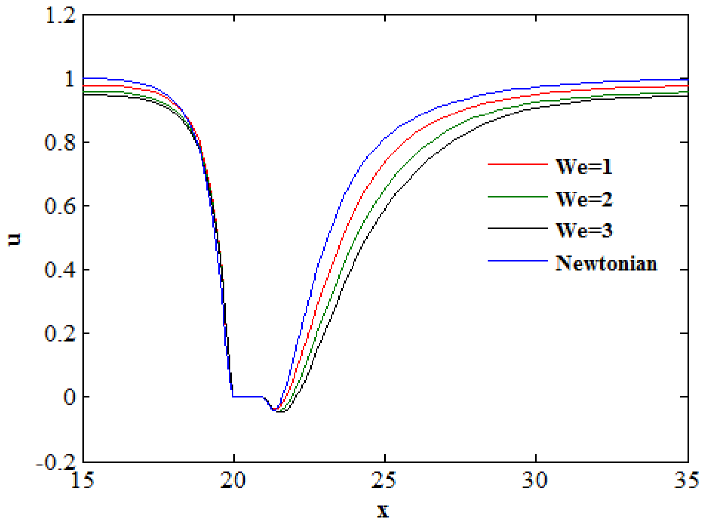

(f) Re=20

Figure 4.5 Velocity component, u, profiles for different positions at x=19 (before cylinder), x=22 (wake region) (a) and (b) for PTT fluid (c) and (d) for Oldroyd-B fluid, at y=2 (centerline) (e) and (f) for PTT fluid (g) and (h) for Oldroyd-B fluid (continued).

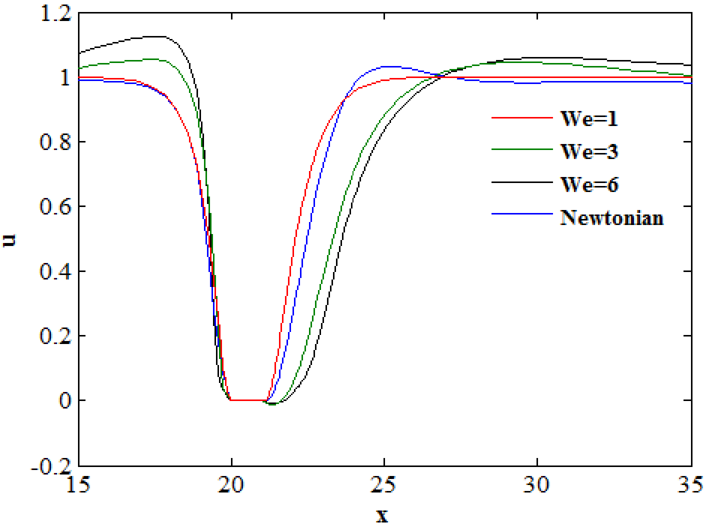

(g) Re=5

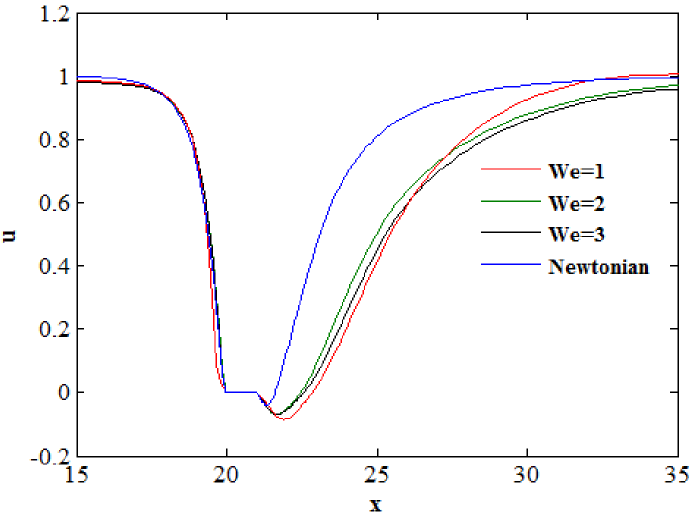

(h) Re=20

Figure 4.5 Velocity component, u, profiles for different positions at x=19 (before cylinder), x=22 (wake region) (a) and (b) for PTT fluid (c) and (d) for Oldroyd-B fluid, at y=2 (centerline) (e) and (f) for PTT fluid (g) and (h) for Oldroyd-B fluid (continued).

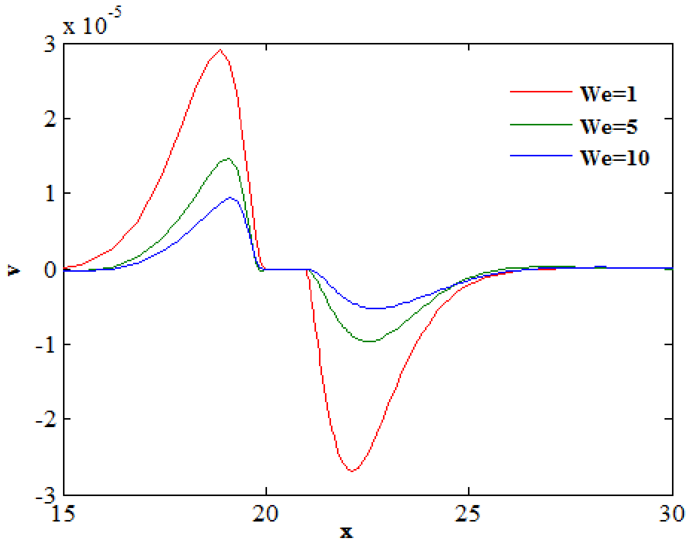

(a)Re=0

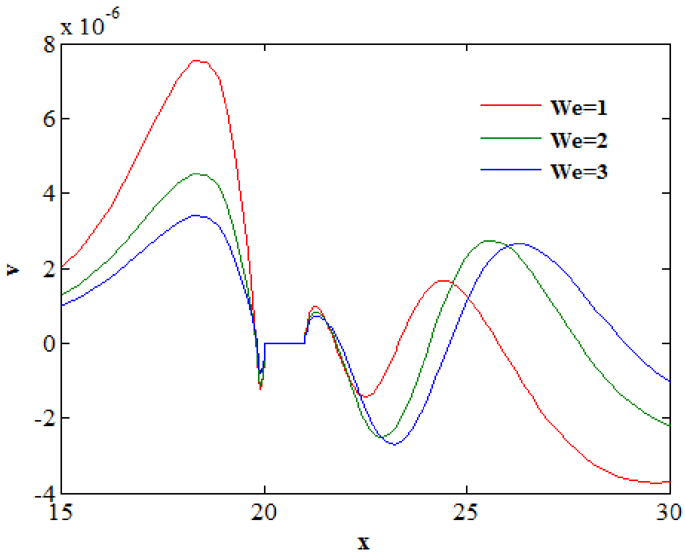

(b)Re=20

Figure 4.6 Velocity component, v, profiles at y=2 (a) and (b) for PTT fluid (c) and (d) for Oldroyd-B fluid.

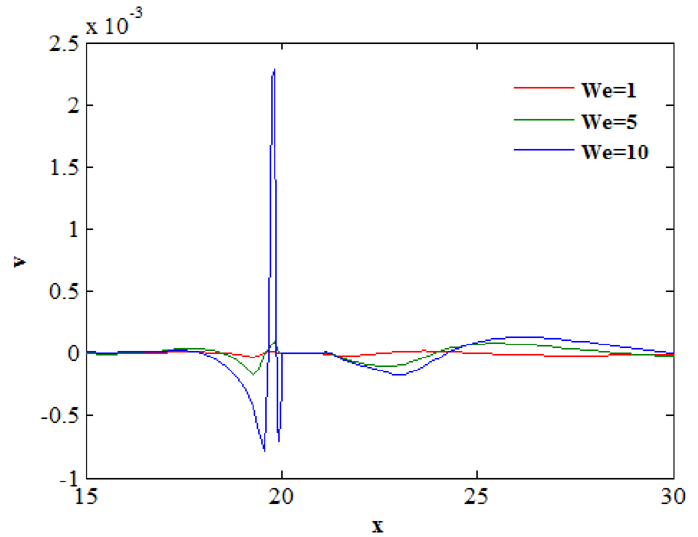

(c)Re=0

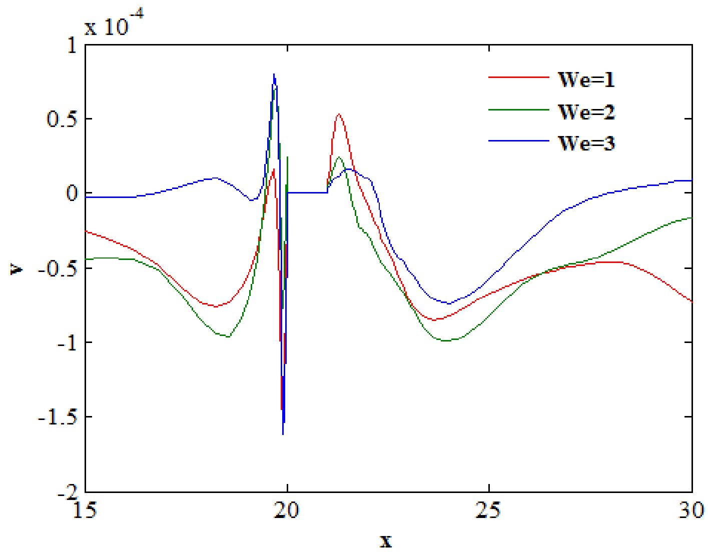

(d)Re=20

Figure 4.6 Velocity component, v, profiles at y=2 (a) and (b) for PTT fluid (c) and (d) for Oldroyd-B fluid (continued).

Figure 4.7 shows the pressure variation in the flow. For viscoelastic flow case, pressure gradients are generated by mainly elastic effects in near front and rear stagnation points of the cylinder. Viscoelastic pressure drop values are also higher than Newtonian flow case due to increasing effect of longitudinal flow as seen in Figure 4.7.

Figure 4.7a and Figure 4.7b depicts pressure profiles for PTT flow. As *We* increases, pressure value decreases as shown in Figure 4.7a, b, c. This result can be attributed to the smaller extensional viscosities associated with higher *We* for a PTT fluid. However, at *Re*=20, pressure drop gets amplified as in Figure 4.7d due to the breaking of the fore-aft symmetry of flow around obstacle at higher *We* (see Figure 4.5h). It can be concluded that, shear thinning property of the PTT fluid causes lower pressure drop compared to the Oldroyd-B fluid.

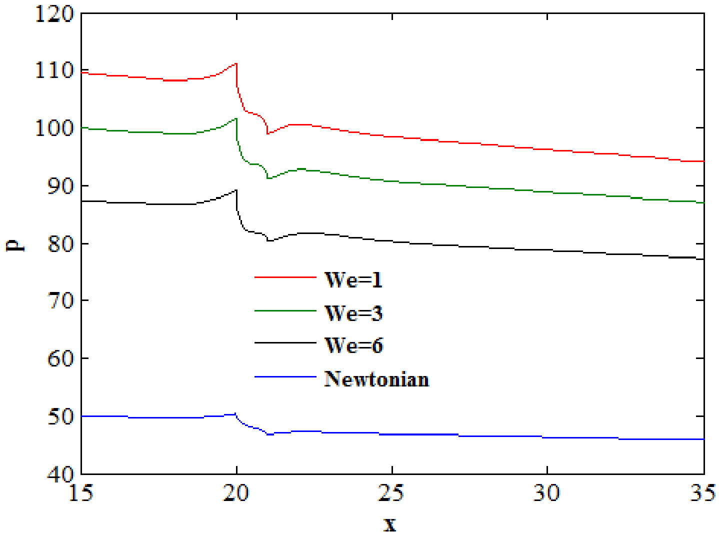

(a)Re=5

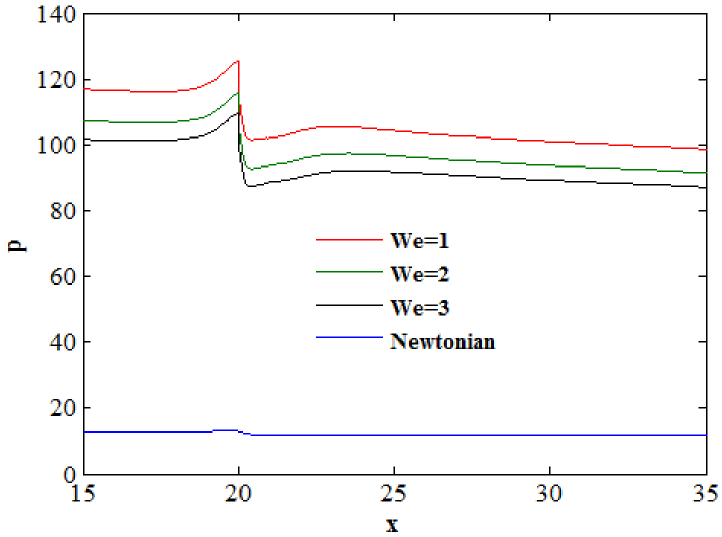

(b)Re=20

Figure 4.7 Pressure profiles around the cylinder (a) and (b) for PTT fluid (c) and (d) for Oldroyd-B fluid along the centerline.

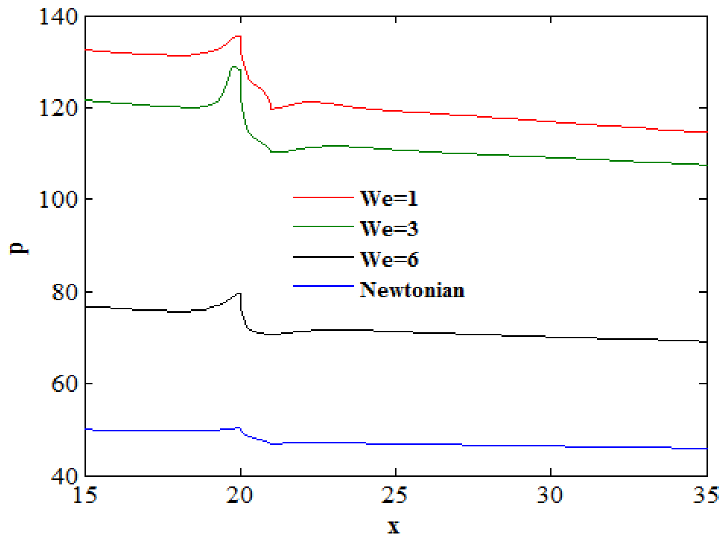

(c)Re=5

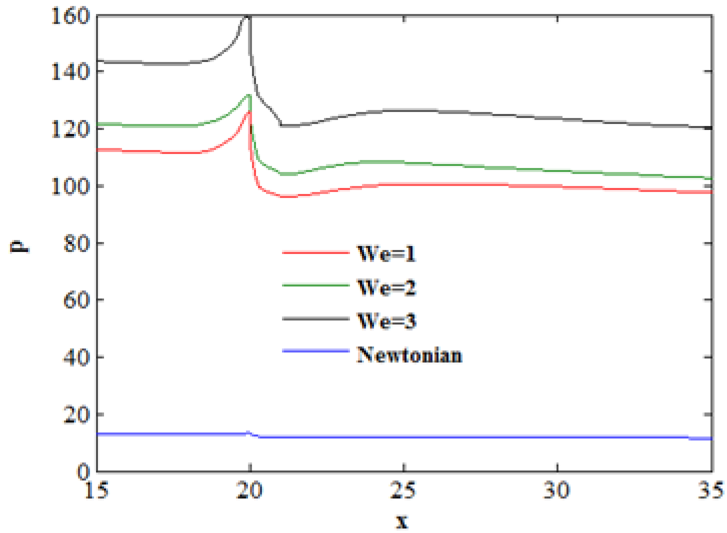

(d)Re=20

Figure 4.7 Pressure profiles around the cylinder (a) and (b) for PTT fluid (c) and (d) for Oldroyd-B fluid along the centerline (continued).

4.2.3. Normal and Shear stress profiles around the obstacle

In order to further examine the behavior of viscoelastic flows around the obstacle, we plot shear and normal stress profiles as in Figures 4.8 and 4.13. τ_{xx} and τ_{xy} variation around the cylinder are given along x and y direction of the flow. Both shear and normal stresses are zero at the front and the rear stagnant points since the velocity gradient ($\partial u/\partial x=0$) is zero at the centerline as in Figures 4.8 and 4.12. In the case of PTT fluid, at *Re*=0 and 10, absolute value of normal and shear stresses decreases as *We* increases due to stress decaying of flow field as shown in Figure 4.8. Higher the *We* is, stronger the shear thinning effects that lead to the lower stress values as depicted in Figure 4.8b and 4.10b.

As the inertial effects get amplified, τ_{xx} and τ_{xy} along the x direction becomes smaller at y=0. Also, shear stress peak is observed at the front stagnation point due to sudden change in the boundary condition (at singularity point) for all *We* numbers as shown in Figure 4.10a.

For the Oldrody-B fluid, absolute magnitude of stresses increases compared to PTT in the flow field. In Figure 4.9a overshoot in τ_{xy} profile occurs at *We*=15. It may be resulted from u velocity gradient with respect to y direction at x=19 (see Figure 4.5c). On the other hand, as *We* gets higher, there is an increase in all stress gradients as shown in Figure 4.9b and 4.11b. The saturation of normal stresses at the obstacle surface was also observed in creeping flow of Oldroyd-B fluid around cylinder [43].

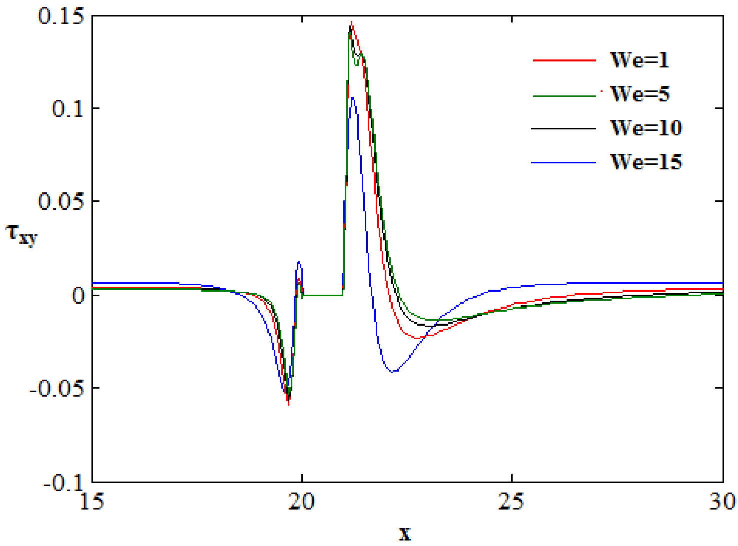

(a)

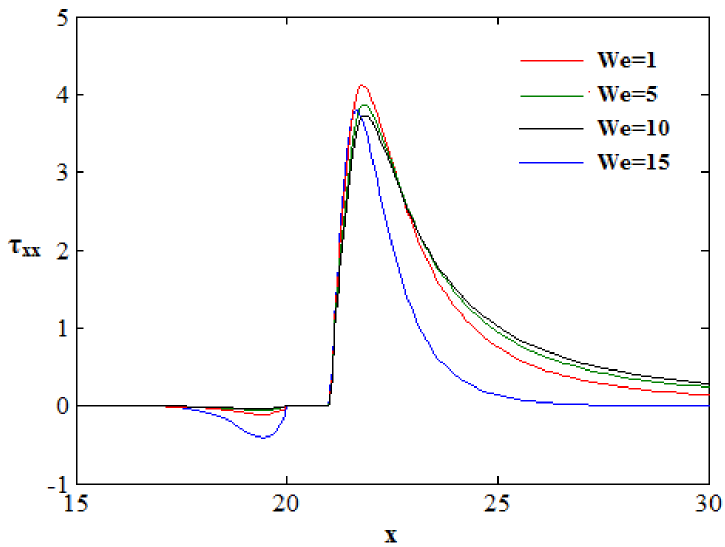

(b)

Figure 4.8 Shear stress, τ_{xy}, and normal stress, τ_{xx}, profiles around the obstacle for PTT fluid at Re=10^{-4}.

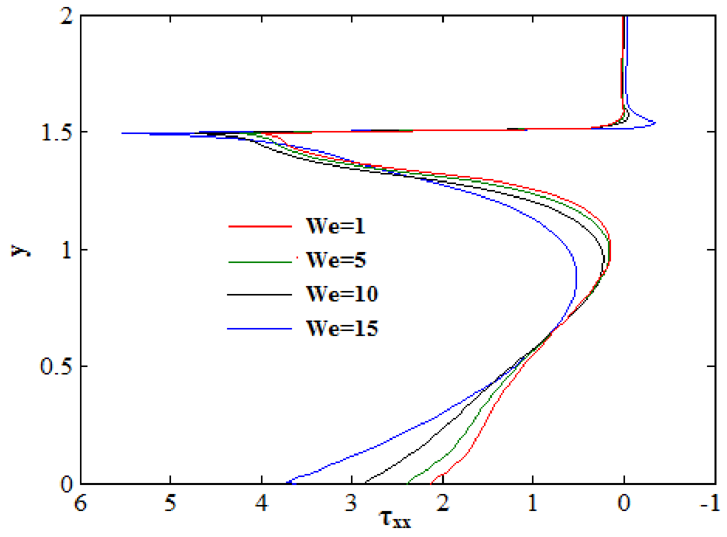

(c)

Figure 4.8 Shear stress, τ_{xy}, and normal stress, τ_{xx}, profiles around the obstacle for PTT fluid at Re=10^{-4} (continued).

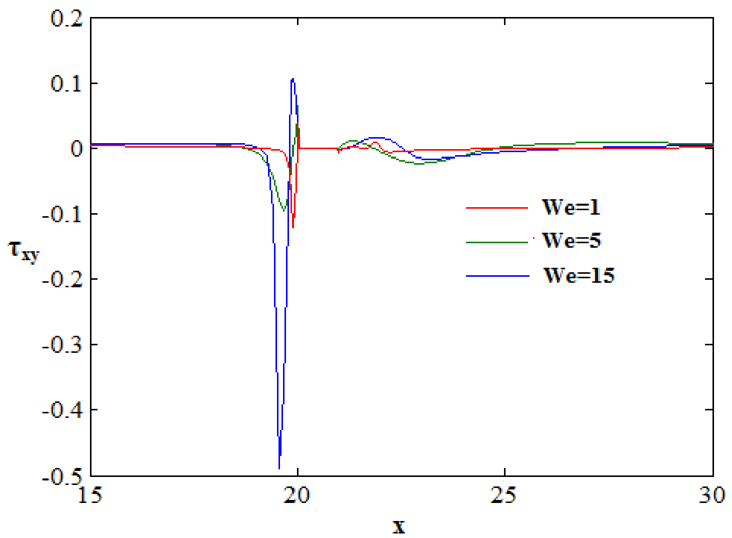

(a)

Figure 4.9 Shear stress, τ_{xy}, and normal stress, τ_{xx}, profiles around the obstacle for Oldroyd-B fluid at Re=10^{-4}.

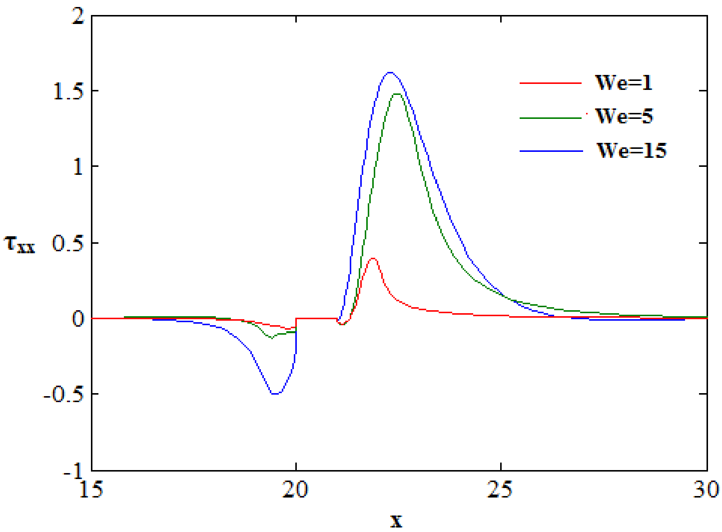

(b)

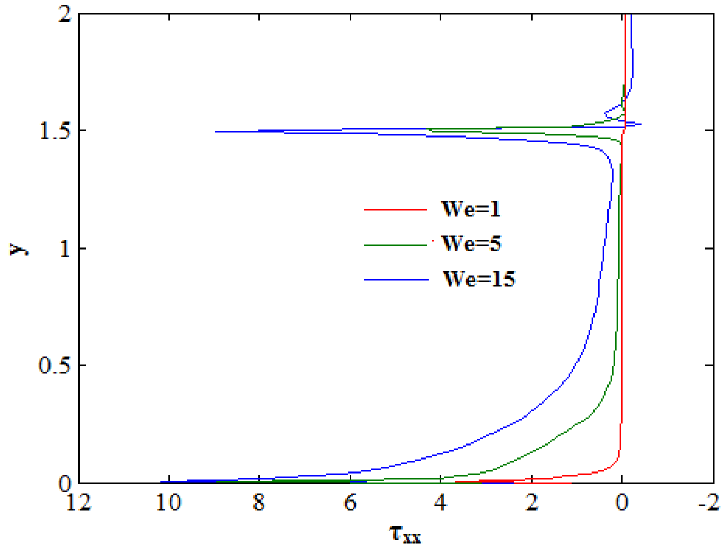

(c)

Figure 4.9 Shear stress, τ_{xy}, and normal stress, τ_{xx}, profiles around the obstacle for Oldroyd-B fluid at Re=10^{-4} (continued).

At *Re*=10, for PTT in the wake region, shear stress relaxation occurs in an oscillation manner as in Figure 4.10a. However, Oldroyd-B have more absolute shear stresses, stress relaxation is more quickly and suddenly owing to more flexible behavior of polymer chain, when the stress source removed (away from the cylinder), it is returned into undeformed case of the flow as in Figure 4.11a.

Another important flow feature is the response of normal stress behavior along the obstacle surface at x=20 (see Figure 4.10c and 4.11c). Normal stresses can be considered conceptually due to the tension of the streamlines of the flow field. Normal stress relaxation or distribution occurs between the obstacle surface and the channel wall at y=0. PTT fluid delays τ_{xx} momentum transfer from the obstacle surface to the channel wall.

Near the obstacle walls, the deformation rate of the fluid gets higher that in turn results in decrease in the shear viscosity decreases along with the normal stress. For Oldroyd-B fluid, all elastic or normal stresses are nearly recovered as suggested by the plots in Figure 4.9c. However, as *Re* increases, elastic stresses reach a maximum value (*We*=5) at the channel wall as in Figure 4.11c. Oldroyd-B flow relaxes quickly elastic stresses at the center of obstacle compared as PTT flow.

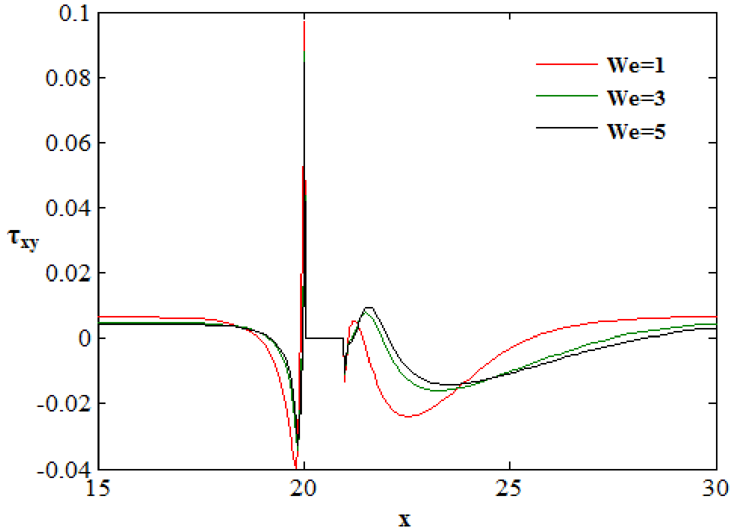

(a)

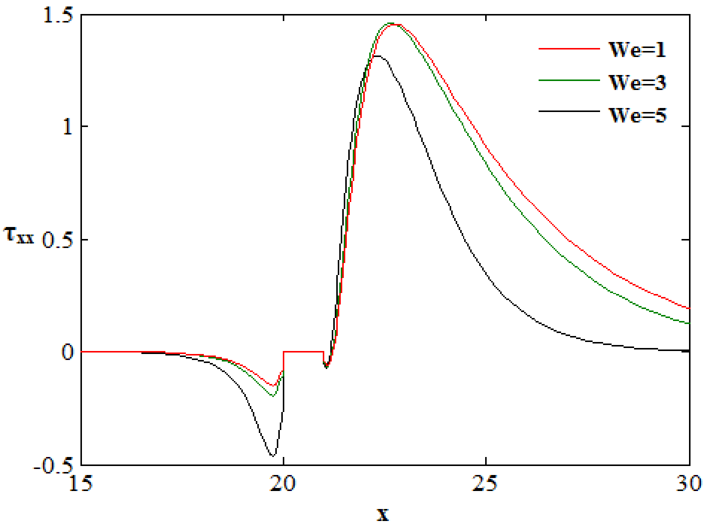

(b)

Figure 4.10 Shear stress, τ_{xy}, and normal stress, τ_{xx}, profiles around the obstacle for PTT fluid at *Re*=10.

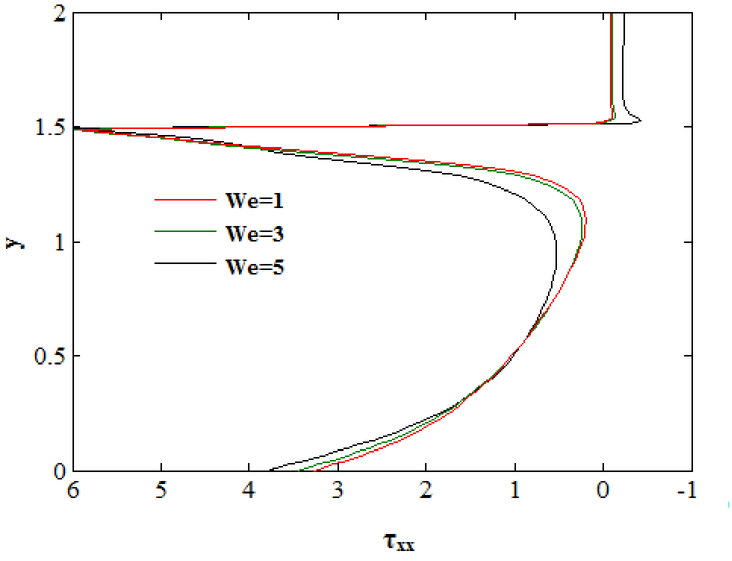

(c)

Figure 4.10 Shear stress, τ_{xy}, and normal stress, τ_{xx}, profiles around the obstacle for PTT fluid at *Re*=10 (continued).

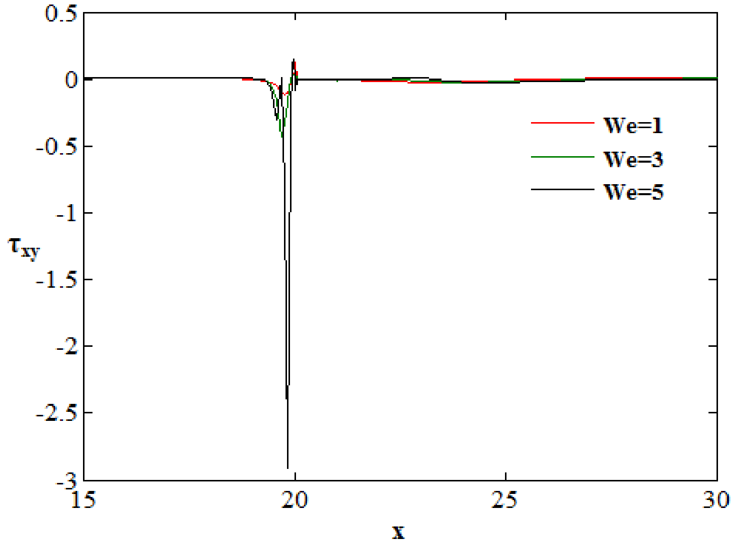

(a)

Figure 4.11 Shear stress, τ_{xy}, and normal stress, τ_{xx}, profiles around the obstacle for Oldroyd-B fluid at *Re*=10.

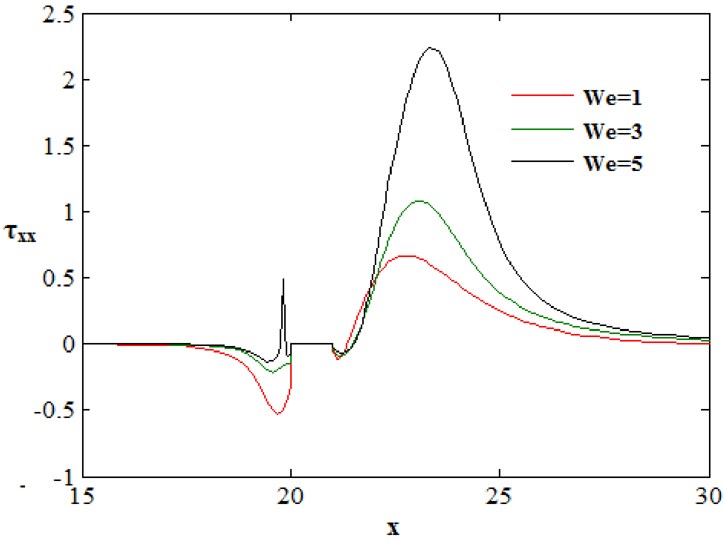

(b)

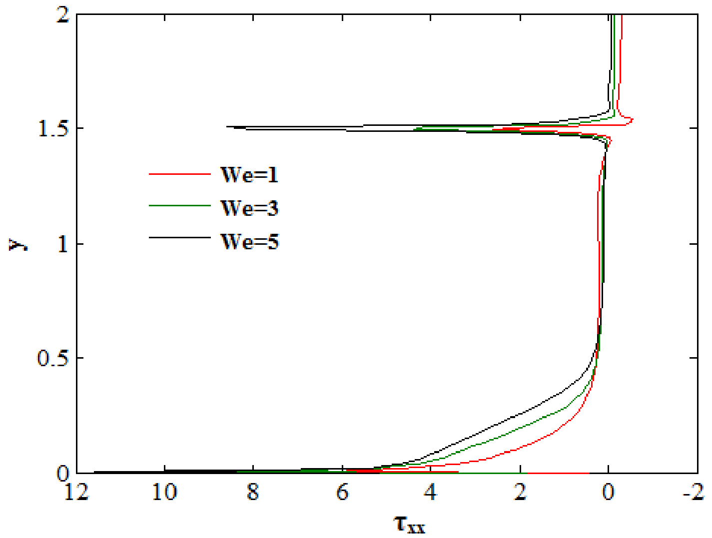

(c)

Figure 4.11 Shear stress, τ_{xy}, and normal stress, τ_{xx}, profiles around the obstacle for Oldroyd-B fluid at *Re*=10 (continued).

Figures 4.12 and 4.13 show shear and normal stresses at different positions for both PTT and Oldroyd-B fluids. At *Re*=20, nonlinear inertial forces become dominant. Observations suggest that the shearing properties of the fluid get stronger with increasing elongational properties. At the center of the channel (y=2), shear stresses get higher value especially for Oldroyd-B fluid at *We*=3 in Figure 4.12a. Figure 4.12b also depicts that there is a remarkable asymmetry shear stresses between upstream and wake region at the vicinity of the obstacle (y=2.5). Y. Xiong et al. [43] also observed asymmetry for Oldroyd-B flow around a circular cylinder. In the wake region, while shear stress diminishes, normal stresses become dominant (see Figure 4.13b).

Figure 4.13 illustrates distribution of normal stresses at the front (x=20) and back (x=21) surfaces of the obstacle along the channel height. Stress profiles in the case of Oldroyd-B fluid are more steep than than those of the PTT fluid. The profiles at the front of the obstacle exhibit smooth increasing or decreasing pattern as opposed to those at the back of the obstacle for both fluids. For example especially as elasticity of the fluids get stronger, two maxima are observed near the walls of the channel and obstacle.

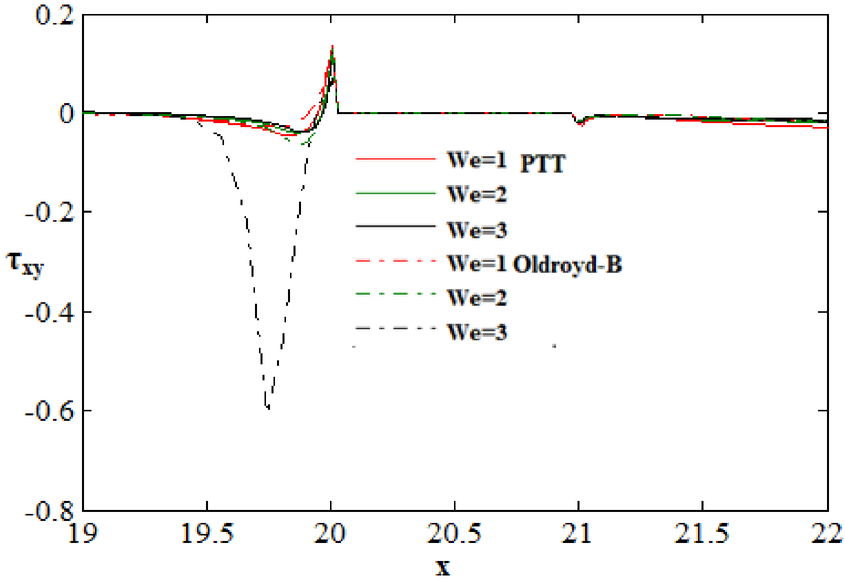

(a)

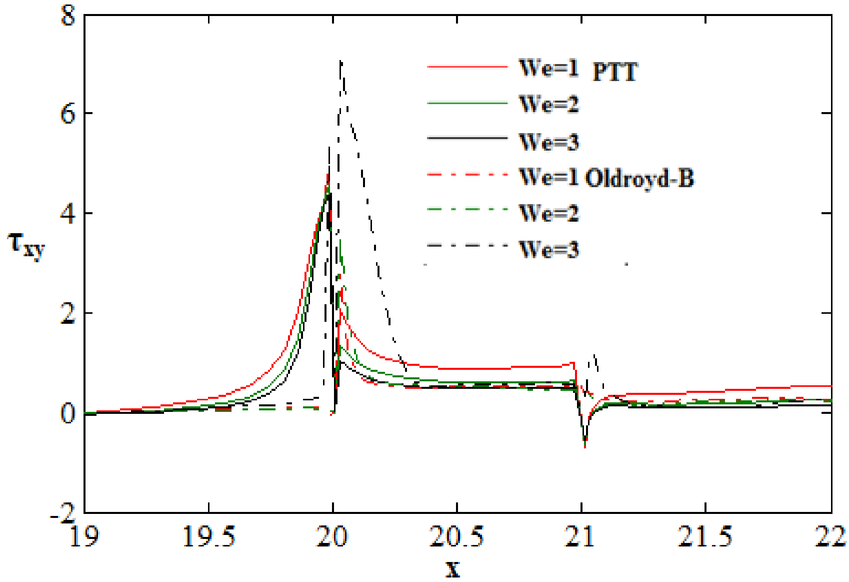

(b)

Figure 4.12 Normal stress, τ_{xy}, comparison around obstacle for Oldroyd-B and PTT fluid at *Re*=20 (a) center at y=2 and (b) at y=2.5.

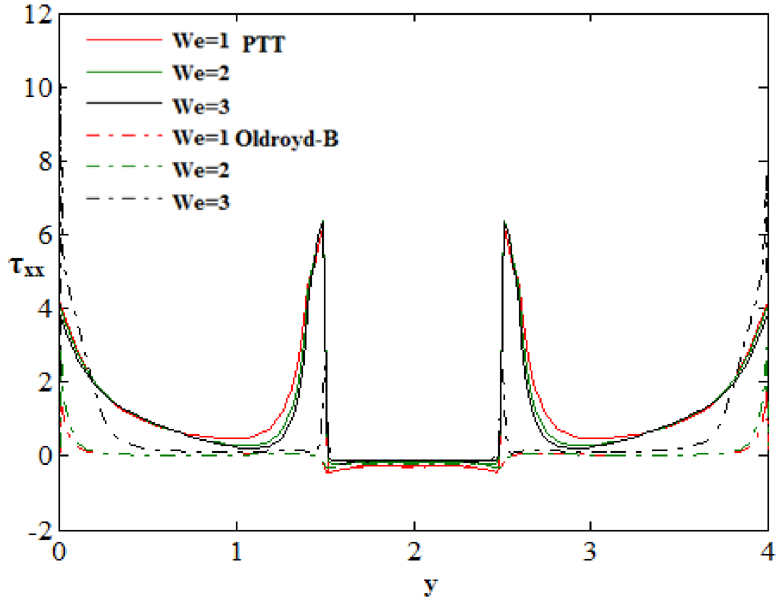

(a)

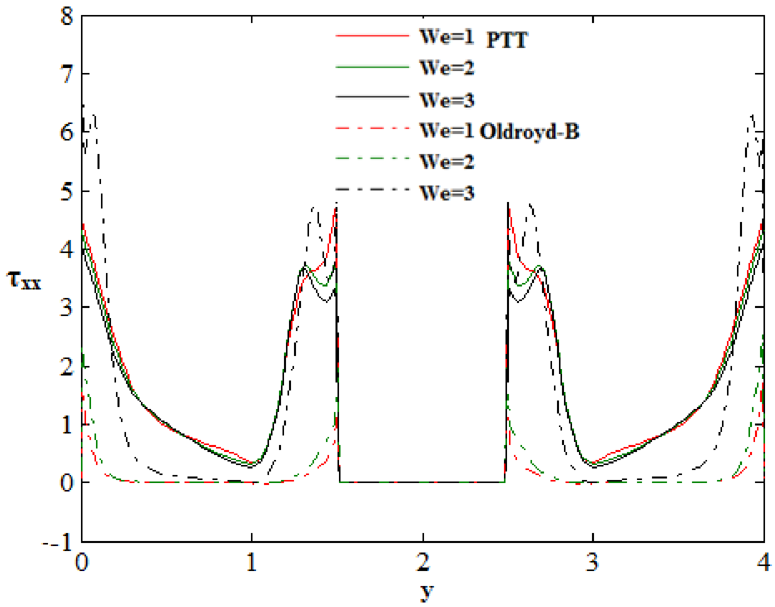

(b)

Figure 4.13 Normal stress, τ_{xx}, comparison around obstacle for Oldroyd-B and PTT fluid at *Re*=20 along the obstacle surface (a) x=20 and (b) x=21.

Figures 4.14-18 show representative contours of normal and shear stresses around the obstacle. Figures 4.14a and 4.14d show the effect of the *We* numbers on the dimensionless magnitude of normal stress component τ_{xx} at the creeping flow condition. Dimensionless contour values in the figures are 1 and -0.1. The stress field is symmetric as expected and overall stress patterns resemble closely for both fluid model in the corresponding regime. However, stress gradient is different each other. Another interesting observation is that at the top and bottom surfaces of the normal stresses extend further in the flow direction. These stress contours extend longer distances in the wake region as *We* is increased as in Figures 4.14a, c, 4.15a, c and 4.16a, c. This is an expected result since higher relaxation times lead to longer convection distances of the stresses. On the other hand, near the channel wall there is no such increasing or decreasing pattern of the stress with respect to *We* for PTT fluid in Figure 4.14a. However, for Oldroyd-B flow when *We* is 5 and 15, normal stresses effects increase near the channel wall as in Figure 4.14c (see Figure 4.9c).

Figure 4.14b and 4.14d give negative normal stresses, -0.1, around the obstacle. They predominantly occur in front of the obstacle. At the highest fluid elasticity, *We*= 15, no negative normal stress is observed in Figure 4.14b and 4.14d. Normal stresses are in tensile in nature as opposed to compressive type. Diverted flow near the leading front of the obstacle gives rise to the Hoop stresses generated by normal stresses. At lower *We*, in this flow region one can then expect negative or compressive stresses associated with the faster relaxation than that of higher *We*. Negative stress has the same approach for range of *We* for both model (see Figure 4.15b, d and 4.16b, d).

Figures 4.15 and 4.16 illustrate normal stress field at *Re*=10 and *Re*=20, respectively. Contour values in the figures are the same as that of Figure 4.14. The figures depict that as the fluid inertia increases the stress fields in the wake region get larger and eventually encapsulate the region developed at the top and bottom surfaces of the obstacle. At *Re*=20, flow circulations behind the object in Figure 4.2c lead to the division of the stress field behind the object into two symmetric regions as shown in Figure 4.16a due to shear thinning effect.

However, for Oldroyd-B flow, normal stress wake becomes longer, extending to nearly the whole length of the channel displayed in Figure 4.16c. With increasing *We*, the variation of the pressure near the cylinder surface is large. It can be seen that there is a strong pressure gradient around the cylinder for $We > 1$, produced by the stress boundary layer on the surface of cylinder. There is also a large pressure gradient in the wake (see Figure 4.7d). Another impact of these circulations is the formation of negative stress fields in the wake region associated with the hoop stresses as in Figures 4.16b and 4.16d with range of *We* numbers. At We=3, there is no negative normal stress in the wake as shown Figure 4.16d. As inertial effects increases, Hoop stresses at contour value of 1 is observed at high *We* flow (see Figures 4.15c and 4.16c).

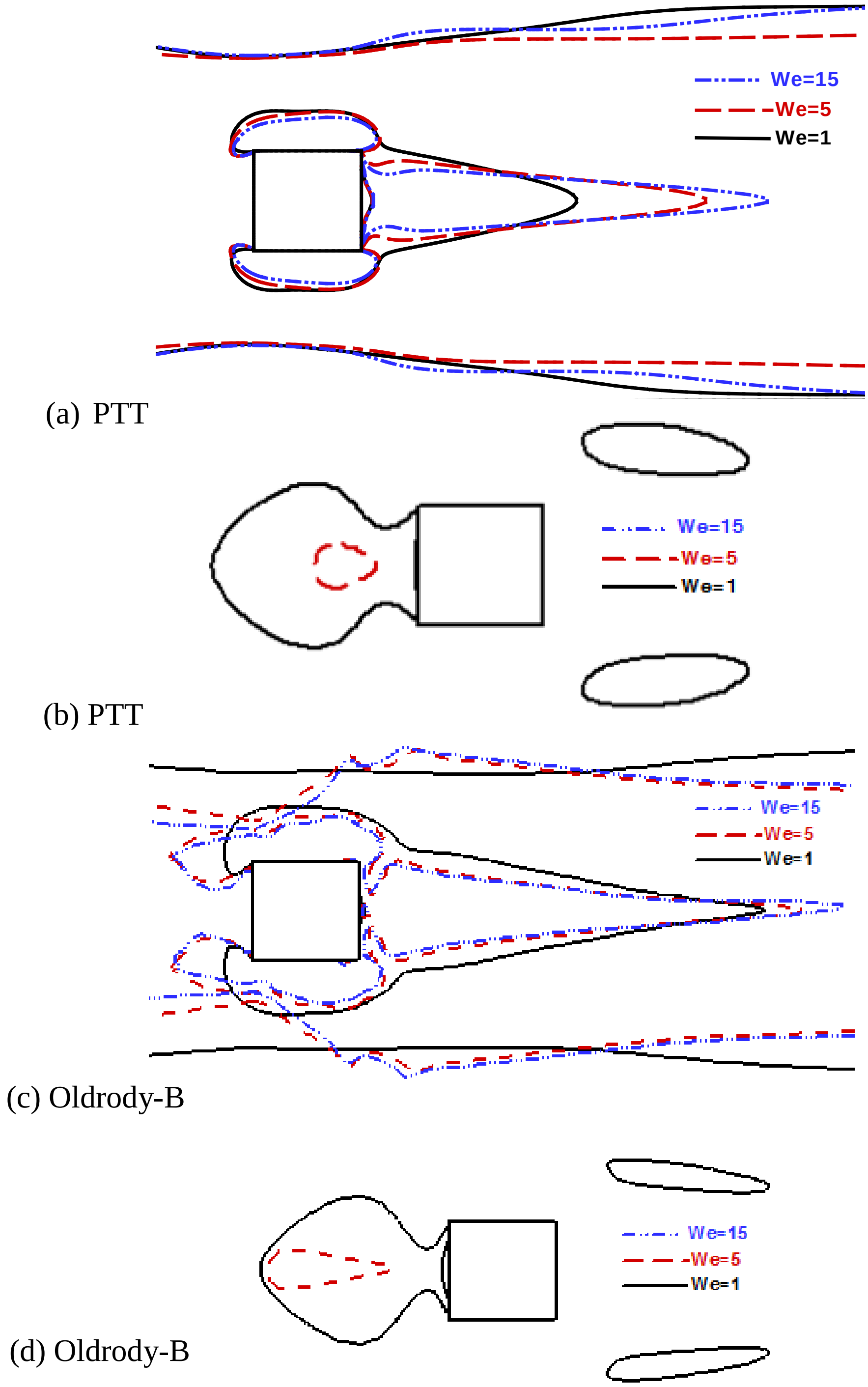

Figure 4.14 Effect of *We* on the normal stress component τ_{xx} at *Re*=0. Contour values are (a) and (c) 1 (b) and (d)-0.1 for PTT and Oldroyd-B.

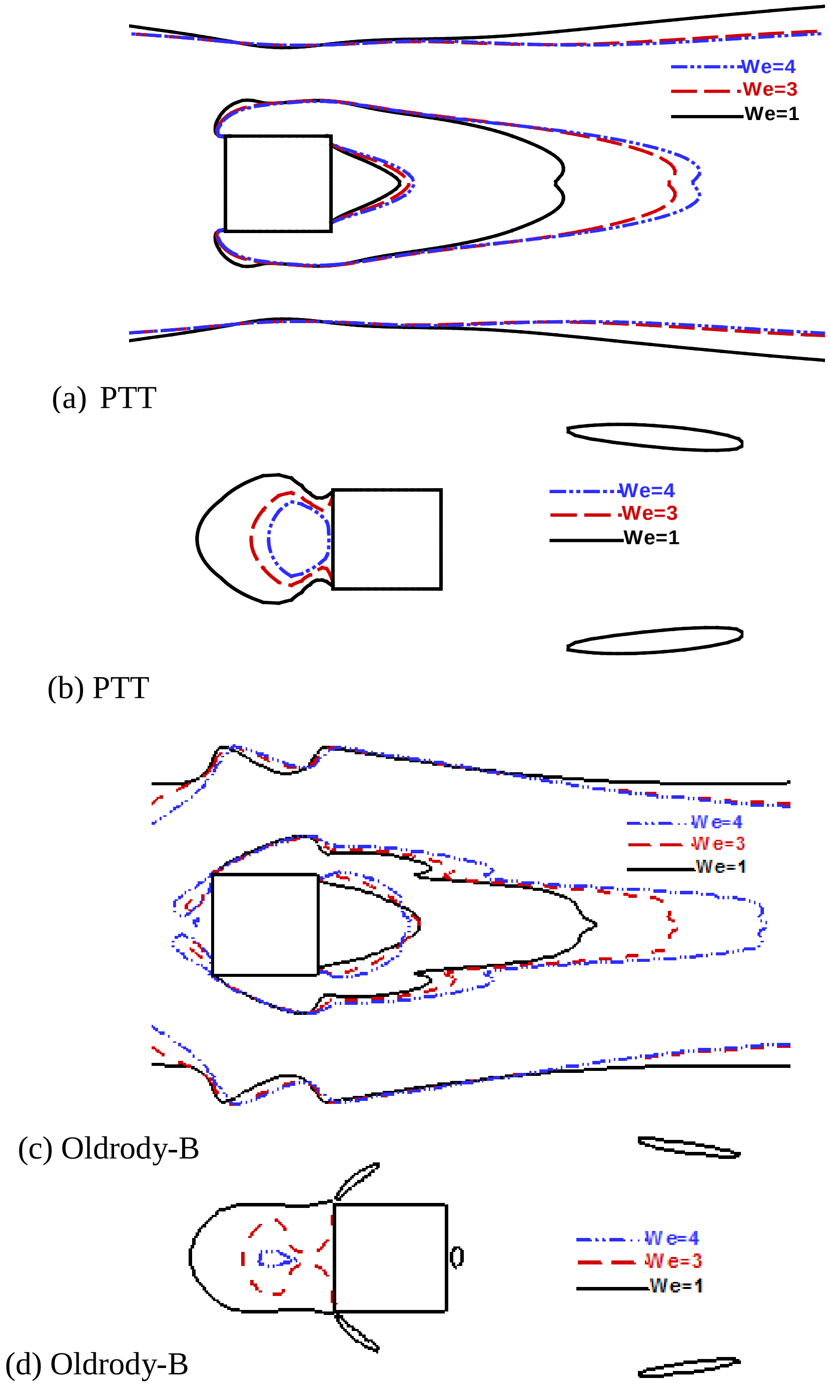

Figure 4.15 Effect of *We* on the normal stress component τ_{xx} at *Re*=10. Contour values are (a) and (c) 1 (b) and (d)-0.1 for PTT and Oldroyd-B.

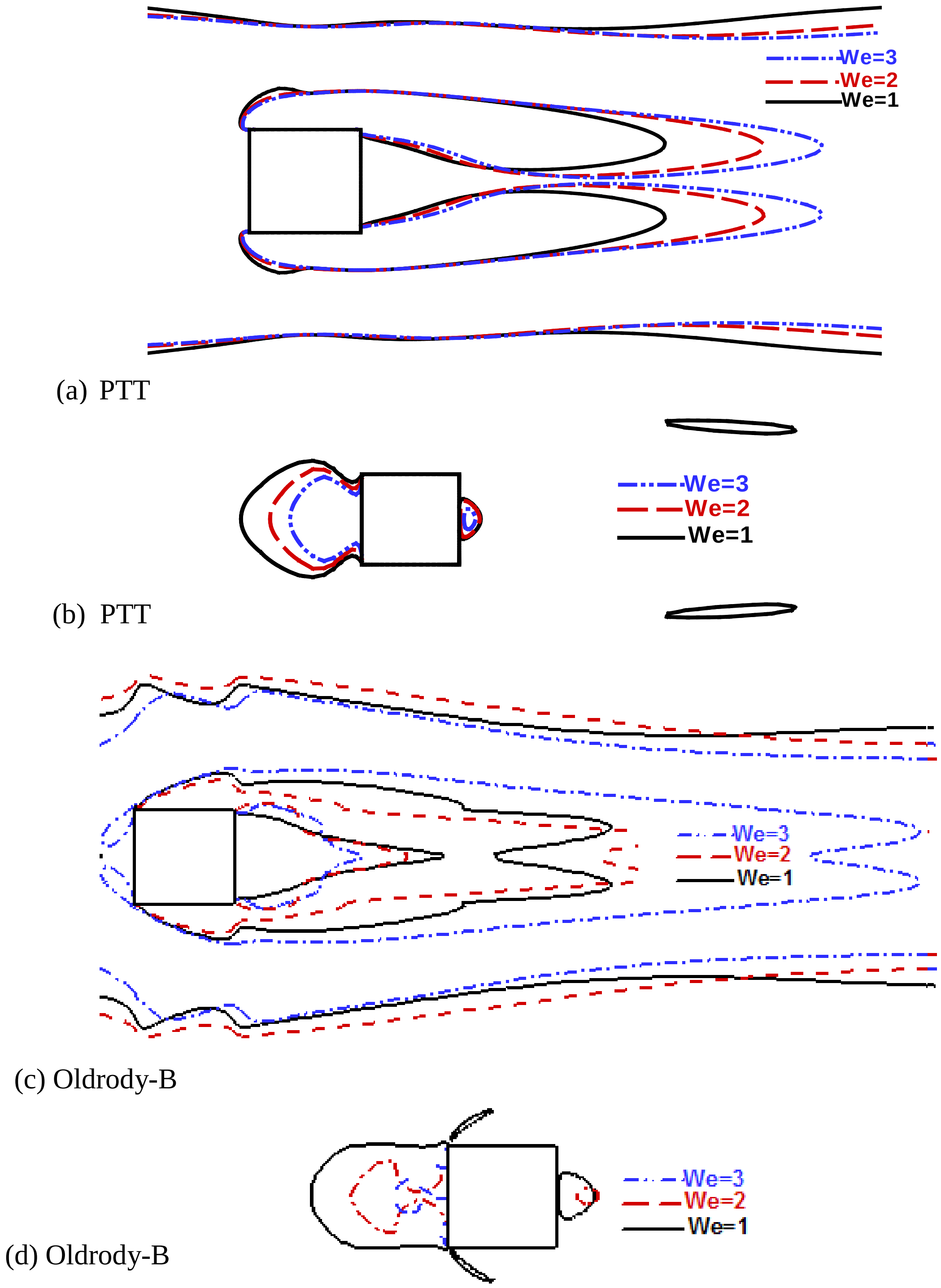

Figure 4.16 Effect of *We* on the normal stress component τ_{xx} at *Re*=20. Contour values are (a) and (c) 1 (b) and (d)-0.1 for PTT and Oldroyd-B.

Figures 4.17 and 4.18 show the effect of the *Re* on the shear stress field, τ_{xy}, at *We*=3, ε=0.25 and β=0.2 for PTT and ε=0 for Oldroyd-B flow, respectively. Several features in the shear stress field are interesting. For example high values of the stress first appears at the front corners of the object where highest contribution of the Hoop stresses can be expected due to sudden turn in the flow as in Figures 4.17 and 4.18. Their contribution to the stress field can also be observed at the back corners especially at creeping flow condition as shown in Figures 4.17a and 4.18a.

Due to the flow separation at higher *Re*, shear stresses become relaxed as depicted in Figures 4.17b and 4.18b. For Oldroyd-B shear stress elongates through the flow direction in sharper form in Figure 4.18b. Higher values of the shear stress at the front corners eventually extend to the upper and lower surfaces as *Re* increases.

Therefore these findings confirm that, shear stresses occur in the region dominated by the flow tangential to the solid boundaries and that shear stresses get amplified. At high *Re*, shear stress contours become more smooth. Stress contour density decreases around the obstacle surfaces. Flow is also more stabilized due to relaxing of shear stresses in Figures 4.17c and 4.18c (see Figures 4.12a and 4.12b).

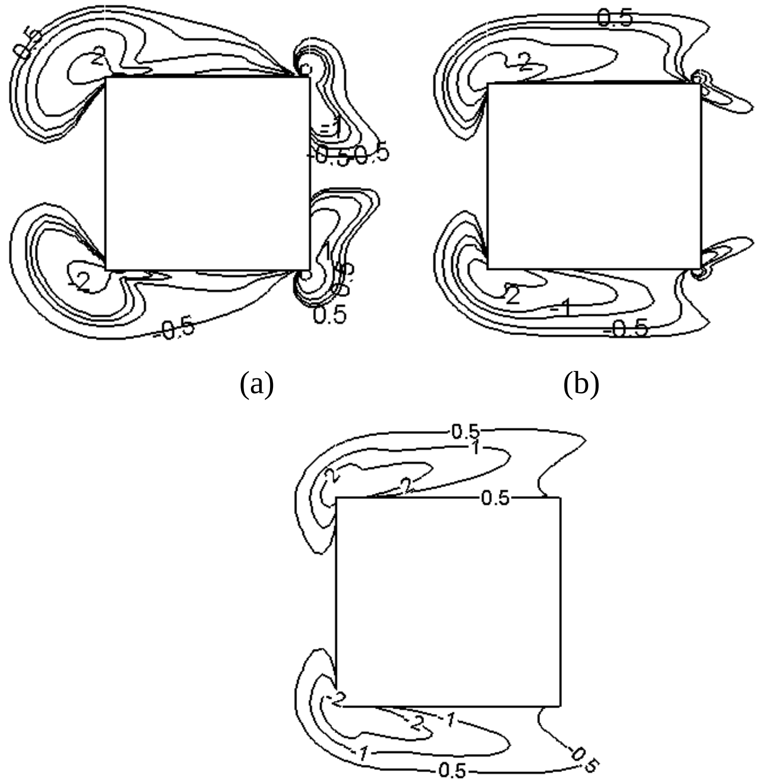

(a) (b)

(c)

Figure 4.17 Effect of fluid inertia on shear stress field, τ_{xy}, for PTT fluid around the obstacle at *We*=3, ε=0.25 and β=0.2 for a) *Re*=0 b) *Re*=10 and c) *Re*=20

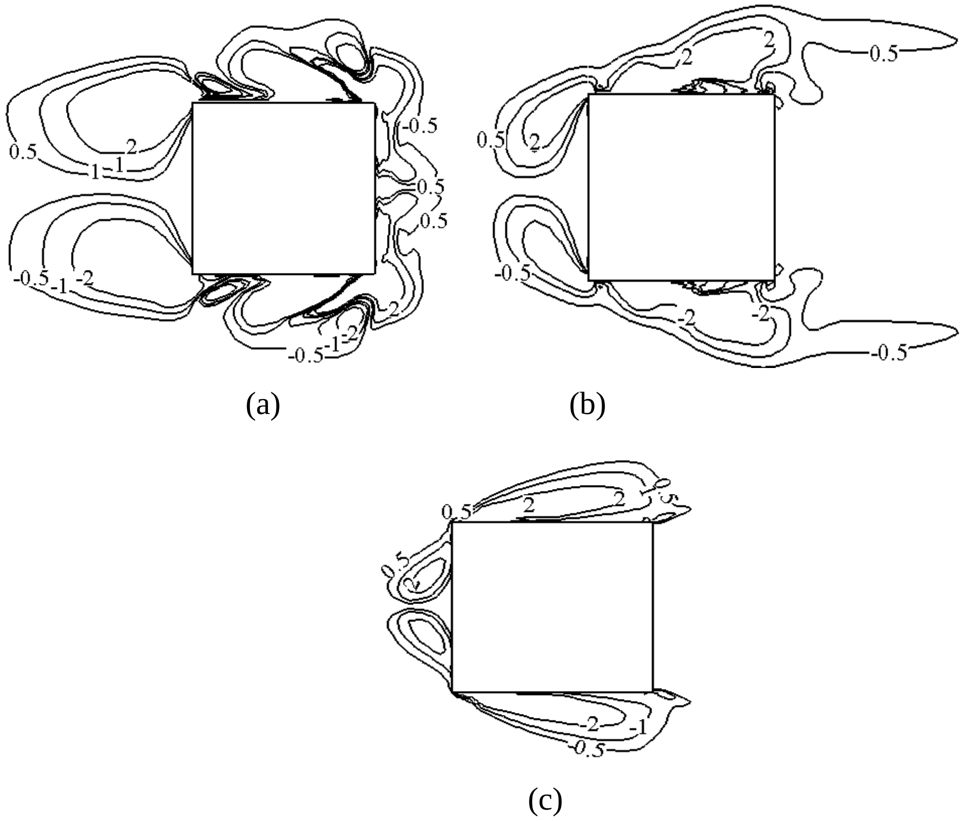

Figure 4.18 Effect of fluid inertia on shear stress field, τ_{xy}, for Oldroyd-B fluid around the obstacle at *We*=3, ε=0 and β=0.2 for a) *Re*=0 b) *Re*=10 and c) *Re*=20.

4.3.Viscoelastic Drag Phenomena over the square cylinder

Drag coefficient is obtained by integrating the stress and pressure contributions over the square cylinder surfaces denoted as *f* front, *r* rear, *t* top, and *b* bottom similar to the methodology reported by Dhiman et al. [11] The relation for *Cd* can be written as:

$$Cd = \frac{2}{\mathrm{Re}}\int_0^1 [(\tau_{xx,r}(y) + \tau_{xx,f}(y))dy + (\tau_{xy,t}(x) + \tau_{xy,b}(x))dx] + 2\int_0^1 [(P_r(y) - P_f(y))dy] \quad (4.1)$$

The corresponding drag coefficient can be splitted into three parts. These are drag coefficient due to normal stress contribution, drag coefficient due to shear stress contribution, drag coefficient due to pressure drop contribution. All these contributions are expected to be functions of *Re* and *W*e numbers and also coupled each other. This relationship is investigated in this section.

At constant *Re* results of the two different mesh size, 372x162 and 372x81, are included in Table 4.4 in order to reveal the possible impact of the mesh size on the computational results. Negligible differences between the results of the meshes indicate the computational results are free of the mesh structures used in this study. Therefore in the following sections, the presented results were obtained by using 372x162 cells.

The effects of increasing viscoelasticity and fluid inertia on *Cd* are given in Table 4.4 for PTT fluid. The first striking feature is higher *Cd* values at non-zero *We* than those of Newtonian fluid in Table 3.2 at a given *Re*. Interestingly, further increase in *We* leads to the smaller *Cd* values as shown in Table 4.4. This behavior suggests that up to a certain critical *We* value, that seems to be between 0 and 1, normal stresses play a significant role in the increase of *Cd* as tabulated in Table 4.6 especially after *We*>0.8. Beyond that critical *We=1*, shear thinning becomes more and more pronounced to counter the normal stresses. Hence, decrease in *Cd* is observed with respect to increasing *We* at a given *Re* as depicted in Table 4.4. This trend is also clear in Table 4.5 in terms of *Cd** values normalized with *Cd* at *We*=0.

The combined effects of elasticity and shear thinning properties are not really distinguishable for viscoelastic effects on the drag at the very low Reynolds number. Flow behaviour differences diminish and drag values approach each other. However, for viscoelastic flow drag coefficient has larger value due to higher viscous behavior than elastic behavior of the flow. Drag enhancement occurs compared with Newtonian flow as the *Cd** is higher than one. With increasing *We*, the drag correction factor (*Cd**) reaches smoothly up to nearly two times the Newtonian value. This behavior was also observed in earlier studies on the flow of PTT fluid around circular cylinder at *Re*=0 [44-46].

Pressure drop contribution to the drag force increases with increased *Re* number (see Figures 4.7a and 4.7b), while shear and normal stresses decays due to shear thinning effects. Table 4.4 also reveals that dependence of *Cd* on *Re* appears to be same as Newtonian fluid.

Inertia has decreasing effect on *Cd*. At a given *We*, say 1 or 2, there is a decreasing pattern in *Cd* behavior with respect to increasing *Re*. A reduction in *Cd* is observed when the value of *Re* is changed from 5 to 20 similar to Newtonian fluid case in Table 4.4. At high *Re* flows, shearing of the fluid will be more important to the viscous dissipation of PTT fluid than its elongational property. So, the discrepancies between Newtonian (*We*=0) and viscoelastic drag (*We*>0) are larger for *Re*=20. On the other hand, in the region of *Re*=5 and *Re*=10 the contribution of normal stresses to the Newtonian drag are of the same order magnitude for viscoelastic drag enhancement (around ~7%).

Table 4.7 shows drag coefficients variation with polymeric viscosity ratio. In our governing equations, polymer concentration effect is characterized by the polymer viscosity ratio, *wr*. Polymeric concentration affects both the viscosity and the relaxation time of polymer molecules in viscoelastic medium. We carry out a few tests for various *wr* for *We*=1, 2 and 3 at fixed *Re*=20 tabulated in Table 4.7. Although shear and normal stresses contribution to drag increase, the variation of *Cd* is nearly same for the range of

We. However, pressure drop contribution has slightly increased with *wr*. The higher is the value of *wr*, the more drag enhances for *We*=3 case due to increased elasticity effect.

In the case of Oldroyd-B fluid, investigation of drag coefficients becomes more involved due to occurance of higher stress gradients than those of PTT fluid as shown in Figures 4.14-17. The drag increases with *We* number as tabulated in Table 4.8. This increase in drag is associated with a remarkably long recirculation region as shown in Table 4.1. Another reason is the formation of Hoop stresses at high *We* flows in the wake region. For PTT fluid, this region is more stabilized owing to decaying of stress field as shown in 4.16a.

When *We* increases, shear and normal stresses contributions to drag coefficient are small due to constant viscosity of Oldroyd-B fluid at a given *Re*. At *Re*=5, up to *We*=4, there is an effective balance between normal stress and shear stress drag contribution leading to nearly the same drag coefficients. For *We*=5 and 6, pressure drop contribution to drag coefficient decreases because pressure magnitude suddenly drops as in Figure 4.7c, while the normal stress contribution to drag coefficients gets amplified. Furthermore, *Cd* increases slightly with increased *We* at high *Re*. This behavior of drag can be explained by the secondary flow formation resulting from vortex pairs in the wake region. They also cause overshoot of vertical velocity, v, (see Figure 4.6d) and break of fore/aft symmetry in streamwise velocity, u. (see Figure 4.5h).

At *Re*=20, large deformation is observed in normal stress field especially at *We*=3 as in Figure 4.16c. Therefore, normal stress contribution to drag coefficient increases from 85 to 108, along with stronger pressure contribution as shown in Table 4.8. Also, the rapid change of pressure and the formation of normal stress boundary layer generates high extensions and shears around the obstacle. For *We*<3, negative normal stress field around the obstacle has also decreasing effect in magnitude of normal stress contribution to drag coefficient (see Figure 4.17c).

Table 4.9 indicates that the drag coefficient becomes almost ten times larger than that of the Newtonian fluid when *We* increases due to stronger elastic effects. As demonstrated in Table 4.10, at higher *wr*, drag coefficient increases at a constant *We.* At high *We* flows, further increase of polymer concentration makes no significant contribution to drag force around the obstacle as shown in Table 4.10.

Table 4.4 Drag coefficients for PTT fluid at *Re*= 5, 10 and 20

Re	*We*	Pressure Contribution to *Cd* *(372x162)*	Shear Stress Contribution to *Cd* *(372x162)*	Normal Stress Contribution to *Cd* *(372x162)*	*Cd* *(372x162)*	*Cd* *(372x81)*
5	1	13.530	50.646	92.910	84.492	84.482
	2	11.542	50.537	86.760	78.273	78.002
	3	10.123	48.932	84.923	73.912	73.788
	4	9.923	32.874	81.125	65.652	65.439
	5	9.606	28.415	80.640	62.932	62.835
	6	9.317	21.912	78.120	58.738	58.647
10	1	15.917	51.961	83.391	59.023	58.904
	2	14.004	49.359	82.510	54.427	54.383
	3	13.118	38.317	71.370	48.412	48.174
	4	12.602	31.289	66.416	44.858	44.745
	5	12.124	29.812	62.136	43.012	42.869
20	1	21.483	49.076	75.840	55.512	55.456
	2	19.704	46.934	71.230	51.301	51.224
	3	18.950	39.357	70.370	48.998	48.874

Table 4.5 Drag coefficients for PTT fluid at Re=0.0001 where *Cd*=Cd/Cd* at *We*=0

We	*Cd*	*Cd**
0	7.114×10^5	1.000
1	1.984×10^6	2.789
5	1.557×10^6	2.189
10	1.428×10^6	2.007
15	1.369×10^6	1.924

Table 4.6 Drag coefficients for PTT fluid at *Re*=20 for low *We*≤1 flows

We	**Pressure Contribution to *Cd***	**Shear Stress Contribution to *Cd***	**Normal Stress Contribution to *Cd***	***Cd***
0	2.261	1.821	-	4.702
0.1	6.089	8.481	11.250	14.152
0.2	9.492	16.167	20.255	22.627
0.3	12.471	23.050	28.810	30.123
0.4	15.025	29.155	36.942	36.660
0.5	17.151	34.457	44.624	42.218
0.6	18.860	38.969	51.865	46.804
0.7	20.141	42.670	58.660	50.410
0.8	21.050	45.590	64.310	53.089
0.9	21.345	47.665	72.232	54.669
1	21.483	49.076	75.840	55.456

Table 4.7 Drag coefficients for PTT fluid at *Re*=20 for different polymer viscosity ratio

We	***wr***	**Pressure Contribution to *Cd***	**Shear Stress Contribution to *Cd***	**Normal Stress Contribution to *Cd***	***Cd***
1	**0.5**	21.076	39.264	58.813	51.960
	0.6	21.131	34.884	62.087	51.959
	0.7	21.290	41.441	73.045	54.030
	0.8	21.483	49.076	75.840	55.456
2	**0.5**	18.727	33.503	47.132	45.517
	0.6	18.841	38.548	49.264	46.463
	0.7	19.147	44.937	65.063	49.294
	0.8	19.704	46.934	71.230	51.224
3	**0.5**	18.079	29.123	45.342	43.604
	0.6	18.342	34.456	55.654	45.695
	0.7	18.920	37.342	63.651	47.939
	0.8	18.951	39.357	70.370	48.874

Table 4.8 Drag coefficients for Oldroyd-B fluid at *Re*= 5, 10 and 20

Re	*We*	Pressure Contribution to *Cd*	Shear Stress Contribution to *Cd*	Normal Stress Contribution to *Cd*	*Cd*
5	1	21.017	111.277	117.345	133.484
	2	19.752	118.123	119.123	134.402
	3	18.807	119.860	121.854	134.310
	4	17.494	120.037	129.797	134.922
	5	12.182	121.342	150.182	132.975
	6	11.176	122.959	160.955	139.917
10	1	16.062	105.028	114.612	76.051
	2	16.092	107.543	115.453	76.783
	3	16.149	109.912	118.582	77.821
	4	17.023	110.123	118.591	79.788
	5	17.699	114.723	119.400	82.222
20	1	18.595	94.852	83.381	55.013
	2	18.909	95.695	85.561	55.943
	3	22.642	96.088	108.727	65.767

Table 4.9 Drag coefficients for Oldroyd-B fluid at Re=0.0001 where *Cd*=Cd/Cd* at *We*=0

We	*Cd*	*Cd**
0	7.11×10^{5}	1
1	4.77×10^{6}	6.710
5	5.44×10^{6}	7.650
10	6.35×10^{6}	8.920
15	8.35×10^{6}	11.730

Table 4.10 Drag coefficients for Oldroyd-B fluid at *Re*=20 for different polymer viscosity ratio

We	***wr***	**PressureContribution to *Cd***	**Shear Stress Contribution to *Cd***	**Normal Stress Contribution to *Cd***	***Cd***
	0.5	16.453	42.234	44.321	41.561
1	**0.6**	17.262	43.564	49.124	43.792
	0.7	18.231	44.122	51.984	46.072
	0.8	18.595	44.852	53.381	47.013
	0.5	17.231	54.546	54.235	45.340
2	**0.6**	17.871	55.167	55.146	46.773
	0.7	18.453	55.875	55.456	48.039
	0.8	18.909	55.695	55.561	48.943
	0.5	22.134	56.972	65.123	56.477
3	**0.6**	22.345	57.012	66.341	57.025
	0.7	22.456	58.981	67.891	57.599
	0.8	22.643	59.0887	68.727	58.067

CHAPTER 5

COMPLEX FLOW RHEOLOGY ANALYSIS USING MRI (MAGNETIC RESONANCE IMAGING)

In this chapter, online and offline rheological measurements on complex fluid is presented in detail. Online measurements were performed with an MRI (Magnetic Resonance Imaging) at Food and Science Technology Department at University of California, Davis.

Offline methods for rheological measurements such as cylindirical coquette, cone and plate geometries (conventional rheometries) generally is used for the study of fluid motion in shear. However, obtained results from these types of geometries need to be verified with suitable online or inline methods. Especially, many industrial processes, such as extrusion, transfer processes involve established or developing flows in pipes or tubes. Therefore, online techniques based on the measurement of the velocity profile in a pipe flow using MRI, which is a non-invasive method, and simultaneously determining the pressure drop, are promising for use a product quality or rheology control tool during the fluid flow.

In this study, the application of MRI rheometry on the measurement of complex fluid such as CMC (Carboxylmethyl cellulose), and Carbopol solutions flow, there is no linear relationship between stress and shear rate in simple shear flow, was described in the following sections.

5.1. Introduction

Magnetic resonance imaging (MRI) can be used as a viscometer, based on analysis of a measured velocity profile of fluid flowing in a tube coupled with a simultaneous measurement of the pressure drop driving the flow [48]. This type of measurement is well suited for rheological characterization of non-Newtonian fluids.

MRI is based on the interaction between nuclear magnetic moments and applied external magnetic fields. MRI can be used to measure composition, structure, molecular mobility, molecular diffusion, and bulk material motion. In an MRI experiment, a sample is placed in a magnetic field within a radio-frequency probe, energy is added in the radio-frequency range, and the response of the material to that energy is recorded in terms of its attenuation, frequency, and phase [49].

MRI data can be made sensitive to a variety of variables including position, displacement, diffusion, velocity, density, relaxation times, or combinations of these. The MRI signal intensity, S, in the velocity-encoded images described in given by;

$$S(k_X, q_Z; T) = \int [\rho(x) \exp(i2\pi k_X) x \int P(\Delta z, x; T) \exp(i2\pi q_Z) d\Delta z] dx \qquad (5.1)$$

and is due to protons in the fluid, primarily from water. The expression for signal intensity in Equation (5.1) has a density component, a position component, and a displacement component. The variable k_x is the reciprocal space vector with units of 1/m and given by a product of the magnetogyric ratio (γ), the phase encoding gradient duration, and the applied phase encoding gradient. The variable qz is the reciprocal space vector of displacement with units of 1/m and is given by the product of γ, duration of the displacement encoding gradient, and the applied displacement gradient vector.

A two-dimensional Fourier transform with respect to *qz* and *kx* produces a map of $P(\Delta z, x; T)\rho(x)$ with respect to displacement Δz and position x. The product $P(\Delta z, x; T)\rho(x)$ is the conditional probability density that a nucleus at x will displace Δz within the pulse sequence time interval T, which is referred to as the flow time. The position-dependent density of spins attributed to each displacement is given by $\rho(x)$. The measurement of fluid velocity is accomplished through this displacement component (Δz) by measuring the distance a volume of fluid has moved in a specific time (T). When the motion is steady, the velocity is calculated from the ratio of the distance to the elapsed time. Details of the technique and applications are given by Callaghan [50] and McCarthy [51].

The MRI process viscometry requires that a well-defined flow field be established. To evaluate shear viscosity in tube (or capillary) flow, an incompressible fluid must undergo steady pressure-driven flow in the laminar regime. The conservation of linear momentum, which equates pressure forces to viscous forces, provides the relationship between the shear stress, σ, and radial position, r:

$$\sigma(r) = \frac{-\Delta P}{2L} r \tag{5.2}$$

where ΔP is the pressure drop over the tube length L. In tomography-based methods, the shear rate is obtained at the same radial position using the velocity profile obtained from a flow image. The expression for the shear rate in tube flow is:

$$\gamma(r) = \frac{dV(r)}{dr} \tag{5.3}$$

where v is the axial velocity. Using Equations 5.2 and 5.3, the apparent viscosity η is determined by the ratio of shear stress to shear rate:

$$\eta(r) = \frac{\sigma(r)}{\gamma(r)} \tag{5.4}$$

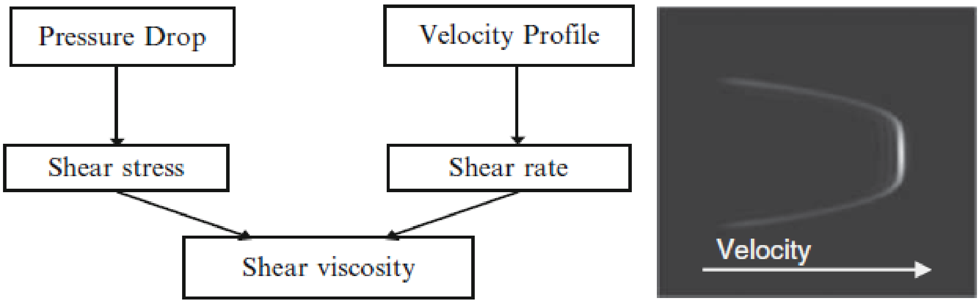

Figure 5.1 Data processing procedure and velocity image sample [52]

Graphical User Interface (GUI) programs were developed in the lab to analyze data and display results. This automation of data analysis provided rapid and consistent evaluation of multiple data sets. A schematic of the data processing steps and a sample velocity image are shown in Figure 5.1. Major steps in the data processing procedure include calculating the shear stress as a function of radial position in the pipe, processing the velocity profile image to obtain a velocity profile, calculating the shear rate as a function of radial position from the velocity profile, and generating the rheogram by plotting the shear stress against the shear rate [52]. Calculating the shear stress is straightforward from Equation 5.2.

Extracting the velocity profile from the image and calculating the shear rate data presents several challenges. The image data need to have sufficient signal-to-noise and sufficient velocity resolution to achieve a desired range of shear rates. The maximum shear rate is determined in the same manner as a conventional capillary viscometer (that being the shear rate at the wall). The minimum shear rate depends upon the velocity resolution [53-55]. After the appropriate velocity resolution is set and the image acquired, a velocity profile is extracted. Shear rates are calculated as a function of radial position by taking the derivative of the velocity profile. At each radial position the shear rate is matched to its shear stress to create a rheogram. As with most rheological measurements, the shear stress/shear rate data are modeled with a specific constitutive expression to determine rheological parameters, e.g., Herschel–Bulkley [56] parameters, or, alternatively, the shear viscosity versus shear rate is plotted.

For all studies, a small tank serves as a fluid reservoir that feeds a positive displacement pump. Depending on the circumstances, the fluid may be agitated in the tank to ensure homogeneity. If the fluid is evaluated at temperatures other than room temperature (20 ^{0}C) or if viscous heating is anticipated, the fluid is pumped through a coil heat exchanger to maintain a constant and known temperature. The fluid then flows at a constant and known flow rate into a section of nonmagnetic pipe that is centered in an MRI magnet/spectrometer. Studies have been performed using an Aspect Imaging 1 Tesla MRI spectrometer and industrially compatible permanent magnet (Aspect Imaging, Shoham, Israel). The magnet is designed to be compatible with process environments and has essentially zero external magnetic field. In other words, the magnetic field at the surface of the magnet is on the order of a few Gauss. The system has 30 G/cm peak gradient strength. Typically a solenoid radio-frequency coil imparts and receives radio-frequency energy. Velocity profiles are obtained noninvasively using a velocity-encoded pulsed gradient spin echo sequence (PGSE). Data can be acquired as fast as one image every 5 s. Typical measurement times are on the order of 1 min. In addition to the MR velocity image, an independent pressure drop is obtained over the straight length of pipe positioned in the magnet. A typical pipe diameter is 20 mm, though smaller and larger diameters have also been used. The pipe diameter is limited by the magnet construction. For this 1 Tesla Aspect unit, the maximum diameter (OD) is 59 mm. Alternate designs of the magnet can accommodate larger pipe diameters [57, 58].

Usually the fluid is recirculated, as shown in Figure 5.2. However, a number of studies have also been performed with fluids that have been single pass, which is important when evaluating shear-sensitive fluids. Image and data analyses are performed using MATLAB (MathWorks, Natick, MA, USA). GUI programs have been developed to analyze data and to communicate results. The data are reported in a form similar to that acquired from a standard research-grade laboratory rheometer (shear stress vs. shear rate).

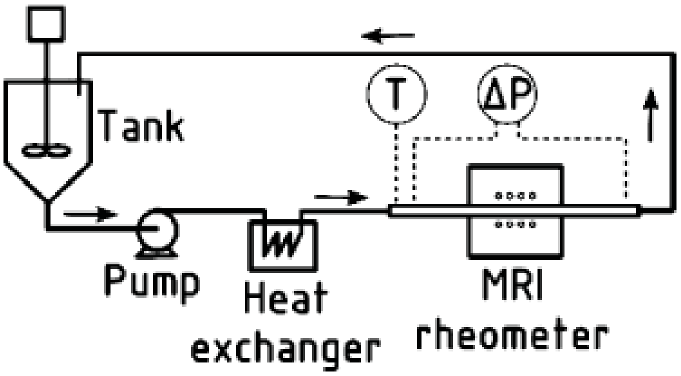

Figure 5.2 Flow loop for MRI rheometer studies

5.2. MRI Rheometry Acquisition and Processing

Figure 5.3 below shows a typical velocity profile acquired, in the software used. It is common window used in all data processings of MRI images. To get accurate rheological results, it is needed to adjust some important imaging parameters shown in Figure 5.4.

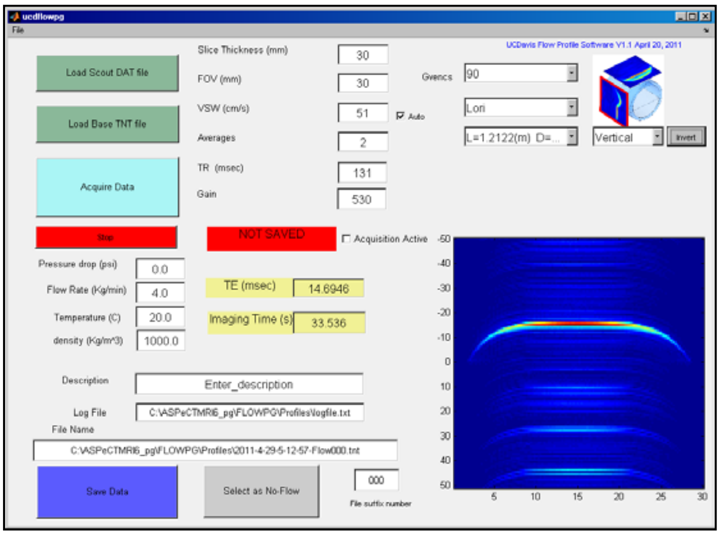

Figure 5.3 Acquisition program of MRI

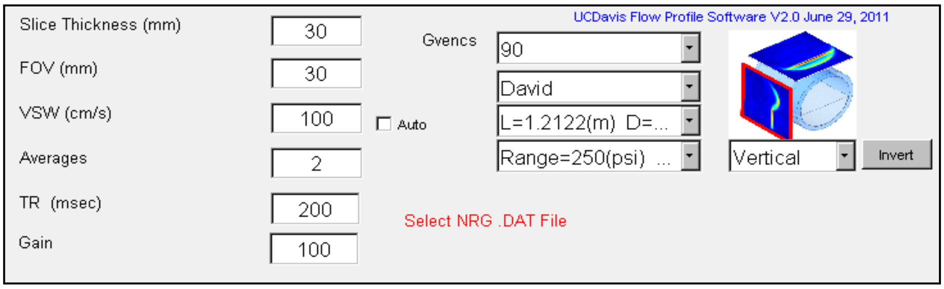

Figure 5.4 Imaging Parameters of MRI

In Figure 5.4, imaging parameters should be adjusted to capture steadily imaging files. Slice of thickness (mm) gives thickness of shell or slice of normal direction of flow. Thicker slice improves the signal intensity during imaging. Field of view (FOV) gives the thickness of vertical direction of flow approach to the signal. Larger values also improve the signal, but sometimes reduces radial resolution of image. Velocity Sweep Width (VSW) is adjusted with respect to velocity of flow and decides to the velocity resolution of image. It is critical parameter to capture velocity of flow accurately. Larger number of averages improves signal-to-noise ratio, increases imaging time. Repetition time (TR) and Gain are related signal intensity parameters. Larger TR can improve signal in some fluids increases imaging time and also gain increases signal to noise ratio of the image.

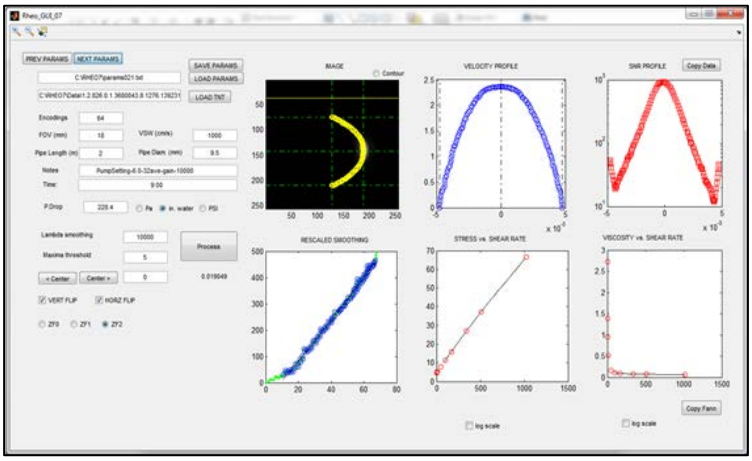

Figure 5.5 Processing program of MRI

An example for measured velocity profile is shown in Figure 5.5.. A first step is to compute the stress-rescaled velocity function process [58] using Equation (5.5) to Equation (5.8). Re-scaled smoothing method of velocity is applied to obtain rheological information from velocity experiments coupled with pressure drop measurement.

$$U(r) = (V_{\max} - V(r))\frac{\Delta P}{2L} \tag{5.5}$$

$$\tau(r) = \frac{\Delta P}{2L} r \tag{5.6}$$

$$U(\tau) = \int_0^{\tau} \dot{\gamma} d\tau \tag{5.7}$$

$$U'(\tau) = \dot{\gamma} \tag{5.8}$$

Next step is to compute an auxilliary function g;

$$g(\tau) = \frac{U(\tau)}{\tau} \tag{5.9}$$

A smoothed version of this function is almost a rheogram. This feature can be exploited to avoid artifacts that occur near the extremes of the rheogram if one tries to use other methods such as smoothing the velocity profile directly. We take the derivative of Equation (6.9) with respect to τ.

$$\frac{dg(\tau)}{d\tau} = g' = \frac{\tau U' - U}{\tau^2} \tag{5.10}$$

$$U' = \tau g' + \frac{U}{\tau} \tag{5.11}$$

Substitute Equation 5.8 and Equation 5.9 into Equation 5.10, Equation 5.12 yields;

$$\dot{\gamma} = \tau g' + \tau \tag{5.12}$$

The shear rate can be computed as in Equation 5.12. Smoothed shear stress v.s. shear rate data plot is given as seen in Figure 5.6.

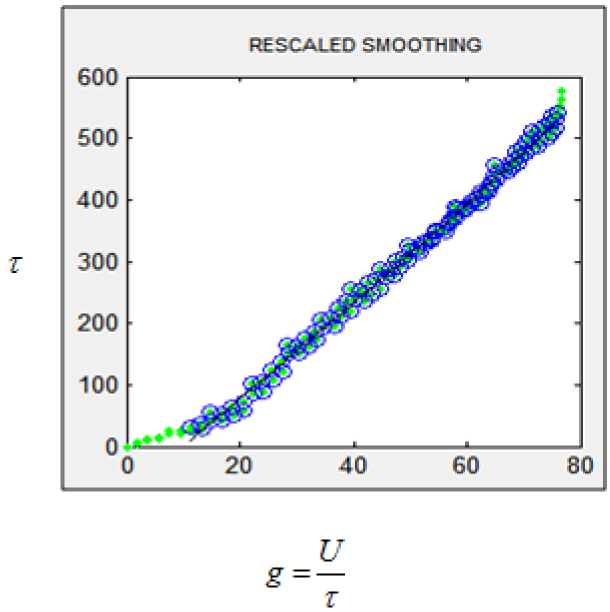

Figure 5.6 Rescaled Smoothing Process [51]

5.3. Results and Discussion

5.3.1. Rheological Parameter Evalutions of CMC Solutions

The CMC, with nominal molecular weight of 250,000 g/mol was supplied by Sigma. Aqueous solutions of CMC were prepared by dissolving the appropriate amount of CMC powder in distilled water. The high CMC concentration solutions (0.5%, 1.0%, 1.5%, 2% w/w.) were prepared by using water heated at 50 ^{o}C by gentle stirring with the sufficient time < 24 h.

Using flow loop depicted in Figure 5.7. MRI Flow Imaging Tests were done for 0.5, 1, 1.5, 2% (w/w) CMC solutions to determine rheological constitutive equations parameters. Inlet diamater of PVC tube was 38.1 mm. The test fluid was recirculated using Moyno pump (Integrated Motor Drive System, Franklin Electric) at 22^{o}C Pressure drop was obtained at the ends of pipe with a constant length of 1.68 m using pressure transducer (Siemens Company).

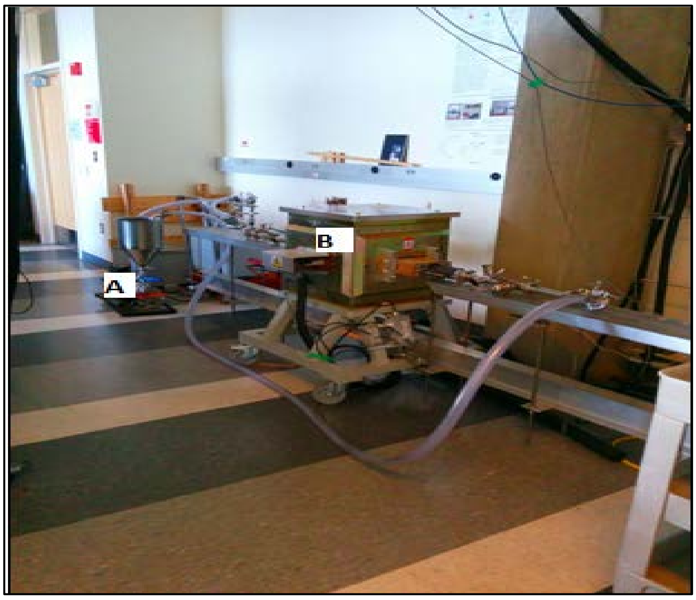

Figure 5.7 Flow loop setup for CMC testing A) Positive displacement pump B) MRI magnet

In Figure 5.8 flow image for an example of 0.5% CMC flow, can be seen with data processing window. The velocity profile is used to obtain shear rate distribution, while the pressure drop is used to calculate the shear stress distribution. By taking the ratio of these quantities at a radial position, local viscosity can be obtained within the shear rate range in the flow, zero at the center, and maximum at the wall, within minutes.

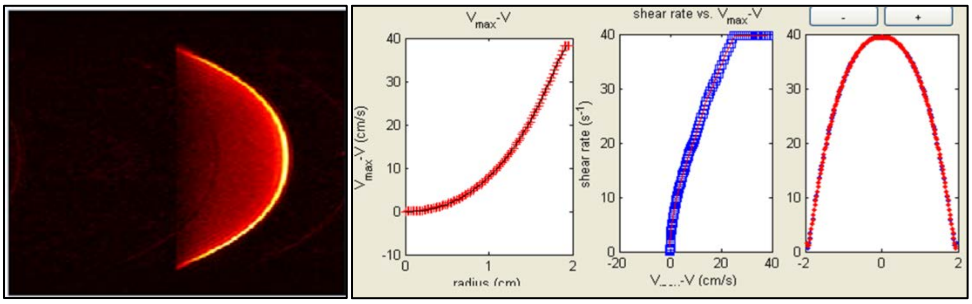

Figure 5.8 MRI Image for 0.5% CMC

Figure 5.9 shows the flow curves of the CMC solutions at different concentrations. Instrument CVO rheometer (Bohlin Insturements) with a cone and plate rheometer (with a cone angle 4^o and diameter 40 mm) at 22^oC was used for offline measurement. A steady state shear rate ramp from 0.085 to10 s^{-1} was performed in logarithmic mode with 10 points/ decade. For MRI measurements at the different pump speed of flow loop and also measured using a conventional technique and the agreement between the results is satisfactory shown in Figure 5.9.

MRI measurement results of CMC solutions are also listed in Table 5.1 with changing pump speed of flow loop shown in Figure 5.7. All obtained rheograms for different CMC solutions are listed in Table 5.1. Rheological properties are independent of flow velocity. Hence, zero shear viscosities are nearly constant during the flow. As Reynolds number and concentration of flow increased, fluid shear stress acting on the pipe wall also increased as seen in Table 5.1.

Rheological parameters for CMC solutions are listed in Table 5.2. Depending on CMC concentration, Power law or H.Bulkley models give the best fit according to MRI flow result. Power Law model is valid for 0.5% and 1.0% CMC. On the other hand, 1.5% and 2.0% CMC solutions flow are well described by Herschel–Bulkley model.

Consistency index, K, and power law index, n, and yield stress, τ_0, data values are obtained from shear stress v.s. shear rate data using online (MRI Rheometry) method and offline (CVO Rheometry) method. R^2 values of the fittings are also satisfactory. As CMC concentration increased, yield stress gets larger. These results are also in good agremeent with those reported by Benchabane et. al [59].

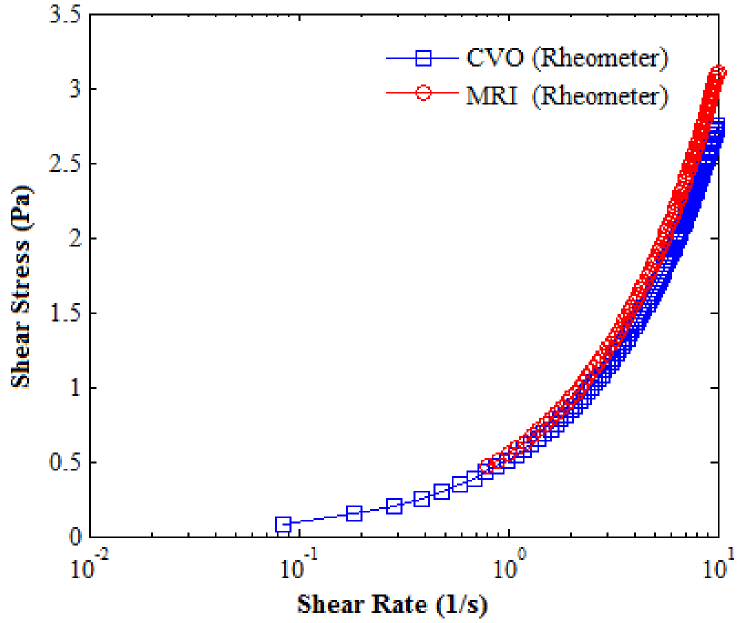

(a)

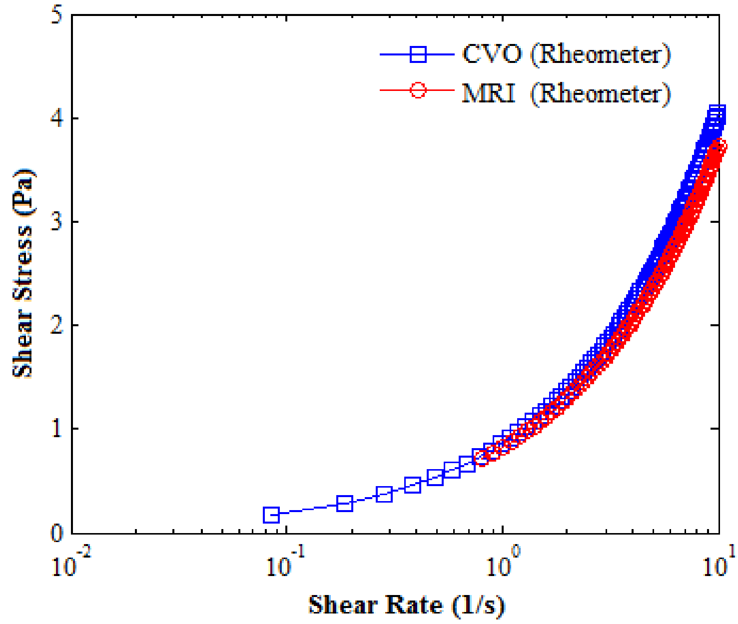

(b)

Figure 5.9 Shear stress v.s. Shear rate plot for (a) 0.5% CMC (b) 1.0% CMC (c) 1.5% CMC (d) 2.0% CMC.

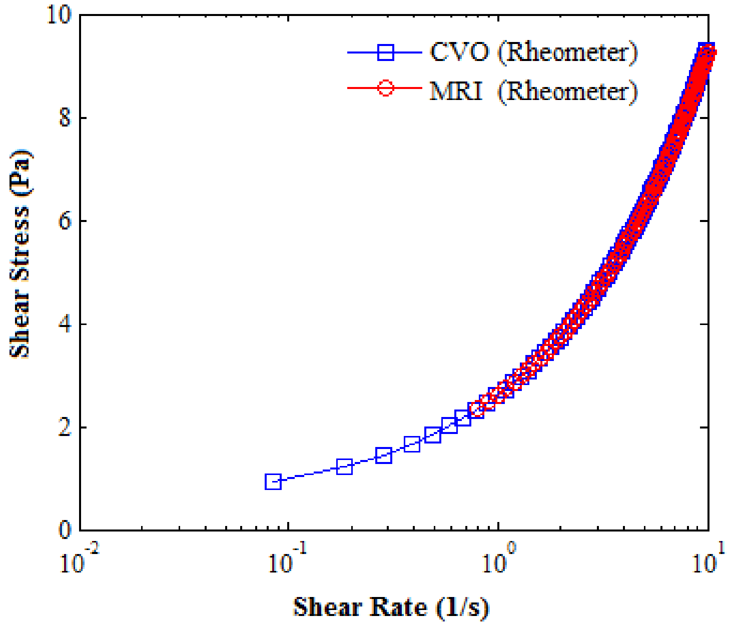

(c)

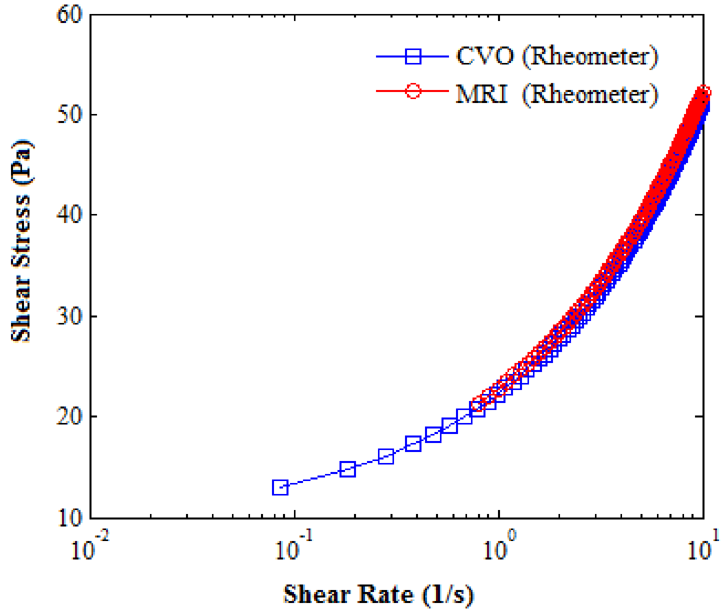

(d)

Figure 5.9 Shear stress v.s. Shear rate plot for (a) 0.5% CMC (b) 1.0% CMC (c) 1.5% CMC (d) 2.0% CMC (continued).

Table 5.1 MRI flow measurement for CMC solutions

	Pump Speed (rpm)	V(m/s)	*Re*	Wall stress (Pa)	Zero Shear Viscosity (Pa.s)
0.5%CMC	330	0.023	2.176	4.371	0.412
	400	0.039	4.020	4.840	0.411
	700	0.078	8.840	7.590	0.411
	1000	0.121	14.445	11.730	0.413
	1500	0.196	25.013	15.240	0.415
1.0%CMC	330	0.032	1.620	7.230	1.002
	430	0.043	2.312	9.350	1.003
	600	0.060	3.390	12.780	1.001
	1000	0.122	7.870	20.670	1.002
	1500	0.193	13.590	28.605	1.001
1.5%CMC	330	0.035	0.970	16.800	2.001
	460	0.047	1.400	21.560	1.989
	600	0.058	1.850	27.770	2.012
	1000	0.094	3.300	42.540	2.014
	1500	0.183	7.690	55.550	2.001
2.0%CMC	330	0.031	0.180	53.681	9.012
	500	0.053	0.360	77.670	9.022
	800	0.077	0.580	95.431	8.912
	1000	0.095	0.760	106.071	8.993
	1500	0.147	1.340	127.350	8.912

Table 5.2 Rheological Parameters for CMC solutions

	MRI Rheometer	CVO Rheometer	Goodness of the fit R^2 (MRI- CVO)
0.5%CMC	K=0.550 n=0.753	K=0.512 n=0.730	0.9993-0.9987
1.0%CMC	K=0.825 n=0.653	K=0.863 n=0.670	0.9983-0.9985
1.5%CMC	τ_0=0.436 K=2.176 n= 0.607	τ_0=0.424 K=2.640 n=0.608	0.9994-0.9996
2.0%CMC	τ_0=9.054 K=14.731 n=0.495	τ_0=9.150 K=13.120 n=0.507	0.9986-0.9991

5.3.2. Low Shear Rate Flow Rheology study on Carbopol Solutions

An analysis of complex (yielding) rheological flow behavior of 0.1, 0.13, 0.15 wt % Carbopol solutions has been carried out using MRI velocimetry within the low shear rate region (10^{-4} -10 s^{-1}) for gravity driven flow system. For this study, flow kinematics in a pipe was performed at the steady and creeping conditions (Re<1) to get accurate dynamic yield value of Carbopol solutions. Then we show that in this range of shear rates, MRI velocimetry works well with using the suitable image data acquisition process. (Re-scaled smoothing method of velocity)

The shear viscosity of Newtonian and Generalized Newtonian flow can be monitored by MRI based viscometry techniques. Velocity profile imaging can be extracted with the known of pressure drop and pipe dimensions of entire flow using MRI techniques. Conversion of velocity profiles into rheological data is only based on computing relation between shear rates and shear stress data processing during on-line flows [54]. It can be applied various geometry flow analysis for rheological characterization with some experimental limitation of resolution or quality of velocity data. Accuracy of MRI velocity data implementation is given by Arola et. al [53].

Zero shear rate or creeping flow rheology has crucial potential for measuring of yield stress of complex fluid. Conventional yield stress measurement methods sometimes fail due to accuracy of torque measurement. From a practical point of view, yield stress concept has a significant relationship to consumer perception of product quality.

In this study, Carbopol, known as a complex fluid flow [60] due to physical structure during pipe flow, low shear rate rheology is investigated by measuring the steady fluid velocity profile using MRI.

Cross-linked polyacrylate polymer (Carbopol940, Lubrizol Corporation) was used at different concentrations (0.1%, 0.13%, 0.15% w/w). These solutions were prepared using powder form of Carbopol-940 mixed with distilled water in a stirred tank for approximately 7 days. The polymer solutions were neutralized with TEA (tri ethanolamine) solution to *p*H 7.1. The neutralization process is crucial because of the strong dependence of the flow behavior of Carbopol solutions on *p*H. The neutralization allows the solution to achieve its maximum viscosity since the polymer chains disentangle at this *p*H [61].

The closed flow loop system is used in this study supplies gravity driven flow serving low velocity measurement for MRI imaging. The flow loop is shown schematically in Figure 5.10. The test fluid is recirculated using a Moyno pump (Integrated Motor Drive System, Franklin Electric) through a pipe with an internal diameter of 38.1 mm made of PVC pipe connected with stainless steel fitting parts. Pressure drop was obtained at the ends of pipe with a constant length of 1.68 m using pressure transducer (Siemens Company). To ensure fully developed flow in the imaging part of pipe 4.5 m with straight fittings upstream of magnet (between exiting of pump and entrance of pipe section) (L/d=120). Flow driven tank height is changed to between 50-150 cm using a lab cart with an adjustable height platform.

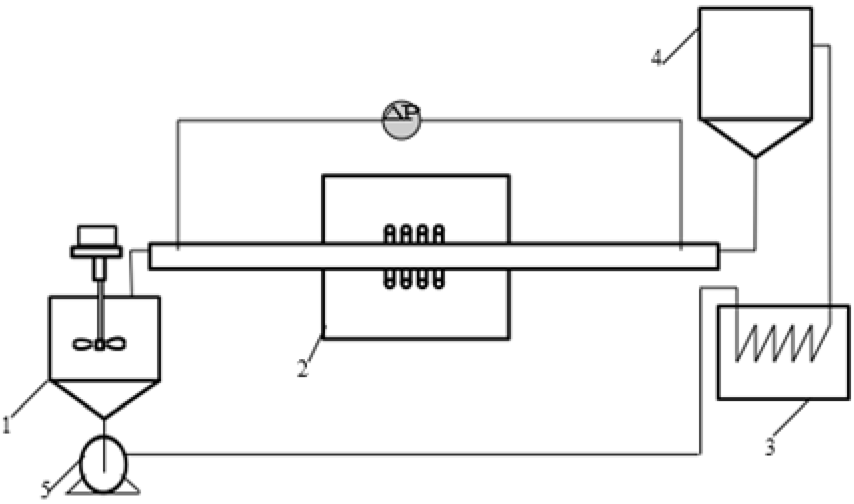

Figure 5.10 Components of the flow system: 1. Storage tank, 2. Imaging magnet 3.Temperature bath 4. Flow driven tank, 5. Moyno pump (positive displacement pump)

Velocity and rheological measurements were carried out using MRI under pulsed gradient spin echo sequence (PGSE) [50] on an Aspect Imaging 1 Tesla permanent magnet (Aspect Imaging, Shoham, Israel). The slice of thickness and field of view were 30 mm and 50 mm respectively. The radial and velocity encodings used 256 steps. Small velocity sweep width values (VSW) to capture accurate low velocity flow imaging through the pipe are used depicted as in Table 5.3. The radio frequency of coil was a solenoid with four turns, encasing a cylindrical volume 60 mm in diameter and 60 mm long. System temperature is kept constant at 22.2 ^{o}C using temperature controller and heat exchanger. Steady state shear flow experiment parameters is used shown in Table 5.3. The Reynolds number is smaller than unity.

Table 5.3 Some typical example of experimental parameters used in imaging process

Carbopol Conc.(%)	VSW (cm/s)	Q (l/min)	*Re*
0.10	9	1.235	0.370
0.13	6	0.864	0.020
0.15	5	0.746	0.015

Measured velocity MRI images for 0.15% Carbopol solutions for no- flow and axial velocity flow condition are given in Figure 5.11 and Figure 5.12, respectively. MRI no- flow condition is acquired prior to initiating flow and also has same signal for 0.1 and 0.13% Carbopol solutions. The signal intensity depicts the axial velocity as a function of radial position. The vertical bright region in the center of no-flow image spans the width of the pipe which indicates the position of pipe walls. The bright region position in the center of the image is for axial velocity, v=0, at no-flow condition.

Under the flow condition for 0.15% Carbopol velocity profiles are shown in Figure 5.12. As the flow rate is increased, the signal intensity is positioned more to the right as expected with higher velocities. At low flow rate, 0.25 l/min, the image exhibits a more blunted velocity profile for VSW value at 5 cm/s. It is sufficient to capture small shear rate ranges for the flow.

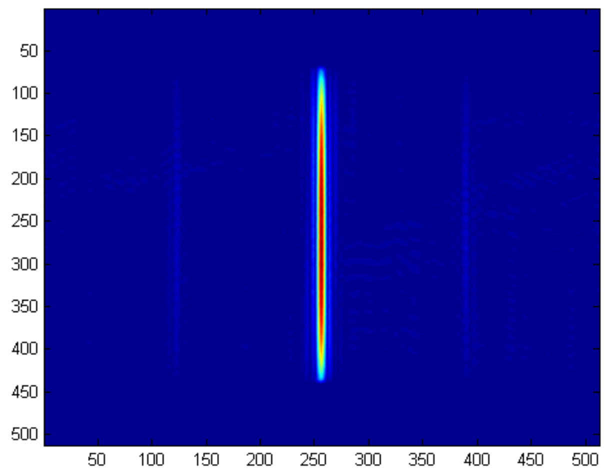

Figure 5.11 No flow condition of solutions (no wall slip).

Measured velocity profile images are given for % 0.15 Carbopol solution at different volumetric flow rates and are shown in Figures 5.12. Plug like shape velocity profile expands as volumetric flow rate is increased. Carbopol solutions do not exhibit slip velocity at these low Reynolds numbers as seen in Figures 5.12.

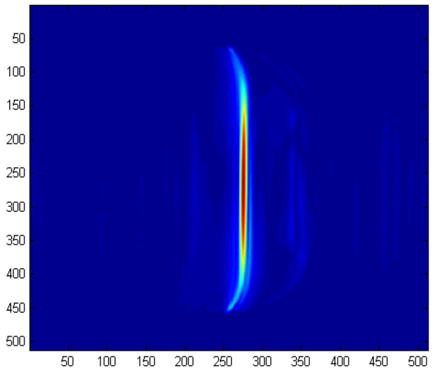

(a)

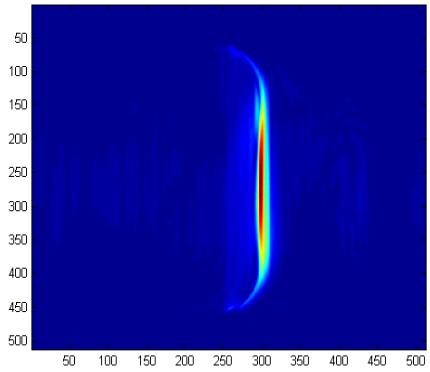

(b)

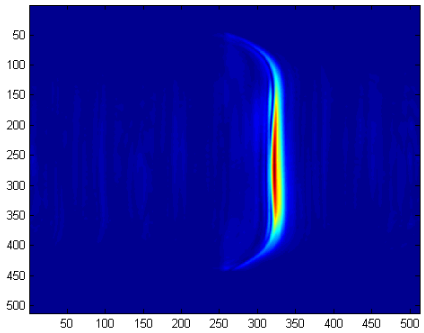

(c)

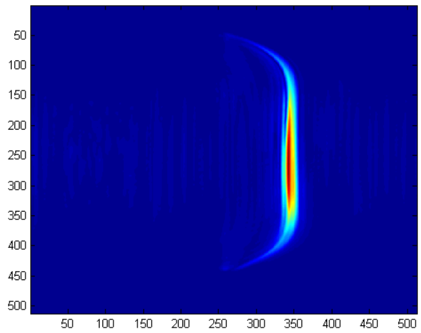

(d)

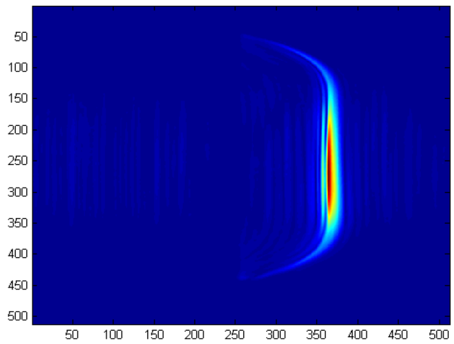

(e)

Figure 5.12 Measured Velocity Profile 0.15% Carbopol Solutions with different flow rates (a) 0.25 l/min (b) 0.5 l/min (c) 0.75 l/min (d) 1.0 l/min (e)1.5 l/min.

Figure 5.13 shows the velocity profiles for Carbopol solutions with no-slip at wall. They are given as function of pipe radius. The flow is unidirectional flow and velocity field is simply given by V=V(r) for different pressure drop measurements. Velocity magnitude is even small as order of 10^{-2} and 10^{-3} m/s and sufficient to observe low shear rate flow measurement. Velocity data exhibits apparent plug-like behavior. The minimum shear rate data point is determined at the lowest rate investigated shown in Figure 5.13.

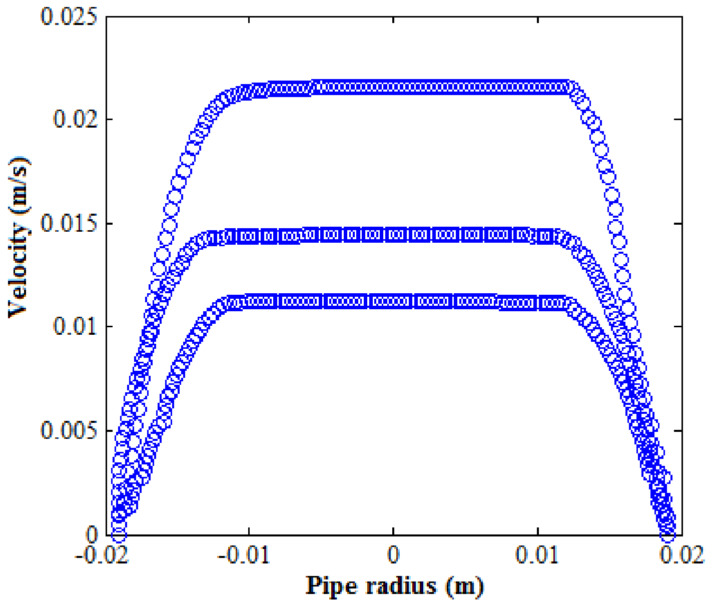

(a)

Figure 5.13 Velocity profiles for Carbopol solutions:(a) 0.1%(b) 0.13%(c) 0.15%.

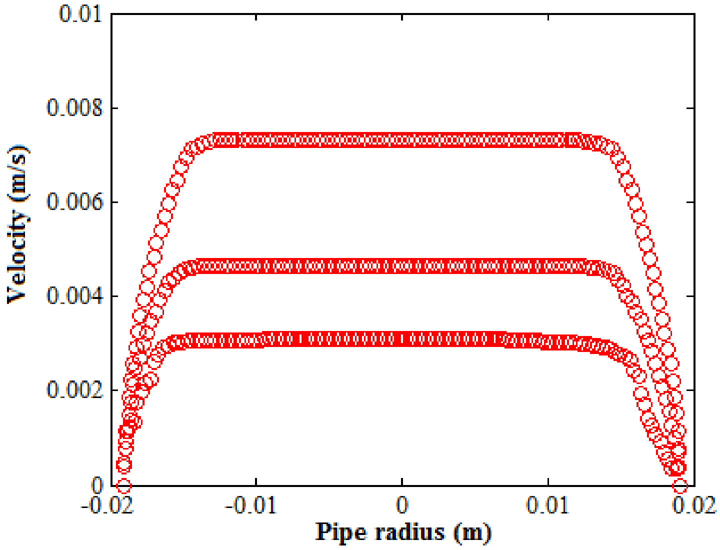

(b)

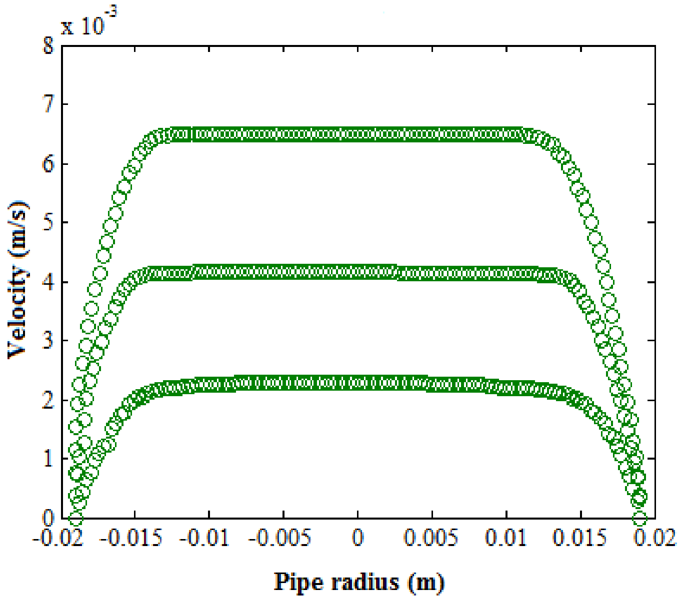

(c)

Figure 5.13 Velocity profiles for Carbopol solutions: (a) 0.1% (b) 0.13% (c) 0.15% (continued).

In Figure 5.14, rheograms were given for three different Carbopol concentrations determined using in- line and off-line methods. The square symbol lines represent the values obtained with the off-line conventional rheometer. The circles correspond to MRI velocimetry data. For conventional methods, shear rates start from 0.085s^{-1}. MRI velocimetry data match closely with the off-line data for all concentrations. Instrument CVO rheometer (Bohlin Insturements) with a cone and plate rheometer (with a cone angle 4^o and diameter 40 mm) at 22 ^oC was used for offline measurement. A steady state shear rate ramp from 0.085 to10 s^{-1} was performed in logarithmic mode with 10 points/decade. Many rheological measurements at different flow rate conditions shear stress/shear rate data is obtained as shown in Figure 5.13. The lower shear rate is limited by the velocity resolution of flow image because no data are acquired on shear rates below the minimum calculated velocity resolution for the MRI method (see Figures 5.9).

For this study the minimum shear rate range is on the order of 10^{-4} s^{-1} for VSW=5 shown in Table 5.13. It must be consistent with measured experimental shear rate data to estimate of the quality of shear stress and shear rate data. The minimum shear rate can be calculated using the relationship between nondimensionalized minimum shear rate and resolution of velocity data [53]. The results are obtained using rescaled smoothing process pre-described by Tozzi et.al [57]. This rescaling feature also helps to eliminate artifacts that can occur in the velocity profiles during data acquisition process performed using MATLAB. It removes potential sources of error which can be resulted from image acquisition. Accurate dynamic yield values estimates can be obtained from this process and are shown in Figure 5.14. Lower yield stress is achieved for lower concentration of Carbopol as expected. From the data in Figure 5.14, yield stress (τ_0) can be found as 9.8, 22.8, 58.4 Pa which correspond to the intersection of shear stress value when approaching shear rate is nearly zero.

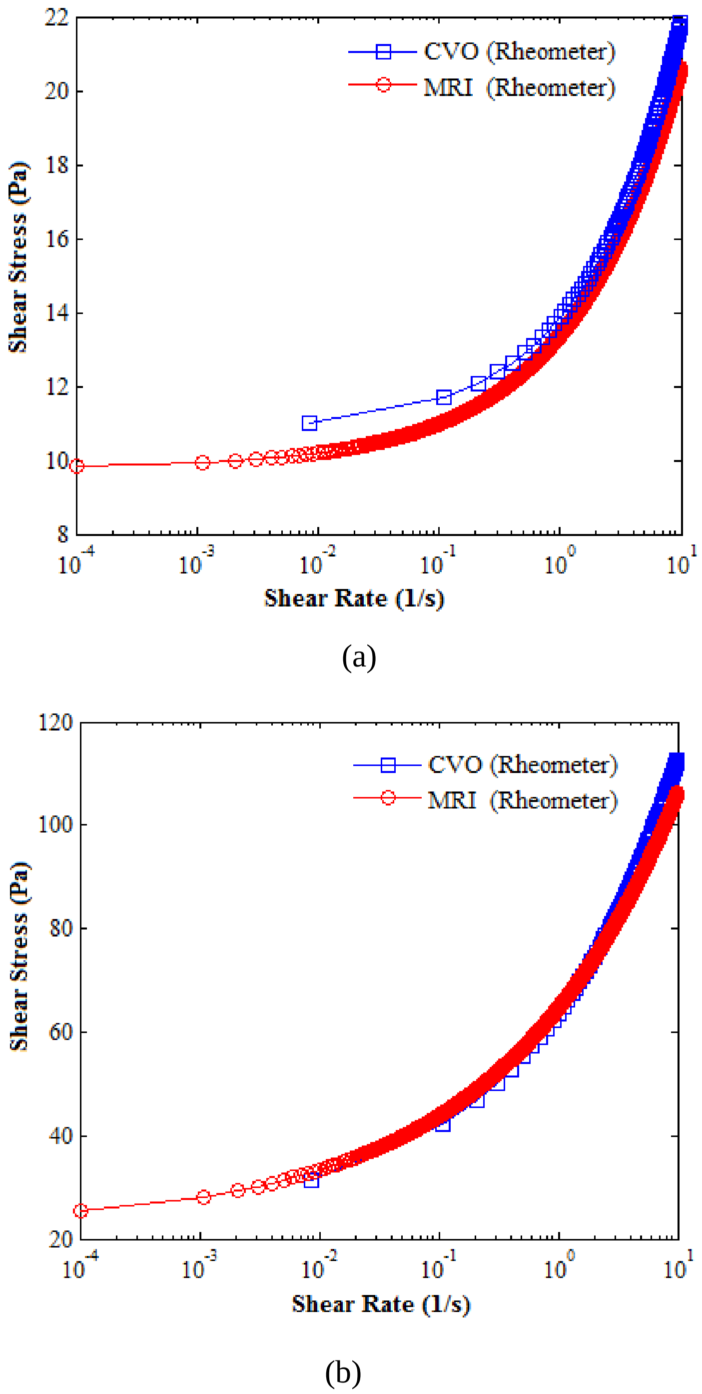

Figure 5.14 Rheograms for Carbopol solutions (a) 0.1% (b) 0.13% (c) 0.15%.

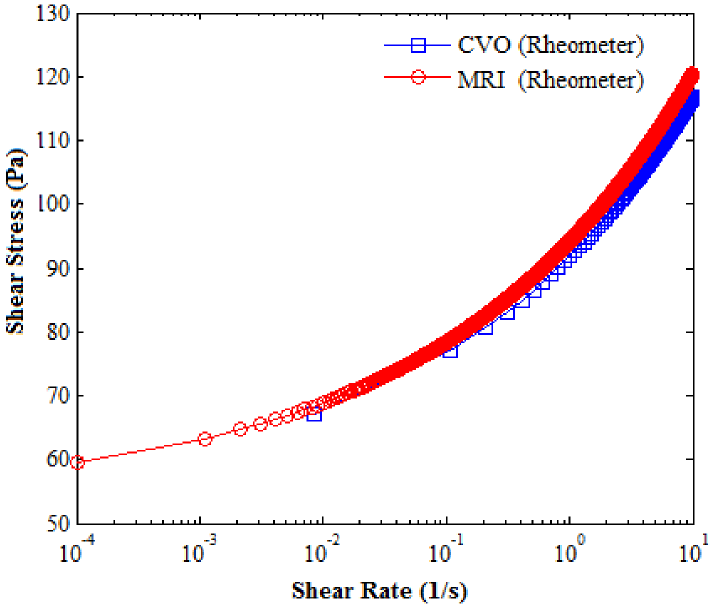

(c)

Figure 5.14 Rheograms for Carbopol solutions (a) 0.1% (b) 0.13% (c) 0.15% (continued).

CHAPTER 6

CONCLUSIONS

6.1. Conclusions

In this study numerical and experimental studies are carried out for steady laminar flows of both Newtonian and non-Newtonian fluids around the confined square cylinder to reach physical mechanism of flow behavior around the square obstacle. Oldroyd-B model (constant viscosity with elasticity) and the PTT model (shear thinning with elasticity) are used to capture viscoelasticity. Flows are simulated at various Reynolds and Weissenberg numbers by utilizing the finite volume method on non-uniform staggered grid systems. Upwind and CUBISTA approximations are employed for the viscoelastic stress and convective terms in the momentum equations to get accurate numerical solutions. Particle image velocimetry (PIV) was also used to obtain the two-dimensional velocity field. The Newtonian flow measurements were conducted for $Re=1\leq Re\leq 100$. Finally MRI was employed for rheological characterization of viscoelastic fluids. The results obtained in this study allow one to draw the following conclusions**:**

1. Symmetrical vortex structure are found to be higher with an increase in the Reynolds number for Newtonian flow around the obstacle at $Re>20$. Highest intensity of vorticity is obtained in the normal direction to the flow. Symmetrical vortex structures at the wake region is observed when *Re* increased. Numerical simulations is confirmed by the experimental visualization method, PIV. The effect of inertia on vorticity distribution

around the obstacle is analyzed and the results getting of two methods show that increasing the Reynolds number leads to increase of vortex area and intensity.

2. The impact of *Re* number on *Cd* becomes more pronounced at low *Re* region. As inertial effects increase, the contributions of the viscous effect and pressure effect to the total drag coefficient decrease for Newtonian flow.

3. Results for mesh refinement along y-direction in the system, with shrinking length scales in the velocity gradients, the impact of mesh size on computational results was considered negligibly small for the dense mesh of 372x162. Convergence of CUBISTA scheme is nearly independent to get convergence solution. CUBISTA scheme also prevents numerical instabilities at high *We* flows. At creeping flow condition maximum attainable Weissenberg number is 15 for both model.

4. Increasing fluid elasticity or inertia leads to larger recirculation lengths and eventually formation of symmetric vortexes.

5. Strong impact of *Re* on the highest attainable *We* was observed for stable computations. At higher value of *Re,* upper limit of *We* should be reduced to get stable solutions for PTT and Oldroyd-B model.

6. A detail examination of velocity profiles around the obstacle of PTT and Oldroyd-B flow reveal that streamwise velocity at high *We* flow delays recover undisturbed bulk velocity in the wake region for both flow at constant *Re* number. On the other hand, for PTT flow, required length to achieve the fully developed is nearly same for Newtonian flow at all *We*. But for Oldroyd-B flow with increased of *We* , elasticity of fluid leads to increase required length to achive the fully developed region in the wake compared to Newtonian flow.

7. With respect to vertical velocity changing around the obstacle for the flow of PTT, more symmetric distribution profile around obstacle is observed. With low elasticity flow, more raising vertical velocity is appeared. However, Oldroyd-B flow has overshoot and undershoot peaks especially at *We*=3. Absolute magnitude of vertical velocity component range is also higher than PTT.

8. For viscoelastic flow case, pressure gradients are generated by dominancy of elasticity of flow in near front and rear stagnation point of the cylinder. Therefore, viscoelastic pressure drop values are also higher than Newtonian flow case due to increasing effect of longitudinal flow. Larger *We* attenuates the extensional viscosity and pressure for PTT flow. However, at *Re*=20, pressure drop gets amplified due to more breaking the fore-aft symmetry of flow around obstacle at higher *We* for Oldroyd-B flow. The pressure drop for PTT fluid is smaller than that of Oldroyd-B fluid owing to low stresses because of shear-thinning effects at high *We*.

9. Higher *We* and higher *Re* are the stronger shear thinning effects that lead to the lower shear stress values as for PTT flow. An opposed to the PTT fluid flow, for Oldroyd-B flow absolute magnitude of shear stresses especially at the vicinity of obstacle (singularity point) increases compared to PTT in the flow field with increasing *We* and *Re*. However, shear stress relaxation is more quickly than PTT in the wake region.

10. Another important feature is the response of normal stress behavior along the obstacle surface. Normal stress relaxation occurs between obstacle surface and the channel wall. PTT fluid delays normal stress momentum transfer from obstacle surface to the channel wall. As the deformation rate is raisen, shear viscosity decreases approaching to the channel wall and normal stress loss is observed. For Oldroyd-B model, all elastic or normal stresses are

nearly recovered and absorbed by the channel wall. It relaxes quickly elastic stresses compared as PTT model.

11. Normal stress contours extend longer distances in the wake region as *We* is increased for both model. This is an expected result since higher relaxation times lead to longer convection distances of the stresses.

12. Low *We* and high *Re* conditions favor formation of negative normal stresses in the flow regions with Hoop stresses for both model. However, For Oldroyd-B model, positive hoop stresses are also observed in the wake region at high *We* and *Re* conditions.

13. Shear stresses are mainly observed in the region dominated by the flow tangential to the solid boundaries and that shear stresses get amplified at high *Re*. Flow is more stabilized due to relaxing of shear stresses for both model.

14. Viscoelastic wake behind the square obstacle is longer than the Newtonian wake. This also supplies larger drag or drag enhancement in viscoelastic medium compared with Newtonian results.

15. There is no single increasing or decreasing trend in *Cd* with respect to changes in We for PTT model. Up to a certain critical *We* value, that appears to be between 0 and 1, *Cd* gets elevated with increasing *We* due to the normal stresses. With further increase in *We*, *Cd* values get smaller due to stronger shear thinning effects. At a constant *We*, a reduction in *Cd* is observed when the value of *Re* is changed from 5 to 20 similar to Newtonian fluid case. Decreasing intensities of the vorticity in the wake region with respect to both *We* and *Re* are another indication of the smaller drag coefficient.

16. When *We* increases, shear and normal stresses contributions to drag coefficient changes little owing to fluid constant viscosity at constant *Re* for

Oldroyd-B. Furthermore, *Cd* continues slightly to enhance with increased *We* for the high *Re*. For *We*<3, negative normal stress field around the obstacle has also decreasing effect in magnitude of normal stress contribution to drag coefficient.

17. At *Re*=20, the variation of *Cd* with increased *wr* is nearly same for the range of *We* for both model. At high *We* flows, further increase of polymer concentration makes no significant contribution to *Cd* around the obstacle.

18. As CMC and Carbopol concentration increased, yield stress gets larger.

19. MRI flow imaging at low Reynolds number are readily obtained from the gravity driven experimental flow design.

20. MRI velocimetry is an effective tool for obtaining accurate yield stress data for Carbopol solutions at low shear rate ranges.

21. Carbopol solutions did not exhibit slip velocity at these low Reynolds numbers.

6.2. Recommendations for Future Work

Although in this study a complete modeling procedure for viscoelastic flow around the confined cylinder presented, there are several aspects that need to be investigated further.

Firstly, experimental measurements on viscoelastic flow around the cylinder can be done using PIV system to see elastic effects of flow. Therefore, PIV system should be re-scaled to compare numerical results quantitatively. Furthermore, PIV system should be improved to get rheological information of flow field by combined with pressure drop measurements.

Secondly, modeling of flow over multiple obstacles (two or three) can be implemented into code. The flow patterns and wake structures for the case flow over square cylinders are considerably different from flow over one cylinder. Because, vortex behavior around between obstacles affects drag coefficient characteristics of flow. Such a further study is considerable fundamental interest because of the fact that the wakes of multiple bluff bodies placed next to each others create a complex flow structure. The understanding of this flow pattern as well as its exact mathematical modeling and numerical simulation is a challenging task.

REFERENCES

1. Zdravkovich, M. M. *Flow around circular cylinders*. (1997).Volume 1: Fundamentals Oxford University Press.

2. Nitin, S. & Chhabra, R. P. Non-isothermal flow of a power law fluid past a rectangular obstacle (of aspect ratio 1x2) in a channel: Drag and heat transfer. *Int. J. Eng. Sci.* **43,** 707–720 (2005).

3. Mittal, S. & Raghuvanshi, A. Control of vortex shedding behind circular cylinder for flows at low Reynolds numbers. *Int. J. Numer. Methods Fluids* **35,** 421–447 (2001).

4. Goldstein, S. On laminar boundary-layer flow near a position of separation. *Q. J. Mech. Appl. Math.* **1,** 43–69 (1948).

5. Sharma, A. & Eswaran, V. Effect of channel-confinement and aiding/opposing buoyancy on the two-dimensional laminar flow and heat transfer across a square cylinder. *Int. J. Heat Mass Transf.* **48,** 5310–5322 (2005).

6. Sohankar, A. Flow over a bluff body from moderate to high Reynolds numbers using large eddy simulation. *Comput. Fluids* **35,** 1154–1168 (2006).

7. Breuer, M., Bernsdorf, J., Zeiser, T. & Durst, F. Accurate computations of the laminar flow past a square cylinder based on two different methods: lattice-Boltzmann and finite-volume. *Int. J. Heat Fluid Flow* **21,** 186–196 (2000).

8. Sen, S., Mittal S. & Biswas G. Flow past a square cylinder at low Reynolds numbers. *Int. J. Numer. Meth. Fluids* **67,** 1160–1174 (2011).

9. Saha, A. K., Biswas, G. & Muralidhar, K. Three-dimensional study of flow past a square cylinder at low Reynolds numbers. *Int. J. Heat Fluid Flow* **24,** 54–66 (2003).

10. Dhiman, A. K., Chhabra, R. P. & Eswaran, V. Steady Flow of Power-law Fluids Across a Square Cylinder. *Chem. Eng. Res. Des.* **84,** 300–310 (2006).

11. Dhiman, a. K., Chhabra, R. P. & Eswaran, V. Steady flow across a confined square cylinder: Effects of power-law index and blockage ratio. *J. Nonnewton. Fluid Mech.* **148,** 141–150 (2008).

12. Paliwal, B., Sharma, A., Chhabra, R. P. & Eswaran, V. Power law fluid flow past a square cylinder: momentum and heat transfer characteristics. *Chem. Eng. Sci.* **58,** 5315–5329 (2003).

13. Koteswara Rao, P., Sahu, A. K. & Chhabra, R. P. Momentum and heat transfer from a square cylinder in power-law fluids. *Int. J. Heat Mass Transf.* **54,** 390–403 (2011).

14. Ehsan I., Mohammed S., Mohammed N. & Ali J. Laminar and turbulent power law fluid flow passing a square cylinder. *Int. J. Phys. Sci.* **7,** 988–1000 (2012).

15. Nirmalkar, N., Chhabra, R. P. & Poole, R. J. On creeping flow of a Bingham plastic fluid past a square cylinder. *J. Nonnewton. Fluid Mech.* **171-172,** 17–30 (2012).

16. Boger, D. V. Viscoelastic fluid mechanics: Interaction between prediction and experiment. *Exp. Therm. Fluid Sci.* **12,** 234–243 (1996).

17. Li, X.-B., Li, F.-C., Cai, W.-H., Zhang, H.-N. & Yang, J.-C. Very-low-Re chaotic motions of viscoelastic fluid and its unique applications in microfluidic devices: A review. *Exp. Therm. Fluid Sci.* **39,** 1–16 (2012).

18. Yip, R. Slow Flow of Viscoelastic Fluids through Fibrous Porous Media. (2011)

19. Nadau, L. & Sequeira, A. Numerical simulations of shear dependent viscoelastic flows with a combined finite element–finite volume method. *Comput. Math. with Appl.* **53,** 547–568 (2007).

20. Bird, R. B., Armstrong, R. C. & Hassager, O. *Dynamics of polymeric liquids. Vol. 1, 2nd Ed.: Fluid mechanics*. *Related Information: Fluid Mechanics. Dynamics of Polymeric Liquids. Volume 1. 2nd Edition* (1987).

21. Thien, N. P. A Nonlinear Network Viscoelastic Model. *J. Rheol.* **22,** 259 (1978).

22. Davies, A. R. & Devlin, J. On corner flows of Oldroyd-B fluids. *J. Nonnewton. Fluid Mech.* **50,** 173–191 (1993).

23. Thien, N. P. & Tanner, R. I. A new constitutive equation derived from network theory. *J. Nonnewton. Fluid Mech.* **2,** 353–365 (1977).

24. Khan, S. A. & Larson, R. G. Comparison of Simple Constitutive Equations for Polymer Melts in Shear and Biaxial and Uniaxial Extensions. *J. Rheol. (N. Y. N. Y).* **31,** 207–234 (1987).

25. Tanner, R. I. & Rivlin, R. S. *Engineering Rheology*. *Journal of Applied Mechanics* **54,** (1987).

26. H.K. Versteeg and W. Malalasekera, An introduction to computational fluid dynamics: The finite volume method, Prentice Hall, 1995.

27. Perić, M., Kessler, R. & Scheuerer, G. Comparison of finite-volume numerical methods with staggered and colocated grids. *Comput. Fluids* **16,** 389–403 (1988).

28. Alves, M. A., Oliveira, P. J. & Pinho, F. T. A convergent and universally bounded interpolation scheme for the treatment of advection. *Int. J. Numer. Methods Fluids* **41,** 47–75 (2003).

29. Yapici, K. & Uludag, Y. Computational analysis of hydrodynamics of shear-thinning viscoelastic fluids in a square lid-driven cavity flow. *Korea-Australia Rheol. J.* **25,** 243–260 (2013).

30. Rubin, S. & Khosla, P. Polynomial interpolation methods for viscous flow calculations. *J. Comput. Phys.* **24,** 217–244 (1977).

31. Leer, B. Van. On numerical dispersion by upwind differencing. *Appl. Numer. Math.* **2,** 379–384 (1986).

32. Patankar, S.V. & Spalding, D.B., A calculation procedure for heat, mass and momentum transfer in three-dimensional parabolic flows, *Int. J. Heat Mass Transf*, **15,** 1787(1972).

33. Yapici, K. A comparison study on high-order bounded schemes: Flow of PTT-linear fluid in a lid-driven square cavity. *Korea-Australia Rheol. J.* **24,** 11–21 (2012).

34. Gupta, A. K., Sharma, A., Chhabra, R. P. & Eswaran, V. Two-Dimensional Steady Flow of a Power-Law Fluid Past a Square Cylinder in a Plane Channel: Momentum and Heat-Transfer Characteristics. *Ind. Eng. Chem. Res.* **42,** 5674–5686 (2003).

35. Sharma, A. & Eswaran, V. Effect of Channel Confinement on the Two-Dimensional Laminar Flow and Heat Transfer Across a Square Cylinder. *Numer. Heat Transf. Part A Appl.* **47,** 79–107 (2004).

36. Keane, R. D. & Adrian, R. J. Theory of cross-correlation analysis of PIV images. *Appl. Sci. Res.* **49,** 191–215 (1992).

37. Okajima, A., Ueno, H. & Sakai, H. Numerical-Simulation of Laminar and Turbulent Flows around Rectangular Cylinders. *Int. J. Numer. Methods Fluids* **15,** 999–1012 (1992).

38. Van Oudheusden, B. W., Scarano, F., Van Hinsberg, N. P. & Watt, D. W. Phase-resolved characterization of vortex shedding in the near wake of a square-section cylinder at incidence. *Exp. Fluids* **39,** 86–98 (2005).

39. Berrone, S. & Marro, M. Space-Time adaptive simulations for unsteady Navier-Stokes problems. (2008).

40. Zandbergen, P. Von Karman Swirling Flows. *Annu. Rev. Fluid Mech.* **19,** 465–491 (1987).

41. Hu., H.H., and Joseph D.D., Numerical simulations of viscoelastic flow past a cylinder., *J. Nonnewton. Fluid Mech.* **37,** 347-371 (1990).

42. Huang, P. & Feng, J. Wall effects on the flow of viscoelastic fluids around a circular cylinder. *J. Nonnewton. Fluid Mech.* **60,** 179–198 (1995).

43. Xiong, Y. L., Bruneau, C. H. & Kellay, H. A numerical study of two dimensional flows past a bluff body for dilute polymer solutions. *J. Nonnewton. Fluid Mech.* **196,** 8–26 (2013).

44. Phan-thien, N. & Dou, H. Viscoelastic Flow past a cylinder : drag coefficient. Comput. Methods. Appl.Mech. Eng. **180,** 243-266 (1999)

45. Alves, M. A., Pinho, F. T. & Oliveira, P. J. The flow of viscoelastic fluids past a cylinder: finite-volume high-resolution methods. *J. Nonnewton. Fluid Mech.* **97,** 207–232 (2001).

46. Ribeiro, V. M., Coelho, P. M., Pinho, F. T. & Alves, M. A. Viscoelastic fluid flow past a confined cylinder: Three-dimensional effects and stability. *Chem. Eng. Sci.* **111,** 364–380 (2014).

47. Afonso, A. M., Oliveira, M. S. N., Oliveira, P. J., Alves, M. A. & Pinho, F. T. The Finite Volume Method in Computational Rheology. **M,** (1990).

48. McCarthy, K. L., Kauten, R. J., McCarthy, M. J. & Steffe, J. F. Flow profiles in a tube rheometer using magnetic resonance imaging. *J. Food Eng.* **16,** 109–125 (1992).

49. Seymour, J. D., Maneval, J. E., McCARTHY, K. L., Powell, R. L. & McCARTHY, M. J. Rheological Characterization of Fluids Using Nmr Velocity Spectrum Measurements. *J. Texture Stud.* **26,** 89–101 (1995).

50. Callaghan, P. T. Rheo-NMR: nuclear magnetic resonance and the rheology of complex fluids. *Reports Prog. Phys.* **62,** 599–670 (1999).

51. Huettel, S. A., Song, A. W. & McCarthy, G. *Functional magnetic resonance imaging*. *Magnetic Resonance Imaging* (2004).

52. Choi, Y. J., McCarthy, K. L. & McCarthy, M. J. A MATLAB graphical user interface program for tomographic viscometer data processing. *Comput. Electron. Agric.* **47,** 59–67 (2005).

53. Arola, D. F., Powell, R. L., Barrall, G. A. & McCarthy, M. J. A simplified method for accuracy estimation of nuclear magnetic resonant imaging. *Rev. Sci. Instrum.* **69,** 3300–3307 (1998).

54. Arola, D. F., Powell, R. L., Barrall, G. A. & McCarthy, M. J. Pointwise observations for rheological characterization using nuclear magnetic resonance imaging. *J. Rheol.* **43,** 9–30 (1999).

55. Arola, D. F., Barrall, G. A., Powell, R. L., McCarthy, M. J. & McCarthy, K. L. Use of nuclear magnetic resonance imaging as a viscometer for process monitoring. *Chem. Eng. Sci.* **52,** 2049–2057 (1997).

56. Coussot, P., Tocquer, L., Lanos, C. & Ovarlez, G. Macroscopic vs. local rheology of yield stress fluids. *J. Nonnewton. Fluid Mech.* **158,** 85–90 (2009).

57. Choi, Y. J., McCarthy, K. L. & McCarthy M. J. Tomographic techniques for measuring fluid flow properties. *J Food Sci* **67,** 2718–2724 (2002).

58. Tozzi E.J., Bacca L.A.Robust, Hartt W.H., McCarthy, K.L., M.J. McCarthy Processing of capillary velocimetry data via stress-rescaled velocity functions. *J. Rheol.,* **56,** 6 (2012).

59. Benchabane, A. & Bekkour, K. Rheological properties of carboxymethyl cellulose (CMC) solutions. *Colloid Polym. Sci.* **286,** 1173–1180 (2008).

60. Nguyen, Q. D. & Boger, D. V. Measuring The Flow Properties Of Yield Stress Fluids. *Annu. Rev. Fluid Mech.* **24,** 47–88 (1992).

61. Das, B., Nayak, A. K. & Nanda, U. Topical gels of lidocaine HCl using cashew gum and Carbopol 940: Preparation and in vitro skin permeation. *Int. J. Biol. Macromol.* **62,** 514–517 (2013).

CURRICULUM VITAE

Surname, Name	Tezel Tanrısever, Güler Bengüsu
Nationality	Turkish
Date of Birth	08/02/1986
Place of Birth	Kırıkkale
Marital Status	Married
e-mail	bengusu@metu.edu.tr

EDUCATION

2009-Present	Middle East Technical University, Ankara /Turkey PhD in Department of Chemical Engineering
2004-2008	Hacettepe University, Ankara /Turkey BSc in Department of Chemical Engineering

ACADEMICAL EXPERIENCES

02/01/2014-09/01/2014	Visiting Scholar, Department of Food Science andTechnology,University of California , Davis, USA
02/2011-Present	Research Assistant, Department of Chemical Engineering, Middle East Technical University
09/2010-02/2011	Research Assistant, Department of Mechanical Engineering, Abant Izzet Baysal University
06/2008-09/2009	Scholar Student Researcher, TUBITAK Project Grant no:107M594,''Kinetics of reaction between CO_2 and CO_2-bindingorganicliquid:DBU''.Hacettepe University

Publications

1. Tezel G.B., Yapıcı K., Uludağ Y., Computational investigation of viscoelastic flow around square obstacle, Int. J. Numer. Meth. Fluids, 2016, submitted.

2. Uzuner S., Tezel G.B., Cakmak K.N., Effect of Temperature, Gum concentration and gum ratio on Creep-Recovery Behavior of CMC-GG Gum mixtures: modeling with RSM and ANN., Italian Journal of Food Science, 2016, DOI: 10.14674/1120-1770/ijfs.v245.

Presentations

1. Tezel G.B., Yapıcı K., Uludağ Y., Rheology of water based TiO_2 nanofluids at high concentration, 8th Annual European Rheology Conference, 2-5 April 2013, University of Leuven, Belgium. (Poster)

2. Tezel G.B., Yapıcı K., Uludağ Y., Kare silindir etrafında viskoelastik akısın incelenmesi, UKMK-10, 3-6 September 2012, Koç University, İstanbul Turkey. (Oral)

3. Öztürk Ç.M., Tezel G.B., Alper E., Kinetics of reaction between CO2 and a CO2-binding organic liquid DBU, 6th Chemical Engineering Conference for Collaborative Research in Easterm Mediterranean Countries, 7 – 12 March , 2010, Antalya, Turkey. (Poster) DOI: 10.13140/2.1.3674.6245.

4. Tezel G.B., Kaya F.B., Tunç Ö., Zaksu Z., The removal of Reactive dyestuff of Turquoise Blue G. by white-rot fungus Trametes versicolor, UKMK-8, 26-29 August 2008, İnönü University, Malatya Turkey. (Poster)